



Max-Planck-Institut für Metallforschung
Stuttgart

A metastable HCP intermetallic phase in Cu-Al bilayer films

Limei Cha

Dissertation
an der
Universität Stuttgart

Bericht Nr. 184
Februar 2006

A metastable HCP intermetallic phase in Cu-Al bilayer films

Von der Fakultät Chemie der Universität Stuttgart
Zur Erlangung der Würde eines
Doktors der Naturwissenschaften (Dr. rer. nat.)
genehmigte Abhandlung

Vorgelegt von
Limei Cha
aus Yunnan

Hauptberichter: Prof. Dr. Dr. h.c. M. Rühle
Mitberichter: Prof. Dr. E. Arzt
Tag der Einreichung: 08. 12. 2005
Tag der Prüfung: 13. 02. 2006

MAX-PLANCK-INSTITUT FÜR METALLFORSCHUNG
STUTT GART 2006

Contents

List of abbreviations and symbols	I
Summary	IV
Zusammenfassung	VIII
1 Introduction	1
2 Fundamentals	4
2.1 Interface structure	4
2.1.1 Lattice mismatch and strain	4
2.1.2 Orientation relationship	5
2.2 Growth of thin films	6
2.2.1 Wetting and film growth mechanisms	6
2.2.2 Coherence state at interfaces between film and substrate or between films	8
2.3 Defects in films	10
2.3.1 Dislocations	10
2.3.2 Stacking faults	11
2.4 Diffusion	13
2.5 Hume-Rothery laws and electron phases	15
2.5.1 Hume-Rothery laws	15
2.5.2 Electron phases	16
2.6 Cu-Al system	16
2.6.1 Phase diagram	17
2.6.2 Structures of the intermetallic phases in the Cu-Al system	18

2.6.3	Guinier-Preston zones	20
3	Literature overview	23
3.1	Metal-metal interfaces in layered films	23
3.1.1	Reconstruction at metal-metal interfaces	24
3.1.2	Amorphization at metal-metal interfaces	25
3.1.3	Metastable phase formation at metal-metal interface	27
3.1.4	FCC-HCP transformation	29
3.2	Cu-Al film system	30
3.3	Main aim of this work	32
4	Experimental methods and specimen preparation	34
4.1	Experimental methods	34
4.1.1	X-ray diffraction	34
4.1.2	X-ray reflectivity	36
4.1.3	Atomic force microscopy	37
4.1.4	Transmission electron microscopy	39
4.2	Sample preparations	53
4.2.1	Film deposition	53
4.2.2	TEM sample preparation	54
4.2.3	Fabrication, identification and k -factor of the standard sample for the Cu-Al system	56
5	Experimental results and analysis	61
5.1	Cu/Al multilayer films on Si	61
5.2	Cu/Al multilayer films on sapphire	68
5.2.1	Cu/Al bilayer films fabricated by sputtering	68
5.2.2	Cu/Al bilayer films processed by MBE	81

6 Discussion	107
6.1 The formation and characteristics of the interlayer	107
6.1.1 Formation of the interlayer between Cu and Al layers	107
6.1.2 The morphology, atomic structure and chemical concentration of the interlayer	109
6.1.3 Thermal stability of the HCP phase	122
6.1.4 Comparison of the results to the literature on Cu-Al film systems	122
6.2 The formation mechanism of the interlayer with HCP structure	124
6.2.1 The connection between chemical composition and structure of the HCP phase	124
6.2.2 From FCC to HCP	127
6.2.3 The mechanism of phase formation	132
6.2.4 Comparisons to literature results on structure transformations in metal films	134
7 Conclusions	136
List of Figures	139
List of Tables	143
Bibliography	144
Acknowledgements	154
Curriculum Vitae	156

List of abbreviations

AES	Auger-electron spectroscopy
AEM	analytical electron microscopy
AFM	atomic force microscopy
BCC	body-centered cubic
BF	bright field
CTEM	conventional transmission electron microscopy
CTF	contrast transfer function
CVD	chemical vapour deposition
DF	dark field
DP	diffraction pattern
EDS	X-ray energy dispersive spectroscopy
EELS	electron energy-loss spectroscopy
ELNES	electron energy-loss near-edge structure
EPMA	electron probe microanalysis
EXELFS	extended energy loss fine structure
EPMA	electron probe microanalysis
EXAFS	extended X-ray-absorption fine structure
FCC	face-centered cubic
FIB	focus ion beam
GP zone	Guinier-Preston zone
HAADF	high-angle annular dark field
HCP	hexagonal close packed
HRTEM	high resolution transmission electron microscopy

FWHM	Full width at half maximum
IBAD	ion beam assisted deposition
IM	ion-beam mixing
MBE	molecular beam epitaxy
ML	monolayer
OR	orientation relationship
PLD	pulsed laser deposition
POA	phase-object approximation
RBS	Rutherford backscattering spectroscopy
RT	room temperature
SAD	selected-area diffraction
SEM	scanning electron microscopy
SSA	solid-state amorphization
STM	scanning tunnelling microscopy
STEM	scanning transmission electron microscopy
SEM	scanning electron microscopy
TEM	transmission electron microscopy
WDS	wave length dispersive spectroscopy
WPOA	weak-phase-object approximation
XCF	cross-correlation factor
XPS	X-ray photoelectron spectroscopy
XRD	X-ray diffraction

List of symbols

A	atomic weight
Z	atomic number
a	lattice parameter of a unit cell in X direction

b	lattice parameter of a unit cell in Y direction
c	lattice parameter of a unit cell in Z direction
C	chemical concentration
d	d-spacing
k	Cliff-Lorimer factor
m	valence electron density
n	index of refraction
α	incidence angle
α_c	critical angle
μ	absorption length
δ	lattice misfit
ρ	density
σ	roughness
λ	wave length
γ	surface stress
(hkl)	crystallographic plane
$\langle hkl \rangle$	crystallographic direction

Summary

The developments in the microelectronic industry in the past years are focusing on a reduction of the sizes of devices. This size reduction allows an increase of the packaging density of electronic circuits. Prerequisites for a successful miniaturization of the devices are good bonding and chemical stability of the interconnections between the different materials. These requirements led to increased applications of multilayered metal films. Since the properties of layered films are strongly influenced by the characteristics of the interface, the studies of the interface behaviors in metal-metal system are very important.

Cu/Al layered films are selected as a subject in many studies for metal-metal systems due to their common usages in industry [Clemens], [Campisano], [Merkle], [Hamm]. However, Cu/Al films are complicated model systems for the investigation of interface properties, since thermodynamic stable and metastable intermetallic phases and a 10 % lattice mismatch may induce different characteristics depending on the processing conditions. Therefore, earlier research studies on Cu/Al layered films were mostly concentrating on the phase formation at high temperatures or after annealing, but not on the initial structure and chemical composition at the interface at room temperature (RT). Only a few studies have been done by Simic and Marinkovic, Chen *et al.* and Vandenberg and Hamm [Simic], [Chen HY], [Vandenberg] in the latter research field. However, their results differ from each other. Therefore, the aim of the present work was to obtain fundamental knowledge about the structural and chemical characteristics of the interface between Cu and Al films at RT.

For the present study, three kinds of layered Cu/Al films have been fabricated. The first kind of samples were multilayered Cu/Al films deposited by sputtering on (001) Si. The individual layer thicknesses were 100 nm, 200 nm and 400 nm, while the total film thickness of 800 nm was kept constant, thus leading to multilayer systems with 8, 4 and 2 layers, respectively. The second type of samples were Cu/Al bilayer films grown on (0001) sapphire by sputtering, with individual layer

thicknesses of 400 nm. The third type of samples were bilayer films (100 nm Cu and 100 nm Al) deposited on (0001) sapphire by MBE at room temperature.

Applying conventional transmission electron microscopy (CTEM) and X-ray diffraction (XRD) (θ - 2θ scans and pole figure measurements), different epitaxial growth behaviors were found in these films. All multilayer films from the first type were polycrystalline. The second type of films show a (111)_{FCC} texture and possess intermetallic phases at the interfaces. The orientation relationship (OR) between the bilayer film and the substrate was:

$$\pm \langle 110 \rangle (111)_{\text{Cu}} // \pm \langle 110 \rangle (111)_{\text{Al}} // \langle 2-1-10 \rangle (0001)_{\text{sapphire}}$$

The films of the third kind are mainly epitaxial, with the following OR between films and the substrate:

$$[-110] (111)_{\text{Cu}} // [-110] (111)_{\text{Al}} // [10-10] (0001)_{\text{sapphire}}$$

The films from the third group show the best epitaxial behavior and thus the major work in this thesis was performed on these samples. It was found that an interlayer with a thickness of 8 nm is located between the pure Cu and the pure Al film as observed by CTEM, using a JEOL JEM-2000FX. HRTEM investigations performed with a JEM ARM-1250 operated at 1250kV displayed that along $[111]_{\text{FCC}}$, the atomic structure of the interlayer has an *ABAB* stacking sequence, which is identical with a hexagonal close-packed (HCP) structure in $[0001]$ direction, but not with the *ABCABC* stacking sequence of Cu and Al in $[111]_{\text{FCC}}$. The changing intensities of atomic columns suggested that different layers are occupied by different atoms. To understand the structure of the interlayer in detail, a HCP atomic model was constructed and used for image simulations which were performed with the soft-package named electron microscopy simulation (EMS). The lattice parameters of the HCP structure at the interlayer were determined from a model which gave the best agreement between the experimental and simulated images. The parameters are: $a = b = 0.256$ nm, $c = 0.419$ nm, $\gamma = 120^\circ$, with the space group of P-6m2. For the quantitative HRTEM the program of iterative digital image matching (IDIM) was used. The agreements between the simulated images and

the experimental images are 93.1 % and 93.4 % for $\langle 110 \rangle_{\text{FCC}}$ and $\langle 112 \rangle_{\text{FCC}}$ directions, respectively. The orientation relationship between the two FCC metal layers and the HCP interlayer is:

$$\langle 110 \rangle (111)_{\text{FCC}} // \langle 11-20 \rangle (0001)_{\text{HCP}}.$$

Furthermore, lattice distortion analysis (LADIA) revealed that the lattice parameters of the HCP phase are increasing from the near-Cu-side to the near-Al-side, although the symmetry of the HCP structure remains.

The chemical composition of the interlayer was investigated by energy dispersive X-ray spectroscopy (EDS) in a VG HB501UX dedicated scanning transmission electron microscope (STEM). EDS linescans were performed from pure Al to pure Cu layers. To obtain the absolute chemical composition of the interlayer, quantitative X-ray microanalysis was necessary. Thus, a standard CuAl_2 alloy sample was employed to obtain the experimental k -factor of the Cu-Al system. Using the determined k -factor, the results indicated that there is 27 ~ 58 at % of Al in the interlayer and that the Al concentration is gradually increasing from the near-Cu-side to the near-Al-side. This result is in agreement with Hume-Rothery laws for alloy phases. However, beam broadening, which is influenced by the thickness of the specimen and the nature of the investigated material, leads to a smeared diffusion-like concentration profile. Nevertheless, the EDS results together with image simulations, performed using different chemical concentrations of the HCP phase, revealed a compositional gradient across the interlayer.

The formation mechanism of the intermetallic phase, which locates at the Cu/Al interface and possesses a broad composition range and a HCP structure, can be explained by Hume-Rothery laws and Shockley partial dislocations, cooperating with diffusions. During the film deposition, the chemical composition is modified by alloying and diffusion processes occurring between Cu and Al. According to Hume-Rothery, when the chemical composition reaches certain values, the corresponding valence electron densities will start to stabilize the HCP structure, while FCC structures are getting energetically unfavorable. Simultaneously, the extending of the Shockley partial dislocation in $\langle 112 \rangle$ directions will trigger the stacking sequence altering from the FCC structure to the HCP structure in the close packed direction.

In order to examine the stability of this HCP phase, *in-situ* heating experiments were performed in the HRTEM at $\sim 600^\circ\text{C}$. After cooling the sample to RT, the HCP phase disappears and three equilibrium intermetallic phases i.e. CuAl, CuAl₂, and Cu₉Al₄ form. This suggests that the HCP intermetallic phase is metastable. *Ex-situ* heating experiments were performed at different temperatures to obtain the temperature range in which the HCP metastable phase will be stable. According to the XRD measurements, it is found that the metastable HCP phase exists below 120°C .

Zusammenfassung

In der mikroelektronischen Industrie werden immer mehr unterschiedliche Bauteile auf kleinstem Raum benötigt. Voraussetzung für eine erfolgreiche Miniaturisierung ist eine gute Bindung und chemische Stabilität zwischen den verschiedenen Materialien, aus denen sich die einzelnen Komponenten zusammensetzen. Um diese Anforderungen zu erfüllen, werden zunehmend mehrlagige Metallschichtsysteme verwendet. Da die Eigenschaften dieser Schichtsysteme häufig von der Struktur an den Metall-Metall Grenzflächen beeinflusst werden, sind Untersuchungen von Grenzflächen von großer Bedeutung.

Schichtstrukturen aus Kupfer und Aluminium wurden in der Vergangenheit wegen ihrer technologischen Relevanz in verschiedenen Studien untersucht ^{[Clemens], [Campisano], [Merkle], [Hamm]}. In diesem komplizierten System treten sowohl thermodynamisch stabile als auch metastabile intermetallische Phasen auf, zusätzlich muss eine Gitterfehlpassung von 10% berücksichtigt werden. Diese Faktoren bewirken, dass die Grenzflächenstruktur stark von den Prozessbedingungen und Prozesstemperaturen beeinflusst wird. Frühere Studien konzentrierten sich überwiegend auf die Phasenbildung an der Grenzfläche bei höheren Prozesstemperaturen und/oder nach einer thermischen Auslagerung ^{[Clemens], [Campisano], [Merkle], [Hamm]}. Nur einige wenige Arbeiten ^{[Simic], [Chen HY], [Vandenberg]} beschäftigten sich bisher mit der Grenzflächenstruktur bei Raumtemperatur, aber die Ergebnisse weichen voneinander ab. Deshalb war es ein Ziel der vorliegenden Arbeit, ein grundlegendes Verständnis über die strukturelle und chemische Beschaffenheit der bei Raumtemperatur gebildeten Grenzfläche zwischen Cu und Al Filmen zu gewinnen.

Für die vorliegende Arbeit wurden Cu/Al Schichten auf drei unterschiedliche Arten hergestellt. Zuerst wurden Cu und Al durch Magnetronspütern auf (001) Si abgeschieden. Die individuelle Schichtdicke war 100 nm, 200 nm und 400 nm. Die Gesamtschichtdicke betrug immer 800 nm. Die Proben wurden also von acht, vier und zwei Lagen gebildet. Zweilagige Schichten mit je 400 nm Cu und Al wurden ebenfalls durch Magnetronspütern auf (0001) Saphir hergestellt.

Desweiteren wurden mit Molekularstrahlepitaxie (MBE) Bilagen von je 100 nm Cu und Al auf (0001) Saphir abgeschieden.

Konventionelle Transmissionselektronenmikroskopie (CTEM), hochauflösende Transmissionselektronenmikroskopie (HRTEM), analytische Transmissionselektronenmikroskopie (AEM) und Röntgenbeugung (θ -2 θ Scans und Polfiguren) wurden eingesetzt, um die Proben zu untersuchen. Es wurden unterschiedliche Orientierungsbeziehungen zwischen den Filmen und den Substraten gefunden. Die auf Si abgeschiedenen Filme waren polykristallin. Die magnetron-gesputterten Filme auf (0001) Saphir zeigten eine (111)_{FCC} Textur und wiesen intermetallische Phasen an der Grenzflächen auf. Die Orientierungsbeziehung für diese Filme lautete:

$$\pm \langle 110 \rangle (111)_{\text{Cu}} // \pm \langle 110 \rangle (111)_{\text{Al}} // \langle 2-1-10 \rangle (0001)_{\text{Saphir}}$$

Die Filme, welche mit der dritten Methode hergestellt wurden, sind epitaktisch, mit folgender Orientierungsbeziehung:

$$[-110] (111)_{\text{Cu}} // [-110] (111)_{\text{Al}} // [10-10] (0001)_{\text{Saphir}}$$

Da die Filme der dritten Herstellungsart epitaktisch sind, bildeten sie den Schwerpunkt der Arbeiten in dieser Dissertation. Für diese Filme ergaben sich folgende Ergebnisse. Mittels CTEM wurde eine Phase mit 8 nm Dicke zwischen den reinen Cu und Al Schichten gefunden. Für diese Untersuchungen wurde ein JEOL JEM-2000FX verwendet. HRTEM Studien, durchgeführt am JEOL JEM 1250ARM, zeigten, dass die Phase an der Grenzfläche eine *ABAB* Stapelung in [111]_{FCC} Richtung aufweist. Diese ist identisch mit der Stapelung einer hexagonal dicht gepackten (HCP) Struktur in [0001] Richtung, stimmt aber nicht überein mit der *ABCABC* Stapelfolge in [111]_{FCC} Richtung für Cu oder Al. Die Intensitäten in den HRTEM Bildern von der Grenzflächenphase legen nahe, dass die einzelnen Gitterebenen mit unterschiedlichen Atomspezies belegt sind. Für ein Verständnis der Zwischenschicht wurde ein HCP Strukturmodell erstellt. Damit konnten Bildkontrastsimulationen, durch Verwendung des Softwarepackets „Electron Microscopy Simulations“ (EMS), durchgeführt werden. Die Gitterparameter der HCP Struktur konnten aus dem Vergleich der experimentellen Bilder mit den am besten angepassten simulierten Bildern gewonnen

werden. Dabei ergaben sich: $a = b = 0.256 \text{ nm}$, $c = 0.419 \text{ nm}$, $\gamma = 120^\circ$, und die Raumgruppe P-6m2. Die quantitative HRTEM Analyse wurde mit dem Softwarepaket „Iterative Digital Image Matching“ (IDIM) durchgeführt. Die besten Anpassungen ergaben für die Kreuzkorrelationskoeffizienten zwischen experimentellen und simulierten Bildern 93.1 % and 93.4 % in $\langle 110 \rangle_{\text{FCC}}$ und $\langle 112 \rangle_{\text{FCC}}$ Richtungen. Die Orientierungsbeziehung zwischen den zwei kubisch raumzentrierten (FCC) Metallschichten und der HCP Zwischenschicht ist:

$$\langle 110 \rangle (111)_{\text{FCC}} // \langle 11-20 \rangle (0001)_{\text{HCP}}.$$

Desweiteren wurde das Programm „Lattice Distortion Analysis“ (LADIA) eingesetzt. Dadurch wurde nachgewiesen, dass die Gitterparameter in der Zwischenschicht von der Cu-nahen-Seite zur Al-nahen-Seite größer werden, obwohl die HCP Struktur erhalten bleibt.

Die chemische Zusammensetzung der Zwischenschicht wurde mit Hilfe der energieaufgelösten Röntgenspektroskopie (EDS) in einem VG HB501UX, einem Rastertransmissionselektronenmikroskop, aufgeklärt. EDS Linienprofile wurden von der Al Schicht zur Cu Schicht aufgenommen. Für eine detaillierte Analyse wurde eine CuAl_2 Referenzprobe verwendet und experimentell ein k -Faktor für das Cu-Al System bestimmt. Dieser k -Faktor ermöglichte es die Konzentration des Al in der Zwischenschicht mit 27 ~ 58 at% zu bestimmen. Die Al-Konzentration fällt stetig von der Al-nahen-Seite zur Cu-nahen-Seite ab. Dieses Ergebnis ist in Übereinstimmung mit den Hume-Rothery-Regeln für metallische Legierungen. Strahlaufweitung, beeinflusst durch die Dicke und die chemische Natur der Probe, führt jedoch zu einer Verschmierung des Konzentrationsprofils, ähnlich eines Diffusionsprofils. Trotz dieses Phänomens ergaben die EDS Ergebnisse, zusammen mit Bildsimulationen für verschiedene chemische Zusammensetzungen, den Nachweis, dass ein Konzentrationsgradient in der Zwischenschicht existiert.

Der Bildungsmechanismus der intermetallischen Zwischenschicht mit den oben angegebenen Eigenschaften lässt sich durch die Hume-Rothery-Regeln, durch Shockley Partialversetzungen, sowie Diffusion erklären. Während der Filmabscheidung wird die chemische Zusammensetzung durch Legierungsbildung und Interdiffusion zwischen Cu und Al verändert. Wie in den Hume-Rothery-Regeln erklärt, wird die HCP Struktur stabilisiert sobald die chemische Zusammensetzung und somit die Valenzelektronendichte einen Wert erreicht bei dem die Energie der

FCC Struktur über der der HCP Struktur liegt. Gleichzeitig wird die Stapelfolge in $\langle 111 \rangle$ Richtung durch $\langle 112 \rangle$ Shockley Partialversetzungen von der FCC Sequenz auf die HCP Sequenz geändert.

Die Stabilität der HCP Phase wurde durch *in-situ* Heizexperiment untersucht. Dabei wurden im HRTEM die Proben auf $\sim 600^\circ\text{C}$ aufgeheizt. Nach der Abkühlung auf RT war die HCP Phase verschwunden und die drei Gleichgewichtsphasen CuAl , CuAl_2 and Cu_9Al_4 wurden gebildet. Dies deutet darauf hin, dass die HCP Phase metastabil ist. *Ex-situ* Heizexperimente wurden bei unterschiedlichen Temperaturen durchgeführt, um den Temperaturbereich zu bestimmen, in dem die metastabile HCP Struktur stabil ist. Durch Röntgenbeugungsexperimente wurde gefunden, dass die HCP Phase unterhalb 120°C stabil ist.

Chapter 1

Introduction

Bilayer / multilayer metallic thin films are frequently used in the fabrication of electronic devices, in order to combine the advantage of each material involved to obtain best performance. The properties of the devices strongly depend on the nature of the metal-metal interface, though the interface is just a layer (for abrupt interfaces) or a few layers (for rough interfaces) of atoms. Due to the importance, many studies have been performed at metal-metal interfaces ^{[Shearer], [Hamm], [Royce], [Geng]}. The methods applied to investigate the characteristics of different metal-metal interfaces are various, e.g. *in-situ* and *ex-situ* X-ray diffraction (XRD) ^{[Clemens], [Hamm]} for phase identification of solid state reactions; high resolution transmission electron microscopy (HRTEM) ^[Merkle] and image contrast simulation^[Howe] for the determination of the atomic structure at interfaces; scanning tunnelling microscopy (STM) ^[Tsay] for studying the reconstruction at the interfaces between ultra thin metal films and metal substrates; Rutherford backscattering spectroscopy (RBS) ^[Campisano] and X-ray energy-dispersive spectroscopy (EDS) ^[Chen Z] for the chemical composition analysis at interfaces; Auger-electron spectroscopy (AES) ^[Kief] and X-ray photoelectron spectroscopy (XPS)^[Campbell] to get insight in the interfacial electronic structure.

The material combination of Cu and Al is widely used in industry, for example, in modern computer industry the interconnections between Cu-based chips is via a thin Al layer. Compared to perfect model systems for metal-metal interfaces, which are often abrupt and possess neglectable strain due to a small lattice mismatch, and where no intermetallic phase are found, the interfaces of layered Cu/Al films are more complicated. This is because different thermodynamic stable

intermetallic phases as well as metastable phases exist. Furthermore, the system has a quite large lattice misfit of 10 %. Both facts imply that the Cu/Al interface structure is strongly depending on the processing and/or annealing temperatures.

In earlier studies [Simic], [Broeder], [Funamizu], [Hentzell], [Jiang], [Fadnis], [Markwitz], [Rayne] it was found that layered Cu/Al films on NaCl and Si grow polycrystalline. Most of the investigations revealed that the initially formed intermetallic phase at the interface is CuAl₂ if the processing or an annealing temperature at or below 200 °C is applied. However, about the sequence of the intermetallic phase formation in layered film, some discrepancy exists. Besides this, the Cu/Al interfacial structure at room temperature (RT), which has rarely been investigated, was not described uniquely. Chen *et al.* [Chen HY] reported that the interfacial structure of the Cu/Al film is ‘mutiphased’, while Simic *et al.* [Simic] emphasized in their work that no intermetallic phase can form in Cu/Al layered films at RT. Independent of this, the Cu/Al interface structure at RT was only investigated by XRD and/or extended X-ray-absorption fine structure (EXAFS), but not by imaging techniques at an atomic level. Thus, the initial phase formation at the Cu/Al interface at RT, as well as the interfacial structure at an atomic level, is still an open question. Therefore, the objective of this thesis is to study the structural and chemical characteristics of the initial intermetallic phase formed at the interface between Cu and Al films at RT.

In the present work, the Cu/Al interface is produced by depositing Cu/Al layered films on both (001) Si and (0001) sapphire. The films are grown by sputtering and molecular beam epitaxy (MBE). XRD will be used to identify the phases in the layered films and the orientation relationship between the films and the substrate. To obtain the morphology and atomistic structure of the interface, conventional transmission electron microscopy (CTEM) and HRTEM, will be used, respectively. The atomistic structure will be quantitatively analyzed by image simulation of the HRTEM micrographs. The chemical composition at the Cu/Al interface will be determined by using EDS and electron energy-loss spectroscopy (EELS) in an analytical transmission electron microscopy (TEM), employing quantified analysis with the assistance of a standard Cu-Al alloy sample. Furthermore, *in-situ* and *ex-situ* heating experiments will be performed to obtain more information about the phase stability and/or transformation of the pure metal phases and/or possible intermetallic phase formation at the interface.

The outline of this thesis is the following:

After the introduction, chapter 2 outlines fundamental aspects of the phenomena in thin films on bulk substrates, the Hume-Rothery laws for electron phases, and the characteristics of alloy phases in the Cu-Al system. In chapter 3 the literature relevant to this thesis is summarized. Emphasis is made on the structure of various metal-metal interfaces, and on studies in Cu-Al layered films. After that, the aim of this thesis will be given. Chapter 4 introduces the experimental techniques applied in the present work, including methods for TEM sample preparation and the fabrication and characteristic of the standard alloy sample. The results of this work are summarized in chapter 5, which is divided into two parts: the study of polycrystalline layered Cu/Al films, which grew on Si and sapphire by sputtering; and the investigation of epitaxial Cu/Al bilayer films deposited on sapphire by MBE. In addition to the experimental results, the results of the image simulation will be presented. In chapter 6, the structure, chemical composition and thermodynamic stability of the interface will be discussed, taking into account the corresponding experimental conditions and results from literature. In the last chapter, the results are summarized.

Chapter 2

Fundamentals

In this chapter, the basics will be summarized for the areas of the experiments, for the analysis of the results and for the discussion,.

2.1 Interface structure

When a film grows on a substrate or a precipitate forms in a matrix, interface(s) form between the different phases involved. Lattice mismatch and orientation relationship (OR) at an interface are the most fundamental factors. A short description will be given in the following. More detailed information can be found in the book of Feng ^[Feng].

2.1.1 Lattice mismatch and strain

The lattice mismatch (δ) is defined as:

$$\delta = (b-a) / a \cdot 100 \% \quad (2.1)$$

where a and b are the corresponding lattice parameters of the film and substrate¹, respectively. Two points should be noted: (i) usually the values of the lattice mismatch are calculated at room temperature.

¹ In layered films, the film grown first can be also considered as a kind of substrate.

If the thermal expansion coefficients of the film and substrate are different (while it usually the same), then the value of the lattice mismatch depends on the temperatures. (ii) the value of the lattice mismatch is strongly influenced by the orientation relationship between the film and the substrate.

A lattice mismatch induces stress to both the film and substrate. The magnitude of stress is proportional to the value of the mismatch. As Fig.2.1 shows, there are two types of stresses induced by the lattice mismatch. When the lattice mismatch is positive, the film will be under compressive stress. If the lattice mismatch is negative, the film will be under tensile stress. The minimization of mismatch and strain results in higher quality of the epitaxial film. These simple considerations do not take into account interfacial dislocations.

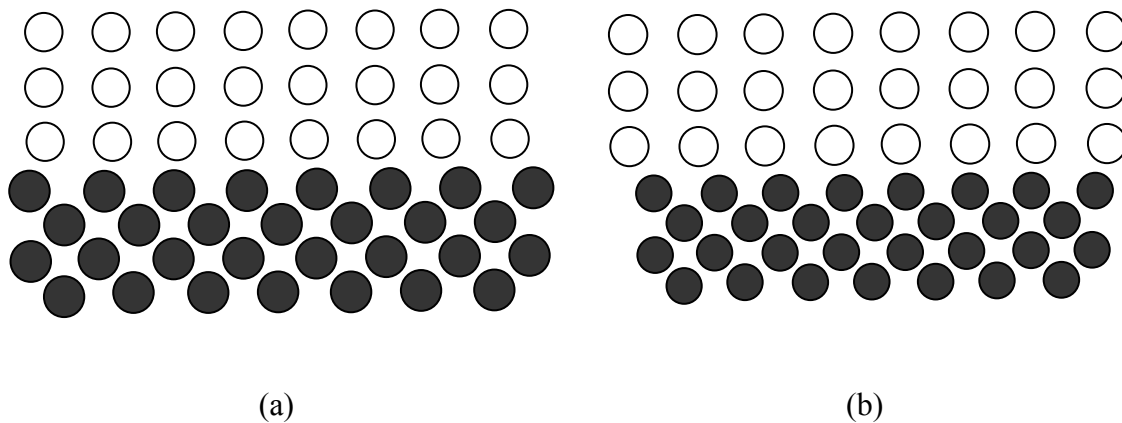


Fig.2.1 Mismatch and strain types in film systems. The open circles are the atoms of the film and the filled circles belong to the layer grown first in a bilayer film system or to the substrate. The value of mismatch of (a) is negative and the film is affected by tensile stress; in (b) the mismatch is positive and the film under compression.

2.1.2 Orientation relationship

In film systems, the orientation relationship (OR) is used to describe the relation orientation between different films (for multilayer system) or between the film and substrate by crystallographic remarks. A complete description of the OR requires the crystallographic nature of the phases in both systems, which are parallel to the interfacial plane. In addition a direction has to be indexed which are parallel in both systems.

If the OR is changes, the properties of the films can be affected. As an example, in Cu/Al layered films, epitaxially grown Cu will be expanded due to the smaller lattice parameter compared to Al. However, if the $\langle 110 \rangle$ directions of the Cu film uses, but not the $\langle 112 \rangle$ direction has to be matched to the $\langle 112 \rangle$ direction of Al in the (111) plane, then the expanded part will be Al but not Cu. In some film systems with a large lattice mismatch, twins (or a textured structure) may form to reduce the strain which can not be fully compensated by the formation of dislocation. Such relaxation mechanism may do influence properties, mechanical properties.

2.2 Growth of thin films

Films can be deposited by various techniques, i.e. molecular beam epitaxy (MBE), pulsed laser deposition (PLD), chemical vapor deposition (CVD) and sputtering. However, the fundamental mechanisms for the film growth are basically the same. Wetting conditions are generally used to explain the film growth modes. In addition, the degree of coherency between the substrate and film influences the structure of the film. More detailed information can be find in the literature from Ohring^[Ohring].

2.2.1 Wetting and film growth mechanisms

Wetting describes the spreading of a (liquid) material on a solid substrate. For film deposition processes, wetting or non-wetting influences the type of film growth.

During deposition, atoms from the target will diffuse and then adhere on the substrate. However, as the deposition continues, most atoms will pile up to form clusters. These clusters will grow into a thin film. According to wetting mechanisms, there are three types of film growth, i.e. layered growth, island growth, and the mixed type. As Fig.2.2 shows there are three surface tensions acting on the droplet simultaneously. γ_s is the surface tension of the substrate, which influence the spreading of the cluster over the substrate. γ_f and γ_{sf} are the surface tension of the cluster and the tension from the interface between the substrate and the film cluster, respectively, which are trying to withdraw the cluster. The competition between the three forces continues until the system reaches equilibrium, with balanced forces. Young's equation can be used to describe the force balance^[Bauer]:

$$\gamma_s = \gamma_f \cos\alpha + \gamma_{sf} \quad (2.2)$$

$$\cos\alpha = (\gamma_s - \gamma_{sf}) / \gamma_f \quad (2.3).$$

Three cases can be distinguished:

1. $\gamma_f = \gamma_s - \gamma_{sf}$: in this situation, $\cos\alpha = 1$ and $\alpha = 0^\circ$. For this case the substrate will be completely wetted by the film cluster. There will be no free substrate surface if sufficient material is present on the substrate. The film grows layer by layer and possesses small surface roughness.
2. $\gamma_s < \gamma_{sf}$: then $\cos\alpha < 0$ and $\alpha > 90^\circ$. The cluster will not wet the substrate. Many 'islands' (cluster) are formed on the substrate. During the deposition of further film material clusters can contact each other, and pores might occur in the film. Island film growth can result in a large surface roughness.
3. $\gamma_f > \gamma_s - \gamma_{sf}$: then $0 < \cos\alpha < 1$ and $0 < \alpha < 90^\circ$. In this situation, the cluster partially wet the substrate. A continuous layer is formed and then islands grow on this layer.

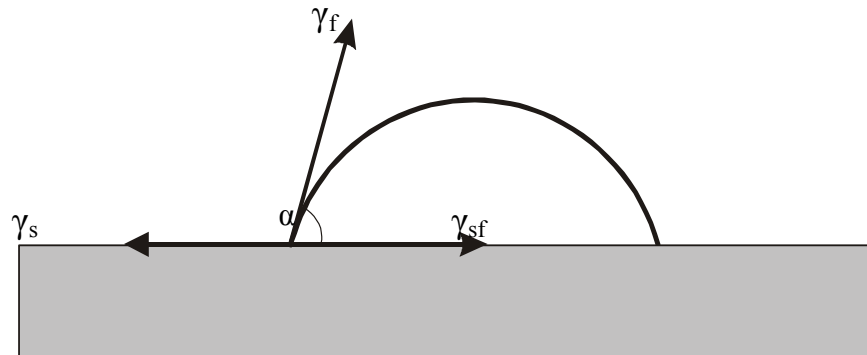


Fig.2.2 Schematic drawing of a cluster on a substrate and the forces acting on the cluster.

The growth behavior is also affected by factors such as deposition temperature and deposition rate. When the deposition rate is much higher than the diffusion rate of the deposited atoms on the surface, the ‘non-wetting’ and / or ‘mixed’ growth types will occur. This can not be described anymore by Young’s equation.

The films grown in the layer-by-layer mode are usually compact with fewer pores and lower roughness compared to the films grown in the islands or mixed mode. Usually, layer-by-layer growth is the preferred growth mode one wants to achieve.

2.2.2 Coherence state at interfaces between film and substrate or between films

For all growth mode, an interface will form between the solid film and the solid substrate. According to the value of lattice mismatch and the ordering of atoms at the interface, a coherent, semi-coherent, or incoherent interface can form^[Hull].

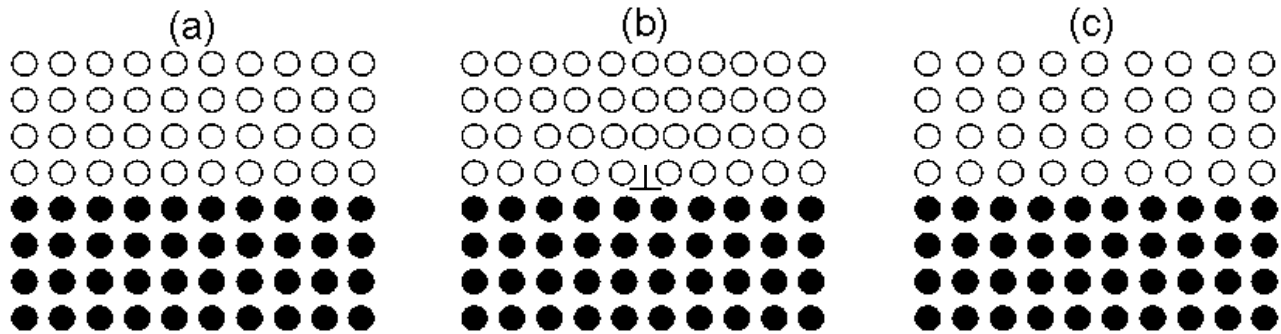


Fig.2.3 For (a) a coherent film, the film has a similar lattice parameter than the substrate, or the film is very thin so stresses are not yet important. For (b) a semi-coherent film-substrate interface, the lattice mismatch is larger and thus misfit dislocation(s) have formed to release stresses in the interface. The misfit dislocations are separated by coherent neighbors. If the lattice mismatch is too large (c), an incoherent interface will form. The open circles are the atoms of the film and the filled circles belong to the undergrowth layer or the substrate.

These three interface structures can be classified as follows:

1. When the lattice mismatch between the substrate and the overgrowth is small, all the atoms at the interface are ordered, and certain planes and directions belonging to the different crystals have a well-defined OR. This is a coherent interface (Fig 2.3 (a)).
2. When the lattice mismatch between the substrate and the overgrowth is large, dislocation will form to release the strain. Regions of perfect fit will occur between the misfit dislocations. This is a semi-coherence state and a common phenomenon in film systems (Fig.2.3 (b)).
3. If the lattice mismatch is too large, and dislocations are not able to release the strain, then the film growth will be independent of the lattice of the substrate,

and no regions of fit occur at the interface. This is an incoherent interface (Fig.2.3 (c)).

2.3 Defects in films

There are different kinds of defects in solid materials, which can be classified according to their dimensions, i.e. point, line, planar and volume defects. Point defects, such as vacancies and interstitial atoms, are zero-dimensional. Line defects are one-dimensional defects, named as dislocations generally. Planar defects are two-dimensional defects, such as stacking faults, grain boundaries, and interfaces. Three dimensional defects are volume defects, which can occur as precipitations, voids and dispersoids [Hull]. For the present work, dislocations and stacking faults are most important and only these two defects will be discussed. More detailed information can be found in 'Introduction to dislocations' [Hull].

2.3.1 Dislocations

Three kinds of dislocations exist: edge dislocation, screw dislocation and mixed dislocation. The different dislocations are described by the orientation relationship between the dislocation lines and Burgers vectors. For an edge dislocation, the Burgers vector is perpendicular to the dislocation line; while the Burgers vector is parallel to the dislocation line for a screw dislocation. For a mixed dislocation, the Burgers vector forms an angle with the dislocation line [Hull].

In general, a lattice translation vector is a vector in the crystal which connects two points in the lattice. If the Burgers vector of a dislocation equals to a unit lattice translation vector, this dislocation is a perfect or an unit dislocation [Hull], e.g. dislocations with the Burgers vectors of $1/2 \langle 110 \rangle$ are the smallest perfect dislocations in a face-centred cubic (FCC) structure.

The energy of a dislocation is proportional to the square of the magnitude of its Burgers vector. A perfect dislocation may decompose into other dislocations with smaller Burgers vectors to decrease the total energy in the system. For smallest perfect dislocations, they only can decompose into dislocations with partial of the lattice translation vectors of the unit cell. The dislocations with partial

translation vectors are known as Shockley partial dislocations, which are usually accompanied with stacking faults (this will be discussed in more detail in section 2.3.2). An example for the formation of Shockley partial dislocation is that in a FCC structure, the perfect dislocation of $1/2 \langle 110 \rangle$ may decompose into two $1/6 \langle 112 \rangle$ Shockley partial dislocations:

$$1/2 [-110] \rightarrow 1/6 [-12-1] + 1/6 [-211] \quad (2.4)$$

$$1/2 [0-11] \rightarrow 1/6 [1-21] + 1/6 [-1-12] \quad (2.5)$$

$$1/2 [-10-1] \rightarrow 1/6 [-211] + 1/6 [-1-12] \quad (2.6)$$

The energies of the perfect and the Shockley dislocation are:

$$\begin{aligned} \text{Perfect dislocation } (\mathbf{b}=1/2 \langle 110 \rangle): & \quad b^2 = (a^2/4) \cdot (1^2 + 1^2 + 0) = a^2/2 \\ \text{Shockley partial dislocation } (\mathbf{b}=1/6 \langle 112 \rangle): & \quad b^2 = (a^2/36) \cdot (1^2 + 1^2 + 2^2) = a^2/6 \end{aligned}$$

The perfect dislocation ($1/2 \langle 110 \rangle$) has a higher energy than the energy of the two Shockley partial dislocations ($1/6 \langle 112 \rangle$), i.e. $a^2/2 > (2 * a^2/6)$. This is the reason why the perfect dislocation can decompose.

2.3.2 Stacking faults

A perfect crystal has fixed stacking sequence in certain directions. For example, for the FCC structure, the normal stacking sequence is ...ABCABC... in $\langle 111 \rangle$ direction, as schematically illustrated in Fig. 2.4. Here, A, B and C are atomic layers with different stacking positions. When the fixed stacking order is disturbed, stacking faults occur. For example, in a FCC structure if the atoms which should take positions A occupy positions B, then the stacking sequence is changed and the process can be described as a slide to B from A. If the following stacking layers continue the normal stacking order according to the slid one, then the stacking order changes to ...ABCBCABC... . This is called an intrinsic stacking fault. In another case, after the first stacking fault (A slides to B), if the next layer does not keep the

stacking ordering according to the slid one, but also slides (not ...ABCBC, but ...ABCBA, i.e. C slides to A), and only the third and the following layers keep the normal stacking order, then the stacking order will be ...ABCABCBAABC... . This looks like that a ‘B’ layer is inserted in the ordered structure. This is an extrinsic stacking fault.

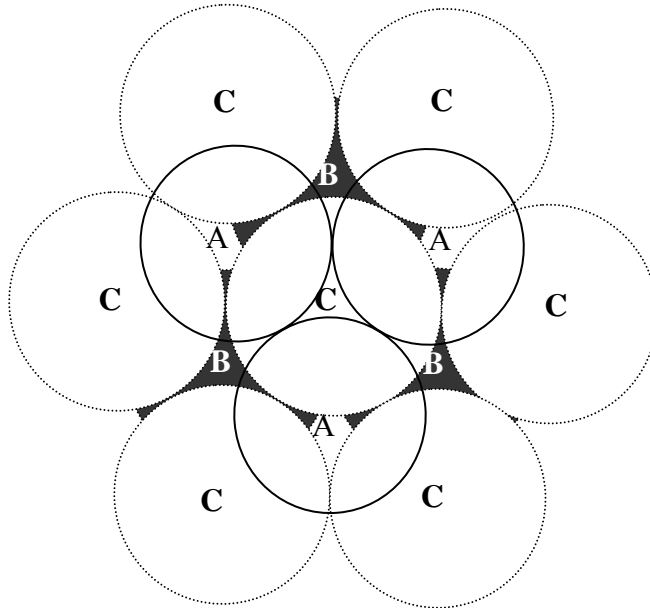


Fig.2.4 Stacking order of atomic layers in $\langle 111 \rangle$ direction in FCC lattices. Different capital letters indicate centers of atoms in various $\{111\}$ layers.

In $\{111\}$ planes of a FCC structure, the slide between positions (e.g. A and B) can be described as an $a/6 \langle 112 \rangle$ vectors. This is a Shockley partial dislocation. Fig. 2.5 (a) is the schematic drawing of Burgers vectors of $1/2 \langle 110 \rangle$ and $1/6 \langle 112 \rangle$ in $\{111\}_{\text{FCC}}$. Fig. 2.5 (b) is a combination of the dislocations (Fig. 2.5 (a)) and atom positions (Fig. 2.4) in $\langle 111 \rangle_{\text{FCC}}$ direction. On top of atoms located at the position ‘C’, if a stacking fault occurs, e.g. atom at position ‘A’ slides to position ‘B’, the vector

is $1/6 \langle 112 \rangle$, which is smaller than the vector from 'A₁' to 'A₂' which is $1/2 \langle 110 \rangle$, as Fig. 2.5 illustrates. Therefore, stacking faults can introduce Shockley partial dislocations.

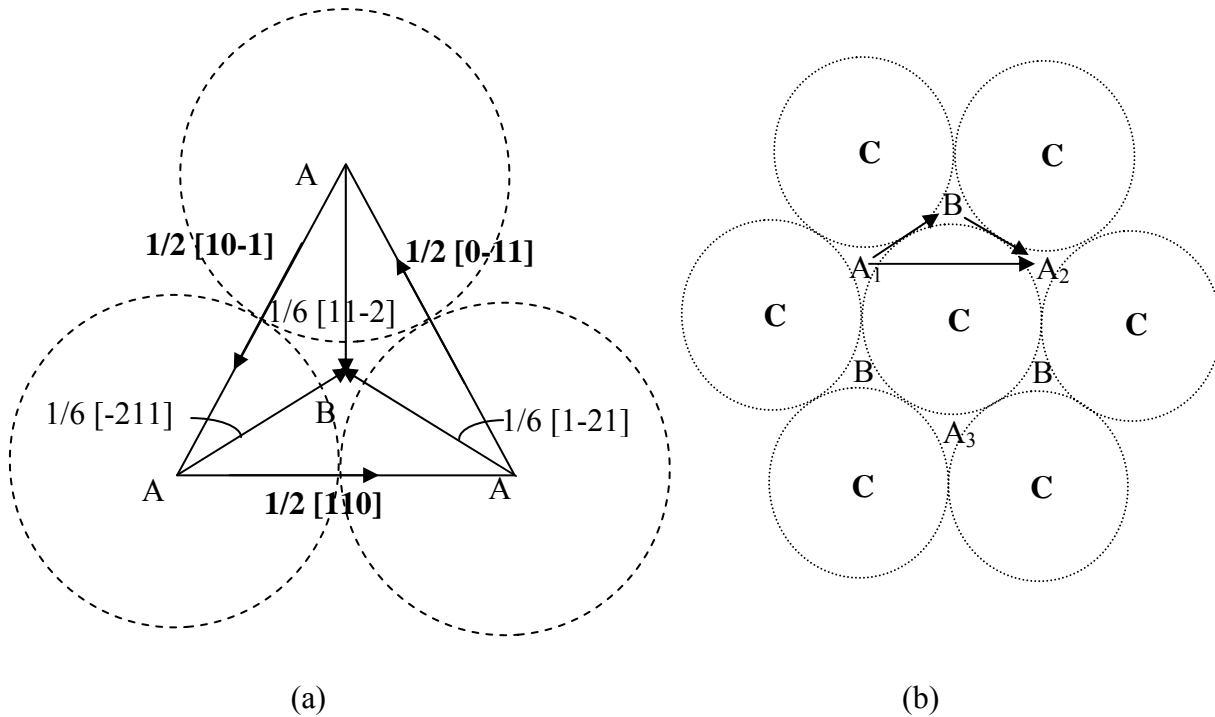


Fig.2.5 (a) Burgers vectors of perfect dislocations ($1/2 \langle 110 \rangle$) and Shockley partial dislocations ($1/6 \langle 112 \rangle$) in a $\{111\}$ plane of FCC. The arrows indicate the direction of the vectors and the circles with dashed lines represent projected positions of atoms. (b) Schematic drawing how the Shockley partial dislocations are induced by stacking faults.

2.4 Diffusion

Atoms in a solid material can jump from one site to another in a random manner, and the activity strongly depends on the temperature ^[Askeland, Barrett]. If a concentration (or chemical potential) gradient exists, atoms will move in one direction and form a flux. This flux, rather than individual atom

movement, is determined as diffusion. In the following the basics of diffusion will be described. More detailed information is found in the textbooks of Askeland and Barrett^{[Askeland], [Barrett]}.

Fick's laws of diffusion

When the concentration gradient is independent on time, a steady state diffusion occurs which can be described by Fick's first law:

$$J = -D \cdot dc/dx \quad (2.7),$$

where J is the number of atoms passing through the plane of unit area per unit time (atoms/cm² * s), D is the diffusion coefficient (cm² / s) which is temperature dependent, c is the composition and dc/dx is the concentration gradient (atoms/ cm³ * cm)^[Askeland]. Here, the concentration is only a function of the distance.

However, in many situations the concentration gradient changes with time and position. The diffusion is nonsteady state diffusion, and described by Fick's second law:

$$dc/dt = D \cdot d^2c/dx^2 \quad (2.8).$$

This law indicates that the rate of the composition change is proportional to the rate of change of the concentration gradient. For a given temperature, the solution for Eq. (2.8) is

$$x / (D \cdot t)^{1/2} = \text{constant} \quad (2.9).$$

It is usually used to obtain some rough estimations, e.g. the time required to achieve appreciable diffusion over a distance x.

According to diffusion paths, diffusion can be described as volume diffusion (3 dimensional), grain boundary diffusion and surface diffusion (2 dimensional) and pipe diffusion along dislocations (1 dimensional). Because the arrangements of atoms at surfaces and grain boundaries are much looser than in the bulk volume, the diffusion rate will be higher along 2 dimensional defects. At lower temperatures, the difference between the surface diffusion coefficient, grain boundary diffusion

coefficient and the volume diffusion coefficient is much larger than that at higher temperatures. This means that surface and grain boundary diffusions play more important roles at lower / room temperatures.

In layered film systems, the interfaces between every two layers also have a more open structure compared to the bulk. This means that the diffusion along interfaces (similar as the diffusion at grain boundaries) is much faster than the volume diffusion in the films. When the number of layers is larger and the film thickness is smaller, the amount of interface areas is higher, and thus the diffusions at interfaces are more and more important.

The terms of ‘self-diffusion’ and ‘inter-diffusion’ are used in the field of diffusion phenomena. Self-diffusion is a random movement of atoms within a pure material. It can happen even without any concentration gradient ^[Askeland]. Interdiffusion is the diffusion of different atoms in opposite directions occurring for example at interfaces between different materials. The term of ‘diffusion’ is usually used to describe the movement of atoms A in solution B, especially for the movement of impurities in the matrix material. While interdiffusion emphasizes both the movement of atoms A to material B as well as that of atoms B to material A, especially these two movements have comparable rates. Usually, interdiffusion coefficients (e.g. D_{AB}) are not equal to the diffusion coefficients (e.g. D_A (A in B) or D_B (B in A)). Only when one of them is small, then the interdiffusion coefficient can be similar to one of them.

2.5 Hume –Rothery laws and electron phases

In this part, the fundamentals of Hume –Rothery rules and electron phases are given. More details can be found in the textbook of Cahn and Haasen ^[Cahn].

2.5.1 Hume- Rothery laws

According to many experimental data which were mainly obtained on copper and silver alloys, the essential conditions for the existence of solid solutions were summarized as Hume-Rothery laws ^[Hume]:

- 1) The difference between the atomic radii of the elements involved should be less than ~ 15%, otherwise the solid solubility is restricted. It is also known as 15% rule.
- 2) The difference in electronegative (or the valence electron density) of the constituents should be small.
- 3) The electron concentration, which determines the extent of the solid solubility and the stability of the intermetallic phases, can be revealed by the valence electron concentration m . m is the number of all valency electrons in the alloy per number of atoms. For example, in an A-B system, the m can be calculated by

$$m = e_A \cdot x + e_B \cdot (1-x) \quad (2.10)$$

Here x is the concentration of element A, e_A is the number of valence electrons of an atom A, $(1-x)$ is the concentration of element B with valence electrons e_B per atom.

2.5.2 Electron phases

Electron phases, also called as electron compounds, are intermetallic phases with a wide solid solubility. They are mostly alloys of noble metals (Cu, Ag, Au) with metals which have valence electrons in the s or p level. With the typical characteristic of 'wide solid solubility', electron phases require Hume–Rothery laws to explain their behaviors.

For the alloys of noble metals with elements having s or p valence electrons, one common phenomenon is that the structures of the stable solid solubility is different from face-centered cubic (FCC), body-centered cubic (BCC), complex cubic to hexagonal closed-packed (HCP) structure, when the valence electron concentration (m) of the stable phases are in the region of $1 \sim 1.32$, ≤ 1.48 , ≤ 1.54 , and ≤ 1.75 , respectively^[Laissardieress]. Based on Hume–Rothery laws, a large number of studies have been done to understand the development of the lattice parameter versus the valence electron density m for different structure domains^[Jones].

Jones^[Jones] performed calculations about the primary solid solubility of Cu based alloys. The main assumptions of his model are:

- 1) the near-free-electron approximation is extended from pure metals to random solid solutions;
- 2) the rigid-band condition is applicable to alloys, i.e. the shape of the density of states curve $N(E)$ for a pure solvent remains unchanged during alloying and the band gaps in the Brillouin zone do not change in magnitude, only the number of loose-bound electrons is changing.

The stability of the electron phase is related to the interaction between the Fermi sphere and contacting the Brillouin zone ^[Jones]. When the Fermi sphere is contacting the Brillouin zone, the density of state will start to decrease. Therefore, it is more favorable for the further filled electrons to occupy the Brillouin zone belonging to another structure. This explanation connects the Fermi surface with Brillouin zones for resulting in a maximum value in the density of states, and it has been generally accepted that the stability of electron phases is linked with the interaction of the Fermi surface and the Brillouin zone.

Combining what has been found that, (i) the values of valence electron concentration is related to the free-electron concept of the Fermi surface; and (ii) the interaction (contact) between the Fermi surface and the Brillouin zones will affect on the stability of the electron phases, with the third rule of Hume-Rothery laws, a relationship of the valence electron concentration, the structure and the chemical composition can be found. During the alloy process, the chemical concentration is changed gradually, and the value of m is modified if the elements alloyed have different valence electron numbers, and then the Fermi surface will keep changing / deforming. When the increasing Fermi sphere has not reached any boundaries of the Brillouin zones, then the structure will not be changed. When the Fermi surface contacts the principle faces of the Brillouin zone, then the old structure may break down and a new structure might be energetically more favorable. Before the structure transformation occurs, m might have been varied in a specified broad region. Thus the alloy phase (electron phase) will exist stable with a wide chemical composition. This is a main character of electron compounds.

2.6 Cu–Al system

In metallurgy, the Cu–Al binary system is a common and important alloy system. Six equilibrium intermetallic phases, i.e. $\text{CuAl}_2(\Theta)$, CuAl , Cu_3Al_2 , $\text{Cu}_{33}\text{Al}_{17}$, Cu_9Al_4 , and Cu_4Al , are known so far and form in this system. Besides them, some metastable phases, Guinier-Preston zones (GP), also exist in this system. The basics will be summarized in this chapter. More detailed information is given in the textbook of Cahn and Haasen^[Cahn].

2.6.1 Phase diagram

Fig.2.6 displays the Cu-Al binary phase diagram which shows that six equilibrium intermetallic phases can form depending on the chemical concentration. The intermetallic alloy phases can be stable for temperatures ranging from RT to 360°C at least.

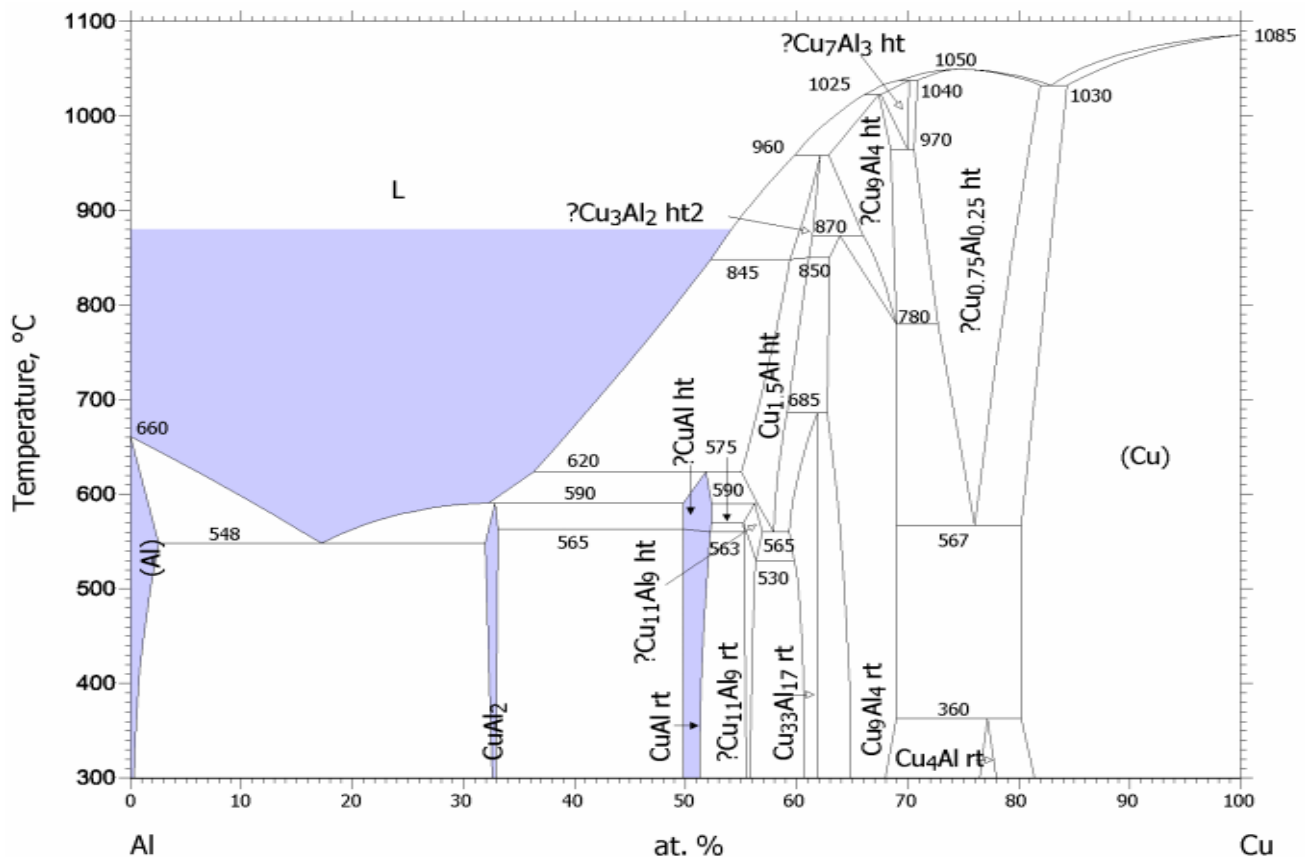


Fig.2.6 Cu-Al binary phase diagram

2.6.2 Structures of the intermetallic phases in the Cu-Al system

The six equilibrium intermetallic phases in the Cu-Al system have different crystal structures and lattice parameters. All structural data for them are summarized in Table.2.1 (a). The data of the metastable phases and pure Cu and Al are listed in Table.2.1 (b).

(a) intermetallic phase	CuAl ₂ (Θ)	CuAl	Cu ₃ Al ₂	Cu ₃₃ Al ₁₇	Cu ₉ Al ₄	Cu ₄ Al
crystal system	tetragonal	monoclinic	hexagonal	rhombohedral	cubic	cubic
lattice parameters						
a (Å)	6.067	12.066	8.292	8.672	8.704	6.260
b	6.067	6.913	8.292	8.672	8.704	6.260
c	4.877	4.105	4.974	8.672	8.704	6.260
α (°)	90	90	90	89.77	90	90
β	90	90	90	89.77	90	90
γ	90	124.96	120	89.77	90	90

(b) phase	Θ'' (GP II)	Θ'	Cu	Al
crystal system	tetragonal	tetragonal	cubic	cubic
lattice parameters (Å)				
a	4.04	4.04	3.615	4.049
b	4.04	4.04	3.615	4.049
c	7.68	5.80	3.615	4.049
α (°)	90	90	90	90
β	90	90	90	90
γ	90	90	90	90

Table.2.1. (a) crystal structure parameters of the six intermetallic phases occurring in the Cu-Al system, and (b) structure parameters for GP zones, Cu and Al.

2.6.3 Guinier-Preston zone

The precipitation processes in supersaturated Al with Cu in solid solution (concentration of $C_{Cu} \leq 2.5$ at %) are well known^[Cahn]. The stable precipitate phase in equilibrium with Al is $CuAl_2$ (Θ), which has a tetragonal structure and a 50% mismatch with Al. On account of the high interfacial energy, $E_{\alpha\beta} > 1J/m^2$, the critical nucleation energy ΔF is also very large. This permits the formation of a series of metastable intermetallic phases, which possess lattice parameters similar to Al. They are called GP I (Guinier-Preston zone of type one), GP II (Θ'' or Guinier-Preston zone of type two) and Θ' , and appear in this order^[Cahn]. The name of 'GP zones' originally comes from the Cu-Al system, but is now used also for other alloy systems where similar structure phases form, for example, in the Al-Ag alloy system.

Schematic drawings for the metastable intermetallic phases occurring in the Cu-Al alloy system are given in Fig. 2.7 and 2.8. GP I has a slightly adjusted Al structure, in which Cu atoms replace the positions of Al in some $\{100\}$ planes. Lattice distortions are induced by the very high size difference between Al atoms and Cu atoms, as illustrate in Fig.2.7

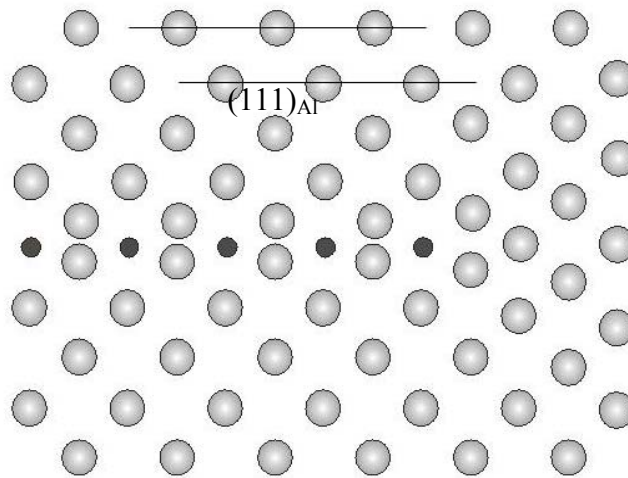


Fig.2.7 A section of GPI in the view direction of $[001]_{Al}$. The gray circles represent Al atoms and the black circles represent Cu atoms.

Comparing the structure models of Fig.2.8 with the crystal parameters in Table.2.1 (b), it can be seen that the tetragonal GP II (Θ'') has the same lattice parameters a and b as those of Al, and thus it is coherent to pure Al in $\langle 001 \rangle$ directions. The GP II can also be understood as a superlattice of GPI, in which Al atoms in $\{100\}$ planes are replaced by Cu atoms every fourth layer.

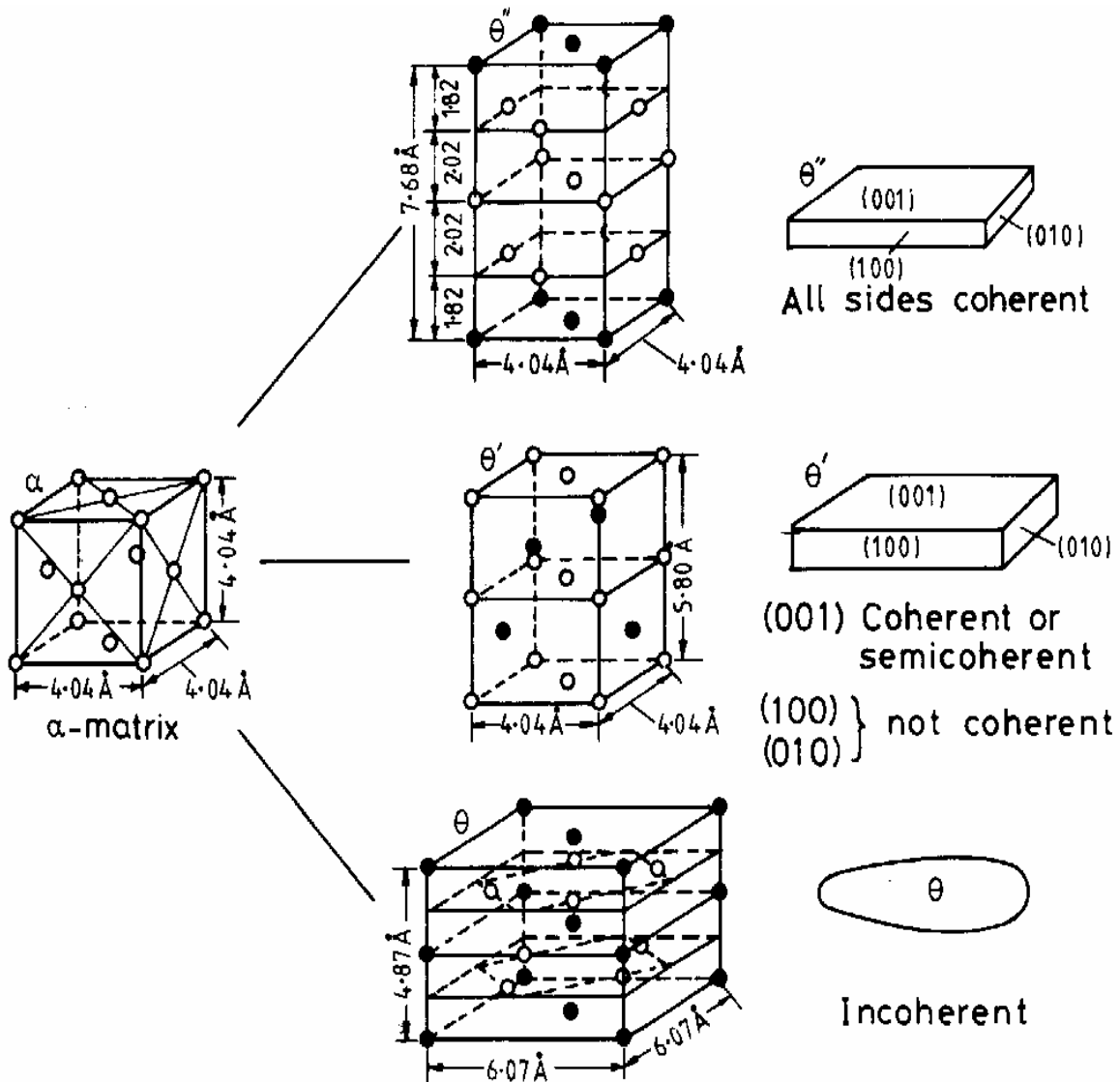


Fig.2.8 Schematic drawings of the structures of Θ'' (GP II), Θ' and Θ (CuAl_2) taken from [Shui]. Θ'' and Θ' are metastable, while Θ is an equilibrium phase. All of these phases form from the Al matrix. The coherence degree between them and pure Al is decreasing in the order of Θ'' , Θ' to Θ .

The Θ' phase is also coherent with Al in the $\langle 001 \rangle$ direction, however, along this direction, the pure Cu layer and pure Al layer stack alternately. At the same time, the layers filled by Cu atoms have different arrangements compared to the layers filled by Al atoms. So the Θ' phase is only semi-coherent with pure Al in $\langle 001 \rangle$ direction.

As to the Θ phase, the Al atoms in it have totally different arrangements compared to those in pure Al and the precipitates are incoherent.

Nevertheless, it can be understood that in the Cu-Al system, GP zone phases (GPI, GPII and Θ') are able to form from the Al matrix along $\langle 001 \rangle$ directions, since they are coherent or semi-coherent with pure Al in this direction.

Chapter 3

Literature overview

According to the aim of the present work, the literature research is summarized in two parts, (a) the interfaces in layered metal films (section 3.1) and (b) the characteristics of Cu-Al film systems (section 3.2). After that, the main aim of the present work will be described (section 3.3).

3.1 Metal-metal interfaces in layered films

Compared to the same material in bulk state, thin film samples may have different properties, and thus a large number of research studies have been performed to investigate the electronic structures [Auciello], [Nakagawa], magnetic properties [Tersoff], [Gubbiotti], mechanical behaviours [Vinci], [Tsakalagos], interdiffusions [Tu], [Ramana] and reactions [Polak] in thin films. It has been found that the behaviours of the films are strongly influenced by the interface structure. For instance, deformation and / or dislocation generation tend to occur at the coherent and / or semi-coherent interface to relax the strains from the lattice mismatch between the two different materials. Diffusion is also a common phenomenon taken place through the interfaces, where the rate of diffusion depends on the structure of the interface. Therefore the determination of the characteristics of the metal-metal interface(s) is the predominant aim in the studies for layered metal films and for this purpose several techniques were applied. For example, to study the atomic structure at interfaces in Ni-Ag [Merkle] and Al-Ag [Howe] systems HRTEM [Merkle] and simulation [Howe] were performed. XRD and in-situ XRD [Hamm] were used for phase identification of solid state reactions in Cu-Al [Clemens], [Hamm] and Ag-Pd [Tu 1977]

systems. The reconstruction at the interface between ultra thin metal films and metal substrates (Ag/Cu, Cu/Ru) was investigated by STM^[Tsay]. RBS^[Campisano] and EDS^[Chen Z] measurements were used to determine the chemical composition in the Cu-Al system while AES^{[Wildman], [Kief]} and XPS^[Campbell] allow to study the electronic properties (Co-Cu^[Kief] and Pd-Ru^[Campbell]).

Many research works have been done in metal-metal systems, but only the studies relevant to the present work will be described in this chapter. The formation of dislocation and diffusions at metal-metal interfaces have been investigated since several decades; the basics were described in chapter 2. However, it is also found that (i) the first few layers next to the interface may reconstruct, that (ii) an amorphous layer can form and then transform into thermodynamic stable alloy phases, and that (iii) the formation of a metastable phase can occur. In the following sections, 3.1.1 to 3.1.3, reconstruction (3.1.1), amorphization (3.1.2) and metastable phase formation (3.1.3) at metal-metal interface (3.1.1) will be summarized in detail. Section 3.14 is dedicated to FCC-HCP transformation.

3.1.1 Reconstruction at metal-metal interfaces

Reconstruction at metal-metal interfaces has been investigated in various bilayer systems, e.g. Ag/Cu (111)^[Meunier], Ag (111) / Ru (0001)^[Ling], Au/Ru (100)^[Radeke], Au/Ni (111)^[Jacobsen], Co/Pt (111)^[Lundgren], and Cu/Ru (0001)^[Günther]. In these studies one metal act as the substrate, the other is deposited as a thin film with a few monolayers (ML) thickness. In this case, the substrate influences the atom stacking behaviour of the films and it is found that the atomic stacking behaviour changes with the film thickness. Most of these samples were deposited by thermal evaporation at RT, followed by annealing at higher temperatures. In the mentioned research works, STM is the predominant employed technique. *In-situ* facilities were also available in some of the STM experiments^[Pötschke].

In couples of two different FCC metals, the interface can reconstruct in various ways. For Ag/Cu (111) (mismatch 13 %), it is found that the strain is relaxed by formation of Cu vacancies^[Meunier]. At the surface layer of the Cu wafer, four or five vacancies form per unit cell^[Meunier]. In the Au/Ni (111) system (misfit 16 %), the dislocations at the interface are controlled by the interfacial energy rather than the strain between the two structures^[Jacobsen]. For Co/Pt (111), an alloy film (CoPt)

formed at the interface where both single and double stacking faults occur [Lundgren]. For this system (mismatch 10%) the thickness of Co was only 2 ML [Lundgren].

Ling *et al.* [Ling] studied Ag (111)/Ru (0001) which is an example of a FCC-HCP joint (mismatch 6.5 %). The interface showed a different reconstruction behaviour compared to the above mentioned FCC couples. The first layer of Ag is reconstructed into a symmetrical structure and contains long threading dislocations, while Ag atoms in the second layer have the bulk spacing of Ag but are shifted slightly from the ideal positions [Ling]. Günther *et al.* studied a similar system, Cu (111)/Ru(0001) (misfit 5.5 %), and they found that the relaxation behaviour is gradually changing with the film thickness [Günther].

Radeke *et al.* investigated Au (100)/Ru (10-10) (mismatch 7 %) which also belongs to the FCC-HCP systems [Radeke]. The difference to the study of Ling *et al.* [Ling] is that the planes parallel to the interface are not the close packed planes. The interesting phenomenon is that Au atoms reconstruct in all layers with exception of the first layer next to substrate, i.e. the layer at the interface [Ling]. Starting from the second layer, Au transforms from (100)_{FCC} to (111)_{FCC}. The authors argued that when the film grows thicker, the strain becomes larger, and thus the reconstruction occurs at the upper layers [Radeke]. In contrast, Au(100)/Pd(100) [Palmberg] and Au (100)/Pt(100) [Sachtler] showed different behaviours, i.e. only the layers at the interface reconstructed.

Though the results from different systems are various, the common conclusion is that the atoms at the metal-metal interface tend to reconstruct to relax the strain, and many FCC-FCC couples in [111] direction presented a HCP shaped area after atomic rearrangements [Lundgren], [Meunier] [Tsay].

3.1.2 Amorphization at metal-metal interfaces

In 1983, Schwarz and Johnson [Schwarz] reported for the first time the solid-state amorphization (SSA) in an Au-La multilayer system after medium temperature annealing. They found that the polycrystalline Au / La multilayer films, which were deposited at 0°C, changed to an amorphous state after annealing at 50 to 80°C. According to the studies from Schwarz and Johnson and also from other groups, Johnson [Johnson] summarised the proposed criteria for this phenomenon in binary metal system. These criteria are: a large and negative heat of formation (ΔH_f), a large atomic size difference between the involved atoms, anomalous diffusion, and low mobility for one of the two elements in

the amorphous phase. However, other research groups ^{[Clemens], [Egami]} claimed that amorphization can occur even when the atomic size ratio is around one.

Besides the Au-La system, SAA was observed later in various binary systems, such as Cu-Ta ^{[Liu], [kawk], [Gong], [Zeng 2002]}, Au-Ta ^[Pan 1995], Ni-Mo ^[Zhang ZJ], Ni-Ta ^[Zhang Q], and Cu-Nb ^[Pan 1996]. It is interesting to note that the system Ni-Mo has a small negative ΔH_f , and that Cu-Ta and Cu-Nb systems even have a positive ΔH_f . For the Au-Ta system, the Au atoms have a similar size than the Ta atoms. Al-Pt have a similar atomic radius but not anomalous diffusion ^[Blanpain]. All of these later results were partially contrary to the original criteria from Johnson.

Thermodynamic calculations have been performed in the research field of SSA. Most of the authors used first-principle or molecular dynamic calculations. Benedictus *et al.* ^[Benedictus] stated that the energy of a crystalline-amorphous interface may be lower than the energy of a crystalline-crystalline interface. This lower energy for the crystalline-amorphous interface provides a driving force for SSA, as long as the amorphous product layer is not too thick. This explanation is in agreement with experimental data reported by Meng *et al.* ^[Meng] and Vrdenburg *et al.* ^{[Meng], [Vrdenburg]}. Kwak *et al.* ^[Kwak] proposed another model. This states, (i) the amorphous phase can only form when its Gibbs free energy is lower than that of the multilayer film, and (ii) the kinetic factor is given by the effective atomic size ratio. Lin *et al.* ^[Lin] tried to predict the conditions for SSA at interfaces in binary metal systems, taking into account the interfacial energy and diffusion as well as the melting point. Applying this model to the Cu-Ta binary system, the calculated thickness of the amorphous layers is less than 5.5 nm ^[Lin]. This calculated value is in good agreement with experimental results from Kwon *et al.* ^[Kwon], who used HRTEM and nanoprobe EDS techniques to investigate the Cu-Ta system. They found that the disordered layer between Cu and Ta was up to 4 nm in thickness when the layered film was annealed between 400 ~ 600°C.

From Schwarz and Johnson ^[Schwartz], Clemens *et al.* ^[Clemens], Benedictus *et al.* ^[Benedictus], Kwak *et al.* ^[Kwak] to Lin *et al.* ^[Lin], the criteria for SSA were further developed. It is believed that SSA may occur when the amorphous-crystalline interface energy is lower than the crystalline-crystalline interface energy, independent whether ΔH_f is negative or positive. Different diffusion rates at the amorphous layer are still a key factor, while the limitation for the atom size ratio is less strict.

It should be noted that the amorphous layer can transform into an equilibrium alloy phase ^[Schwarz] when further annealing is performed at higher temperatures. Some experiments show that

ordered structures may form at metal-metal interfaces if the Gibbs energy is low. This will be described in the next part.

3.1.3 Metastable phase formation at metal-metal interfaces

Ion-beam mixing (IM) is a process far from equilibrium. Many new metastable alloys, which could not be obtained by common techniques, can be prepared by IM. Besides metastable phase formation, the non-equilibrium process of IM may also result in changes in solid solubility, an enhancement of the defect density, the formation of amorphous phases, and changes in the microstructure of alloys [Lilienfeld], [Larsena], [Knapp]

Liu and colleagues worked on the metastable phase formation at metal-metal interfaces by IM. At RT multilayer films (e.g. Ni-Ru^[Li JH], Ag-Co^[Li ZC], Au-Co^[Yan] for FCC-HCP systems, Ag-Ni^[Li ZC 2000] for FCC-FCC systems, and Y-Nb^[Chen YG] for HCP-BCC systems) were deposited on fresh cleaved NaCl by electron gun evaporation. The total thickness of the multilayer was 40 ~ 50 nm, and the composition of the films was controlled by adjusting the thickness of the individual layers. After deposition, a 200 keV Xenon ion-beam was used to mix all the atoms in the different layers together. The temperature during this process was ranging from 77 to 500 K. The results from selected area diffraction (SAD) and EDS experiments indicated that after IM the layered metal films changed into some metastable alloys, which have different crystal structures compared to the initial pure metal matrixes.

In the material systems studied, the two matrices are immiscible. The new phases formed after ion-beam mixing, but not after film deposition. The new phases were not in equilibrium, and the structures and compositions depended on the ion beam dose^[Li ZC 2000] and chemical compositions of the initial matrixes^[Zhang ZJ 1995]. The Gibbs-free energies for the metastable phases with certain chemical composition range were calculated by Liu and co-workers^{[Li JH], [Li ZC], [Yan] [Zhang ZJ 1995]}. Depending on the composition, the minimum Gibbs-free energies varies with the structures, i.e. solid solution, crystalline, or amorphous. Fig. 3.1 shows as an example curves calculated by Yang et al. [Yang]

Li and co-workers explained the formation of metastable phases with the help of Hume-Rothery laws^{[Yan], [Li ZC 2000]}. They found that the observed Ag₃Ni HCP phase occurring in the

transformation of their Ag / Ni film system can be considered as a well-defined Hume–Rothery metastable electron compound phase.

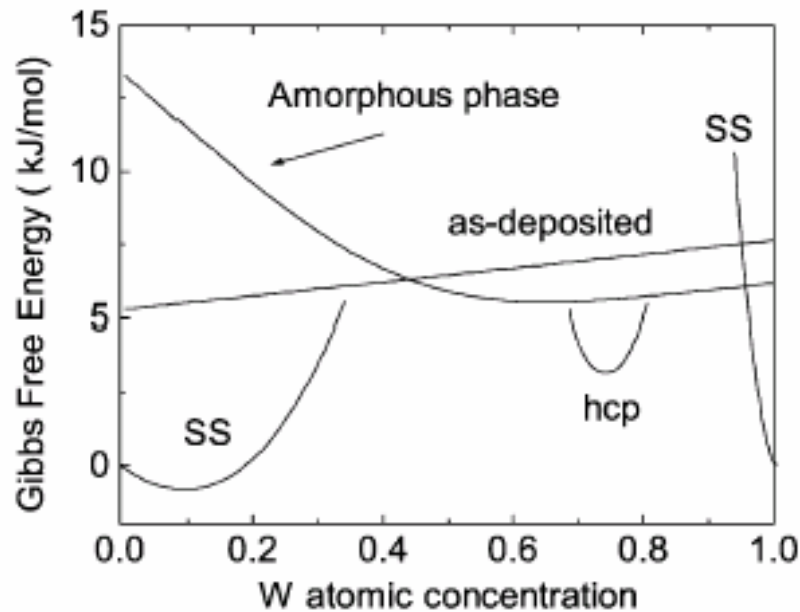


Fig.3.1 The calculated free-energy diagram of the Ni–W system taken from [Yang]. Here SS means solid solution.

In the IM process, the thickness of the alloy films is limited by the ion sources and the bombardment energy. As a derivation of the IM technique, ion beam assisted deposition (IBAD) [Hirvonen], [Smidt], [Sonnenberg] was also widely applied to prepare metal films such as Ag^[Marinov], Nb^[Roy], coatings (i.e. VO₂ on sapphire^[Case]) and metastable compounds (for example, group IV B nitrides^[Johansson]). Compared to IM, IBAD is also a process far from equilibrium, however, it is accompanying the whole film deposition process and is not only used after deposition as IM. In IBAD processes, atoms can be mixed as soon as they reach the substrate or the bottom of the former layer, therefore there is no limitation to the thickness of the alloy films and the required energy is much lower than for IM.

Zhao *et al.* and Zeng *et al.* did a series of works (e.g. Cu-Nb^[Zeng 2001], Ni-Nb^[Zhao 2004] and Cu-Mo^[Zhao] for FCC-BCC systems) to investigate the metastable phase formations in layered films produced by IBAD. The temperature of the substrate (NaCl) was RT or lower than 200 °C. The films were deposited by electron gun evaporation. Though IBAD is different from IM, the experimental results (i.e. metastable phase formation) were similar to what had been observed in the different systems treated by IM. The explanation for the formation of metastable phases was the same: the Gibbs free energies depend on the structure and composition, thus metastable phases may form with special compositions and certain structures.

It should be noted that besides triggering a phase formation at interfaces, IM and IBAD can also induced SSA at metal interfaces as reported by Zeng *et al.*^[Zeng 2002].

3.1.4 FCC-HCP transformations

In both, bulk materials and films, the transformation between different structures may happen. As early as 1987, Dahmen^[Dahmen] explained the mechanism of FCC-HCP transformation by Shockley partial dislocation, which occur across (111) planes in the Al-Ag alloy system (for details see chapter 2). However, the original purpose of his work was applying the same mechanism to clarify the formation of martensite in FCC-BCC transformations. This explanation was also used in later works about martensite formation^{[Muddle], [Mahon], [Pond]}.

Howe and Mahon^[Howe] supported this mechanism for FCC-HCP transformation by HRTEM investigations of HCP precipitates (Ag₂Al) formed in an Al-15%Ag alloy. The orientation relationship between the matrix and the precipitates is $\{111\}_{\text{FCC}} \parallel (0001)_{\text{HCP}}$ and $\langle 110 \rangle_{\text{FCC}} \parallel \langle 11-20 \rangle_{\text{HCP}}$, i.e. the close packed planes and directions are parallel to each other. The Shockley partial dislocations are in the plane of $(111)_{\text{FCC}} / (0001)_{\text{HCP}}$ with the vectors of $1/6 \langle 112 \rangle$.

Besides the simple system of an Al-Ag alloy, Howe and Mahon^[Howe] also investigated a more complicated binary Ti-Al system, in which the structure transformation takes place between two reaction products, FCC TiAl and HCP Ti₃Al, but not between the original pure metal matrixes and the precipitates. Similar work had been done in a ternary metal alloy of Al-2wt%Li-1wt%Cu, and the results were the same: HCP Al₂CuLi precipitate on the (111) plane of the FCC Al matrix. In this

work, quantitative HRTEM simulations were used to investigate the chemical compositions in the transformed phases. However, analytical TEM was not applied to further prove the results.

Hirth and Pond^[Hirth] constructed a model for FCC / HCP bicrystal, to investigate the influence from defects on the structure and phase transformation. At the FCC/HCP interface, the atom stacking ordering has six different possibilities along the close-packed-directions $[111]_{\text{FCC}} / [0001]_{\text{HCP}}$. Thus the step and dislocation have various combinations. After analyzing them by crystallography, it is suggested that the step and dislocations at the interface can yield a description of the interface flux for diffusion growth.

3.2 Cu-Al film systems

Research studies of Cu-Al film systems started from the 70's of the last century, since they are frequently used as conductor layers in microelectronic devices and/or utilize specific properties of each individual component.

In most of these studies, physical methods (sputtering or thermal evaporation) were used to fabricate Cu-Al bilayer films^{[Gershinskii], [Campisano], [Hamm], [Jiang]}. The employed substrates were glass, quartz, NaCl, SiO₂ and MgO. In some of this research works, pure metals (Cu or Al) were also applied as wafers^{[Campisano], [Geng]}. Layered Cu-Al films were deposited at room temperature in most of the experiments to avoid the formation of intermetallic phases. In some studies^{[Gershinskii] [Rajan]} the substrates were heated to higher temperatures during the deposition of Cu films, and then cooled to lower temperatures during the subsequent growth of Al films. In this way, the adhesion between the Cu film and the substrates was improved. All of the bilayer films were polycrystalline^{[Gershinskii] [Rajan]}. After deposition, a series of annealing experiments had been performed. In the annealing the temperature ranged from 4.2K^[Rayne] to 893K^[Jiang]. To characterize the films, commonly used techniques were XRD^{[Campisano], [Simic], [Broeder], [Vandenberg], [Funamizu], [Hentzell], [Hamm], [Jiang], [Geng], [Fadnis], [Markwitz], [Chen HY]}, RBS^{[Campisano], [Hentzell], [Hamm], [Markwitz], and Su]}, TEM^{[Gershinskii], [Rajan], [Hentzell], [Jiang], [Chen]} and scanning electron microscopy (SEM)^{[Chin], [Markwitz], [Chen Z]}. Besides them, anodic etching^[Gershinskii], AES^[Shearer, and Su], AFM^[Markwitz], resistivity-measurements^[Rayne, Shearer, and Chen, Z], XRR^[Chen]

^{HY]} and EXAFS ^[Chen HY] investigations had also been used. *In-situ* XRD and RBS have been also employed in some experiments ^{[Hamm], [Vandenberg]}.

According to earlier studies ^{[Simic], [Broeder], [Funamizu], [Hentzell], [Jiang], [Fadnis], [Markwitz], [Rayne]}, the common results are: (i) the bilayer films were polycrystalline; (ii) independent on the initial chemical composition and the annealing rates, CuAl₂ is the phase which can form at or below 200°C. For the samples with excess Al, no other phases will form after further annealing. For the samples with excess Cu, CuAl and Cu₉Al₄ formed sequentially during the further annealing at 200°C; (iii) the kinetic theory for Cu-Al intermetallic phase formation are combined with diffusion and interdiffusion rates; (iv) no work mentioned that any intermetallic phase can form in Cu-Al layered films at room temperature. Especially, Simic *et al.* emphasized this last point in their work ^[Simic]. In a few studies, some additional features were found: (i) the formation of β'-CuAl_x, which has a hexagonal structure and is a kind of superlattice of cubic FCC-ordered β-Cu₃Al, was only reported by Vandenberg *et al.* ^[Vandenberg], (ii) Hamm and Vandenberg ^[Hamm] consisted that CuAl₂, Cu₃Al and Cu₉Al₄ can form simultaneous. Geng and Oelhafen ^[Geng] also indicated that the diffusion rate depends on temperature, and thus the composition of the formed phase would be influenced by the substrate temperature.

Several authors tried to provide a basis for predicting the sequence of phase formation in Cu-Al bilayers ^{[Gershinskii], [Campisano], [Hamm]}. It was found that the growth rates of CuAl₂ (and CuAl) obeyed a parabolic law and depend on the annealing temperature ^[Gershinskii]. When the temperature is around 150 °C, CuAl₂ forms and CuAl nucleates. Then CuAl will decompose to CuAl₂ and Cu at higher temperatures ^[Campisano]. At the end of 80's, Chen and Heald ^[Chen HY] suggested that CuAl₂ is the first phase which grows and that also simultaneously some intermediate phase can form, but they were not able to detect them due to the limited sensitivity of the applied techniques (XRD or RBS). Therefore, they used XRR and EXAFS, which are more sensitive compared to conventional XRD and RBS, to investigate the interface structure of Cu-Al films. The detectable reaction region is as thin as 3nm. It was found that 'the interfacial structure is multiphased, but not a simple combination of the standard phase' ^[Chen HY]. However, they did not give further information about the contents or the average chemical composition of the 'multiphase'.

From 90's, less fundamental work has been done in Cu-Al layered film systems. Research groups found that, (i) Al can enhance (111) Cu texture ^[Chin]; (ii) the adhesion between Cu-Al bilayer films and Si substrates ^[Chen Z] can be improved by using a nitrogen atmosphere during annealing; (iii)

in different orientations (parallel and perpendicular to the film surface), the magnetoresistance of Cu-Al multilayer with various thickness (350 ~ 520 nm) were measured between 2.5 and 20 K in a magnetic field up to 8 T and was found to be anisotropic [Fadnis]; (iv) formation of the intermetallic phase reduces film roughness, while an oxide phase formation has an opposite effect [Markwitz].

According to the results from literature, it is still an open question which initial phase forms at the interface between Cu and Al layers. Therefore, the main aim of this thesis is to study the initial structure of the interface between Cu and Al.

3.3 Main aim of this work

Most of the previous researches on Cu-Al film systems were performed at samples annealed at temperatures higher than 200°C. They revealed the thermodynamic and kinetic properties, atomic structures, diffusion and reactions of these samples in detail. Until now only a few studies dealt with the Cu-Al film system at room temperature. However, the results are not consistent to each other which is most likely due to differences in methodology. In addition, the interface structure was not investigated at an atomic level. Therefore, the objective of this work is to study in detail the characteristics of the interface between Cu and Al films at RT.

In this present work, layered films are deposited by MBE or sputtering on two kinds of substrates, Si (001) and sapphire (0001), in order to obtain epitaxial Cu/Al layered films. The epitaxial quality will determine which samples are suitable for fundamental studies on the phase formation at the Cu/Al interface at room temperature. The questions which will be addressed are whether diffusion, amorphization, lattice reconstruction or phase (trans)formation can occur at the Cu/Al interface even at room temperature, and whether these phenomena lead to a specific interface structure.

The methods which will be employed to answer these questions are XRD, XRR, CTEM, HRTEM and corresponding quantitative image simulations, as well as analytical TEM. XRD will be used to determine the phase formation and the out-of plane orientation relationship between Cu and Al films. To check the roughness of the interface, XRR will be applied. The morphology of the films will be studied by CTEM. The microstructure of the Cu/Al interface is investigated at an atomic level by HRTEM. Using EDS and EELS methods in analytical TEM, the chemical composition of the

interface will also be analyzed. *Ex-situ* annealing and *in-situ* heating experiments will be used to examine the behaviors of the interface at higher temperatures.

Chapter 4

Experimental methods and sample preparation

In this chapter, the experimental methods, the details of the film deposition and the TEM specimen preparation techniques will be introduced. In addition, the fabrication and identification of the reference sample will be presented.

4.1 Experimental methods

X-ray diffraction, total X-ray reflectivity, atomic force microscopy and transmission electron microscopy are the main experimental methods used to characterize the samples in the present work, and these will be described briefly in the following section.

4.1.1 X-ray diffraction

Two different working modes of the X-ray diffraction were applied in this work, which are θ - 2θ scans and pole figures. A Philips X'Pert XRD, which has a proportional counter and a parallel beam and which was operated at 45 KeV, was used for the measurements.

Generally, in film systems θ - 2θ scans are used to determine the out-of-plane orientation relationship between the different layers e.g. between the substrate and all crystalline films on it, or between the film layers. Here, the 'plane' is the surface of the substrate or the interface between layers. As Fig.4.1 (a) illustrates, when θ - 2θ measurements are performed, the incident angle θ of the X-ray beam will be continuously changed, by rotating the sample or turning the X-ray source. The

angle ψ and ϕ are fixed. When the incident angle achieves a certain value and the Bragg condition (Eq.4.1) is satisfied, the incident X-ray will be reflected on specific atomic planes, and a strong signal will be detected. Accordingly, a peak in the XRD θ - 2θ scan profile will appear. During the variation of θ , different peaks will occur corresponding to different planes which fulfil the Bragg condition. This is given by:

$$2 d_{hkl} \sin\theta = n\lambda \quad (4.1).$$

Here d_{hkl} is the d-spacing of the lattice plane (hkl), θ is the angle between the incident beam and the plane normal, λ is the wavelength of the X-ray and n is an integer.

Pole figures are applied to check the in-plane orientation of the single layers. As Fig.4.1 (b) shows, the angle ψ and ϕ are changed while the incident angle θ is fixed at the Bragg angle for a certain plane. Peaks in the pole figure will also occur when the Bragg condition is satisfied. Combining the values of ψ and ϕ and the symmetry of the pole figures with the crystal structures of the materials, the preferred in-plane orientation of the films can be determined.

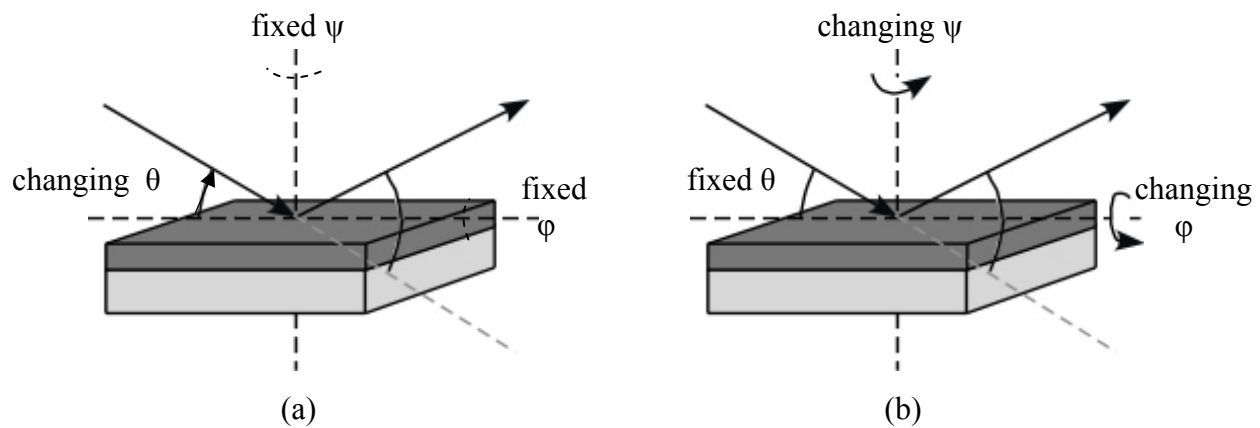


Fig.4.1 Schematic drawings for (a) θ - 2θ scan experiments and (b) pole figure measurements.

4.1.2 X-ray reflectivity

As for visible light, the index of refraction n is used to describe the reflectivity of X-rays. For X-rays [Parratt], [Tolan], [Schreiber],

$$n = 1 - \delta + i\beta \tag{4.2}$$

with

$$\delta = (\lambda^2/2\pi) * r_e\rho_e \tag{4.3}$$

and

$$\beta = (\lambda/4\pi) * \mu_x \tag{4.4}$$

Here $r_e = 2.818 * 10^{-15}$ m is the classical electron radius, ρ_e is the electron density of the material, μ_x is the absorption length, and λ is the wavelength of the X-rays. For simplicity, β , which is usually small, will be neglected. In this case, $\delta > 0$ and $n < 1$, which leads to the phenomenon of total external reflection for incident angle α_i smaller than the critical angle α_c . The critical angle is given by

$$\alpha_c = C * (2\delta)^{1/2} \tag{4.5}$$

Here C is a constant. Fig.4.2 is a simplified drawing showing the refraction in layered structures with different n .

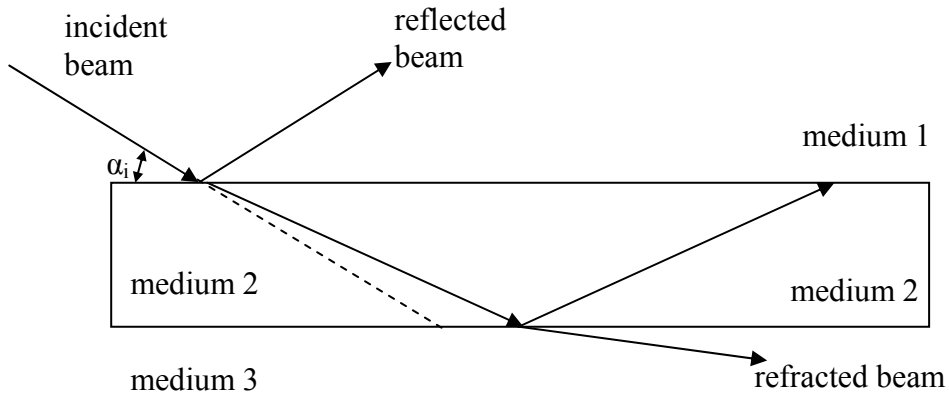


Fig.4.2 Sketch of the reflection and refraction in a layered structure. The mediums there have different indexes of refraction.

According to Eq. (4.3) and Eq. (4.5) , it is obvious that the critical angle is essentially determined by the electron density but independent of the structure or orientation. Typical values for δ and α_c are 10^{-5} - 10^{-6} and $0.1 - 0.5^\circ$, respectively.

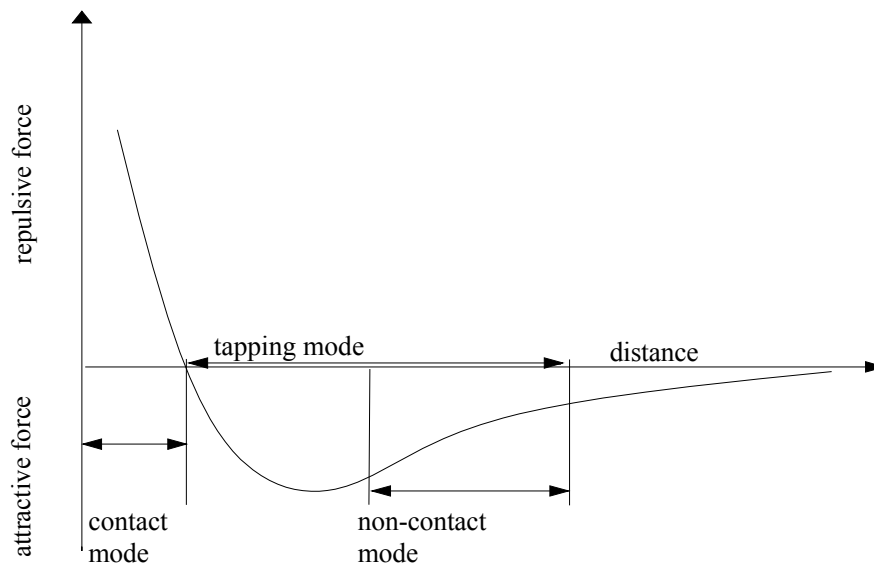
In layered structures, since the electron density varies with the materials in the different layers, the refraction angle will be changing accordingly. Assuming the sum of the intensities of the incident, reflected and refracted beam are fixed, then the reflectivity (intensity ratio of reflected and incident beam) might vary with the depth of the incident beam. XRR is sensitive to reveal changes in electron densities of the layers by measuring the reflectivity versus thickness. Therefore, it is a powerful tool to detect reaction layers or interlayers with a limited volume.

4.1.3 Atomic force microscopy

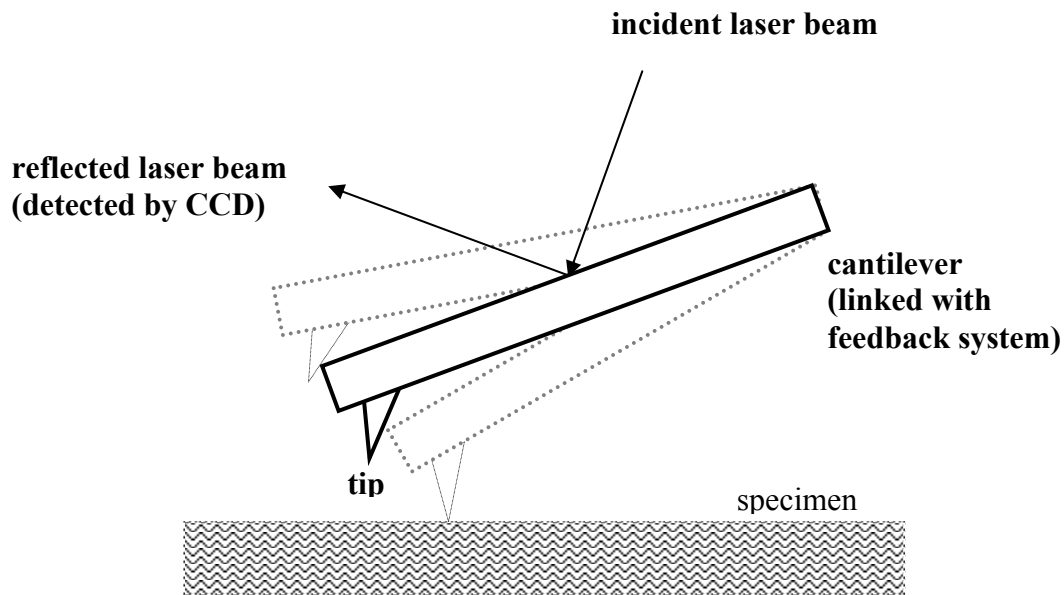
In an AFM, a tip which is attached to a cantilever is scanned across the sample surface. Depending on the force acting between the tip and the sample surface, the bending of the cantilever changes and can be detected. These forces can be Van der Waals forces, magnetic, electrostatic friction and capillary forces, and are repulsive or attractive (Fig.4.3 (a)). The roughness of a sample can be measured due to the strong distance dependence of those forces. A basic drawing of an AFM and the different possible modes for operation are given in Fig.4.3 (a and b). There are three modes for AFM measurements, i.e. contact mode, tapping mode and non-contact mode.

In contact mode the tip is scanned in close contact across the sample surface. For this case, repulsive forces are acting between the tip and the sample. The tip is attached on a cantilever, which is pressed against the sample surface with a piezoelectric crystal. As Fig.4.3 illustrates, a laser beam is reflected on the cantilever. The intensity of the reflected laser light is measured by a position sensitive detector. In the constant force mode, an amplifier applies a voltage to the piezoelectric crystal to adjust the position of the tip in order to keep the force constant. The voltage applied to the piezo is a measure of the roughness of the surface.

In non-contact mode, the tip is scanned some distance above the sample surface. Attractive Van der Waals forces occurring between the tip and the sample are detected. The roughness of the sample is measured by scanning the tip above the detected surface.



(a)



(b)

Fig.4.3. (a) The distance dependent forces and modes used in AFM. (b) the sketch of an AFM. In the contact mode, the tip is touching the surface of the specimen. A certain distance is kept between the tip and the specimen surface in the non-contact mode. In tapping mode, the cantilever is oscillating above the surface of the sample, as the dotted lines indicate.

Tapping mode is another mode used in AFM. It overcomes the disadvantages from both, the contact mode that the surface of the sample is easily damaged, and the non-contact mode where the resolution is low. In the tapping mode, the tip on the cantilever does not have a constant distance from the surface, but is oscillating. Tapping mode images are obtained by the different oscillation amplitudes between the resonant amplitude of the cantilever and the measured one.

Independent of the modes, the measurement is done by a constant force or constant height. In case of constant force, bending of the cantilever is kept constant and the voltage of the piezo is regulated by a feedback loop to keep the bending constant. In case of constant height, the voltage at the piezo is kept constant and the bending of the cantilever is detected by the CCD-camera.

In this present work, AFM is applied to measure the surface roughness of the films in the tapping mode.

4.1.4 Transmission electron microscopy

TEM is the main experimental method applied in this work. Both the structure and chemical composition of the specimen are investigated by TEM together with image simulation and quantification of the data. For conventional TEM a JEOL JEM-2000FX (point-to-point resolution of 0.28 nm), for HRTEM a JOEL ARM-1250 (point-to-point resolution of 0.12 nm), and for analytical TEM a VG HB501UX STEM (scanning transmission electron microscopy) were used. More details about the microscopes are given by Dehm *et al.* [Dehm]. The different TEM techniques are described briefly in the next paragraph. More detailed information can be found in [Williams] and [Reimer].

A. Conventional TEM

Conventional TEM is used to investigate the thickness, morphology (of cross sectional samples) and the OR of the films and the substrate. The morphology and thickness is determined in the imaging mode, and the OR is detected by diffraction mode. Fig.4.4 illustrates these two modes. The image is observed on the viewing screen in the image mode (Fig.4.4 (a)). Changing the strength of the intermediate lens, the diffraction pattern is projected on the final viewing screen in the diffraction mode (Fig.4.4 (b)). In the image mode, usually an aperture is inserted at the back focal plane of the objective lens. It passes only the transmitted beam for bright field (BF) images, or a diffracted beam for dark field (DF) images. In the diffraction mode, usually a selected area diffraction (SAD) aperture

is positioned in the image plane of the objective lens, as Fig.4.4 (b) shows, and only the selected area is contributing to the diffraction pattern.

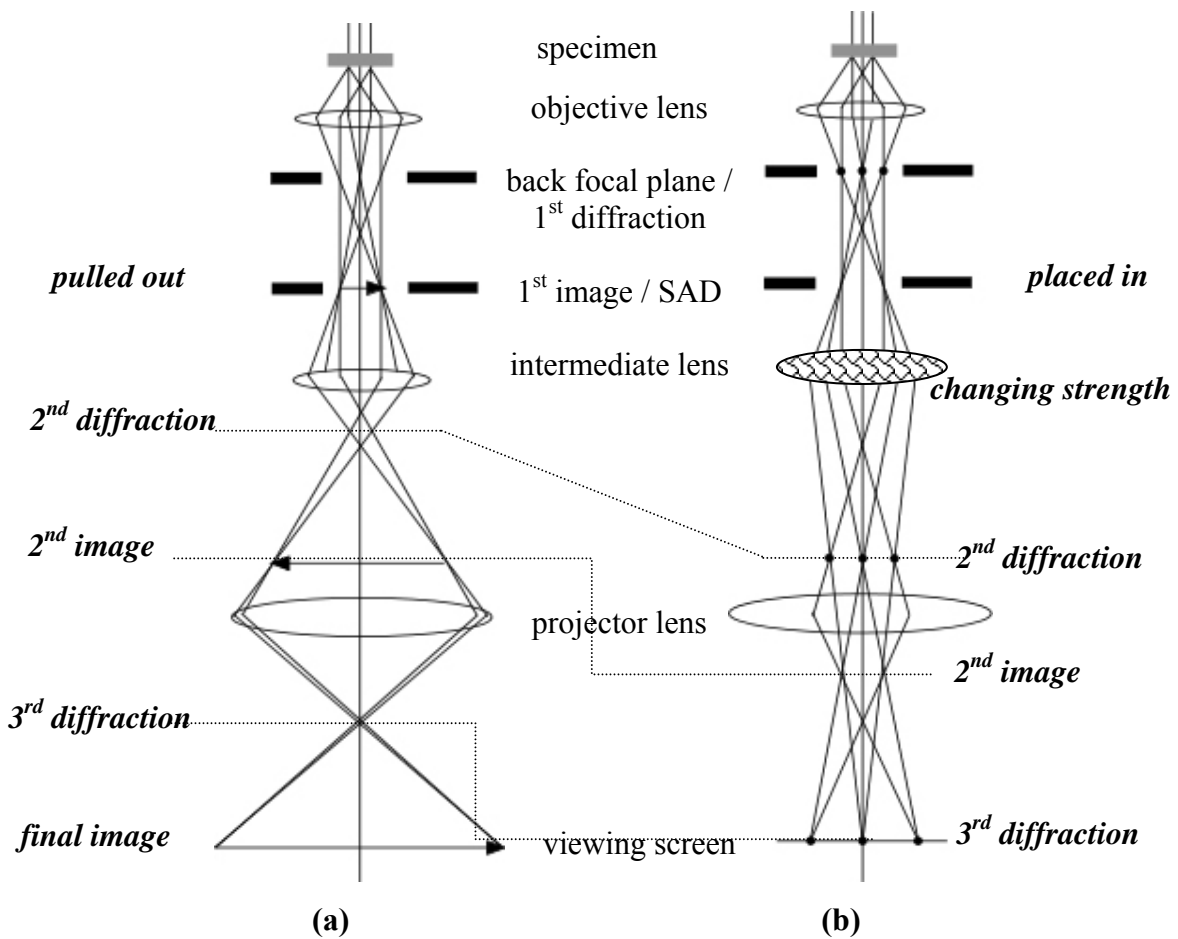


Fig.4.4 Ray diagram of the two modes in TEM after Reimer^[Reimer]. (a) is the imaging mode, in which the objective aperture can be used to select only the direct beam (bright field) or diffracted beams (dark field) for the image formation on the viewing screen. In the diffraction mode (b), the intermediate lens excitation is changed and the diffraction pattern is imaged on the viewing screen.

The contrast of an image formed by conventional TEM is mainly due to the changing amplitudes of the electron waves which travel through the specimen. Amplitude contrast has two types, mass-thickness contrast and diffraction contrast. Both of them depend on how electrons are scattered in the specimen. Generally, the thicker and stronger scattering (from heavier elements)

regions have lower intensity in the BF image than the thinner and weaker scattering areas. For crystalline materials, the OR also affects the contrast of the images (diffraction contrast). Maximum contrast will occur when the Bragg condition is satisfied and the objective aperture is inserted. When the incident angle equals to θ_{Bragg} , the incident beam will be diffracted at the corresponding atomic planes, and the corresponding region will appear dark in the bright field image.

Diffraction occurs when the Bragg condition is fulfilled. For a given material in the TEM, the diffracted beams occur in certain directions (θ), which depend on the crystal structure (symmetry and d-spacing) of the specimen. Thus, the diffraction patterns (DP) and the spot intensities will be various for different materials, and can be used to reveal the crystal structures of materials, as well as to determine the OR between films and substrate.

Micro-diffraction and nano-diffraction also belongs to the diffraction mode. The difference is that, in SAD mode, the incident beam is parallel, while it is a convergent beam in micro- and nano-diffraction experiments. The convergent beam is produced by focusing the beam with a small condenser aperture. Micro- and nano-diffraction can be obtained from very small areas, $\sim 15\text{nm}$ diameter in the JEM-2000FX. The disadvantage of this technique is that the focused beam will strongly heat the observed area of the sample, and that the sample will be contaminated.

B. High resolution TEM

High resolution TEM is a powerful tool to reveal the structure of materials at an atomic level, which cannot be revealed by bright field or dark field techniques^{[Williams], [Fultz]}.

BF (or DF) is using only forward-scattered (or diffracted) electron waves, while a HRTEM image is an interference pattern between the forward-scattered and diffracted electron waves from the specimen. Therefore, in HRTEM images, many beams are contributing to each spot in the final image. On the other hand, the imperfect lenses smear each spot into a disk, and overlapping between the nearby disks occurs. These characteristics prevent that the HRTEM images can be interpreted intuitively, and thus simulation is required as an assistant technique to understand the real atomic structure of the samples.

In the following, the imaging process and optimised imaging conditions of HRTEM will be described. As to the simulation, it will be described in the following part.

Imaging formation and properties

Since each point in the specimen may be different, a function is used to describe the specimen, $f(r)$. The incident wave ψ_o will be modified by both the specimen function, $f(r)$, due to scattering when it penetrates the specimen, and by $h(r)$, the transmission function of the lenses after it passed the specimen. The wave function in the final screen plane is $\psi(r)$ [Williams],

$$\psi(r) = \psi_o(r) f(r) \otimes h(r) \quad (4.6)$$

or
$$\psi(u) = \psi_o(u) F(u) H(u) \quad (4.6'),$$

where ψ_o is the incident wave; u is the corresponding vector of r in reciprocal space. $F(u)$ and $H(u)$ are the Fourier transforms for $f(r)$ and $h(r)$, respectively. Fig.4.5 is the schematic drawing for the image formation in HRTEM.

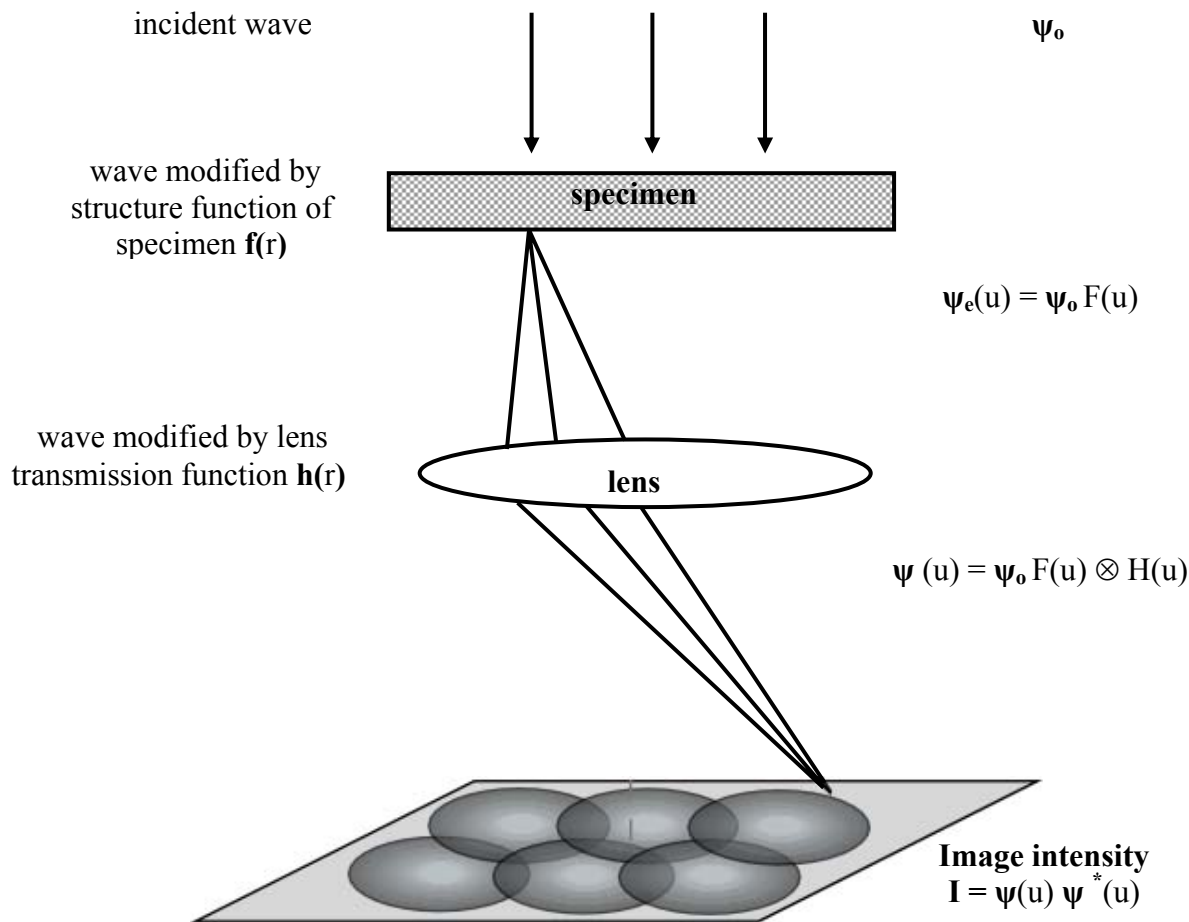


Fig. 4.5. Schematic drawing for the image formation in HRTEM [after Kienzle].

In Fig. 4.5, the incident wave ψ_0 will be modified into $\psi(u)$ by both sample structure and lens aberration when the electron wave penetrates them. The image intensity is $\psi(u)\psi^*(u)$, revealing the structure information adjusted by the transmission function.

A general model describes the specimen function $f(r)$ as

$$f(x,y) = A(x,y) \exp[-i\phi_t(x,y)] \quad (4.7)$$

Here $A(x,y)$ is the amplitude and ϕ is the phase depending on the thickness t of the specimen. To simplify the model, $A(x,y)$ is set to unity. Phase changes only depend on the potential $V(x,y)$ which the electrons pass in the specimen. Assumed that the sample is thin and the potential projected in z direction is $V_t(x,y)$, the specimen function can be given as:

$$f(x,y) = \exp[-i\sigma V_t(x,y) - \mu(x,y)] \quad (4.7')$$

where σ is a constant for elastic interaction. If the absorption $\mu(x,y)$ can be neglected, the specimen can be treated as a phase object. This is known as phase-object approximation (POA).

For very thin specimen, the projected potential $V_t(x,y)$ is very small. Then the exponential function can be expanded and, if absorption and higher-order terms are neglected, $f(x,y)$ becomes:

$$f(x,y) = 1 - i\sigma V_t(x,y) \quad (4.7'')$$

In this case, the amplitude of the exit wave depends linearly on the thickness of the sample. This further simplified model is known as weak-phase-object approximation (WPOA).

The transmission function $h(r)$ describes how the information of the specimen in real space is transferred into an image or how the spots smear into disks, correspondingly, $H(u)$ transfers the same information in reciprocal space. $H(u)$ is named as contrast transfer function (CTF). $H(u)$ is described as the multiply of the aperture function $A(u)$, envelope function $E(u)$ and aberration function $B(u)$:

$$H(u) = A(u) * E(u) * B(u) \quad (4.8).$$

B(u) equals to $\exp(i\chi(u))$, and χ is expressed as

$$\chi = \pi \Delta f \lambda u^2 + 1/2 \pi C_s \lambda^3 u^4 \quad (4.9)$$

where, Δf is the defocus, C_s is the spherical aberration coefficient and λ is the wavelength of the electrons.

Using the WPOA model and setting $h(x,y)$ as $\cos(x,y) + i\sin(x,y)$, then according to Eq.(4.6') and Eq(4.8), the intensity of the image is given by

$$I = \psi\psi^* = 1 + 2\sigma V_t(x,y) \otimes \sin(x,y) \quad (4.10)$$

Here ψ_0 has been normalized to one and the terms in σ^2 have been neglected.

Since only the imaginary part of B(u) is contributing to the image intensity, B(u) can be set as $2\sin\chi(u)$. A transfer function, T(u) is defined in Eq. (4.11), being distinguished from H(u)

$$T(u) = A(u) E(u) 2\sin\chi(u) \quad (4.11).$$

Here A(u) is the aperture function, and E(u) is the envelope function. $\chi(u)$ is named as phase-distortion function, given by Eq. 4.9.

In the curves of T(u) versus u, when T(u) crosses the u-axis, the sign of T(u) will reverse. Then the intensity of the image will be opposite, in another words, the contrast will change. It should be pointed out that, it is T(u) rather than H(u) called as CTF in many HRTEM books.

Δu is set as the distance between the first two of u, which make T(u) equal to zero. The larger Δu , the slower the change in contrast, i.e. the more different values of u give the same contrast. For this values, it is easier to interpret the image. As a limit for a straightforward interpretation for the HRTEM image, Δu is an important value in reciprocal space. Corresponding to this, in real space, two points can be resolved when their distance is larger than Δr ('point-resolution').

Scherzer defocus

Scherzer defocus is defined as the defocus in which the bandpass (Δu) of the CTF reaches the largest value. Setting the differentiated term of Eq. (4.8) to zero, and inserting Eq. (4.9) in the result, the corresponding u_{Sch} and Δf_{Sch} are

$$u_{\text{Sch}} = 1.51 C_s^{-1/4} \lambda^{-3/4} \quad (4.12)$$

and

$$\Delta f_{\text{Sch}} = -1.2 (C_s \lambda)^{1/2} \quad (4.13)$$

Eq.(4.12) and (4.13) reveal that for a certain TEM, the best contrast condition (largest Δu) and defocus can be balanced by both the wavelength and the spherical aberration of the objective lens.

It also gives a hint to experiments that, when d-spacings of the observed material are located in the region of $(0, u_{\text{Sch}})$, and adjusting the TEM parameters to the optimised values (Δf_{Sch} , astigmatism, tilt) then the HRTEM image could be directly interpreted.

C. Simulation and quantification of HRTEM

As mentioned in the previous paragraph, the HRTEM image usually cannot be explained intuitively, thus special techniques are required to recover the structure. Simulation is one of the solutions. Structure models can be evaluated precisely by comparing the simulated images for different models to the experimental image. In this way, the most likely real structure at the atomic level can be obtained. Several modifications and repeated processes are required before the results are obtained.

The steps for simulation and quantification can be summarized as follows and a schematically diagram is given in Fig.4.6:

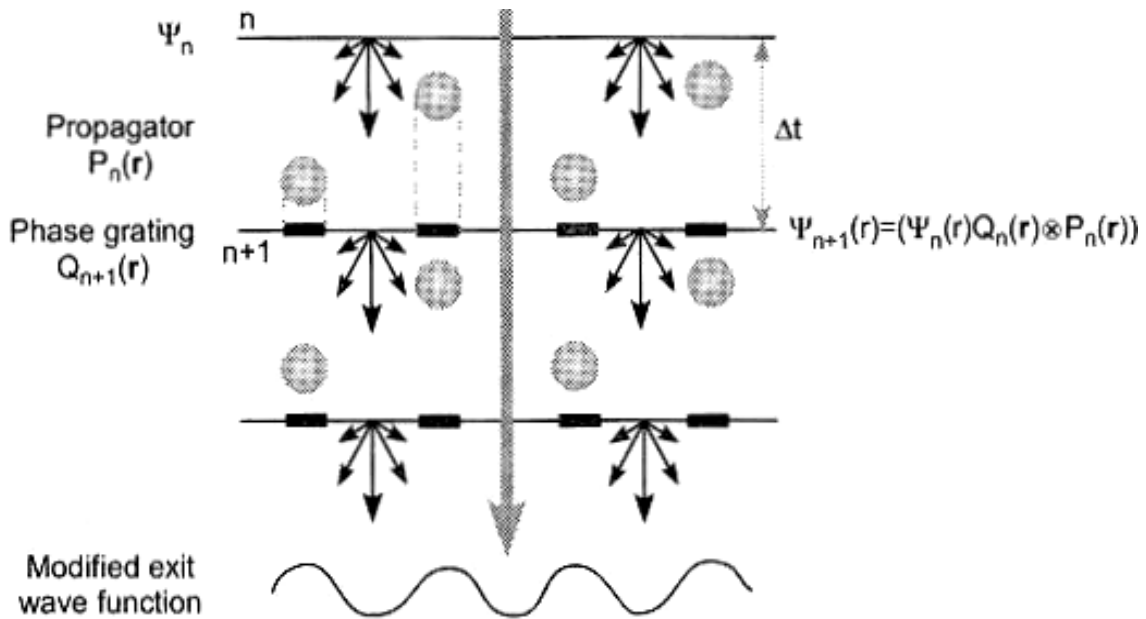
1. a crystal structure model is constructed,
2. the exit wave penetrated through the sample is calculated,
3. the final exit wave is then modified by the interaction with the lenses and the image intensity is calculated,
4. the simulated image and the experimental image are quantitatively compared.

The first step can be done by computer programmes in which all space groups have been listed. In this work, the software package named “Ideal-atomic” was used. The models can be built by choosing the suitable structure, filling in the atomic species, and defining the lattice parameters.

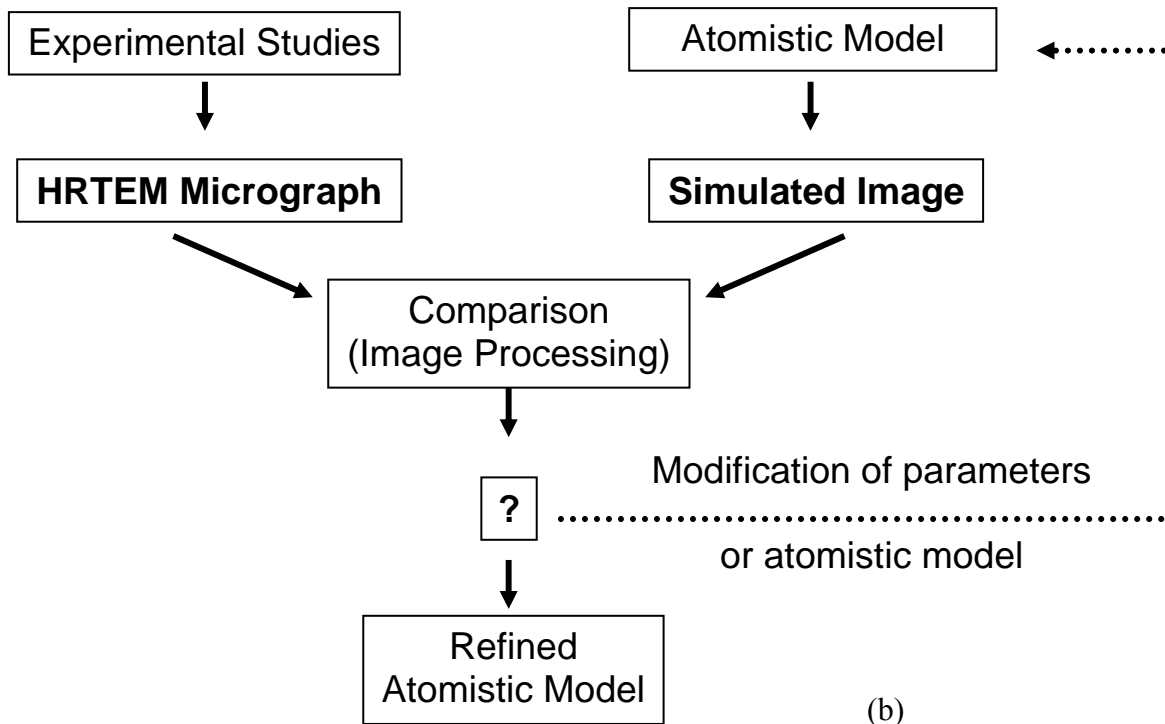
The second step can be done using two methods, one is the Bloch wave method^[Metherell], and the other is the multislice method^[Cowly-Moodie]. However, a wave propagated through the structure with defects such as interfaces can only be calculated by the multislice method, therefore, this method will be discussed in detail. In this method, the specimen is sectioned into many slices, and then each slice is projected onto a plane in the slice. Usually, it is the top, bottom or middle plane of the slice. The crystal potential is projected for the slice according to the atomic structure, called grating, $Q(r)$. The amplitudes and phases for the exit wave $\psi_{n+1}(r)$ are calculated as follows: the interaction of the wave with the projected potential leads to the modified wave $\psi_n(r)$. This wave is propagating through free space and will be modified to $[\psi_n(r) Q_n(r) \otimes P(r)]$, here $P(r)$ is the propagator of the electron waves in free space. This process is repeated until the exit wave from the last slice has been calculated. Using fast Fourier transformation (FFT), the calculated result can be transferred between real space and reciprocal space.

The third step is to calculate the image intensity and to adjust the calculated image intensity by the instrumental parameters, e.g. defocus, misaligned tilt angle, lens aberration. In the present work, the software package Electron Microscopy Simulation (EMS)^[Stadelmann] is applied to perform the second and third steps. The last step, comparing the simulated to the experimental image, applies a package named IDIM (Iterative Digital Image Matching^[Möbus]). A diagram of the program is given in Fig. 4.6 (b). Before the comparison to the simulated one, the experimental image has to be digitalized by a charge-coupled device (CCD) camera. The region of interest is cut out in the same size ratio as that of the simulated image. Then the cut experimental image is scaled and compared to the simulated one. The result of the comparison can be improved by adjusting both the atomic model and imaging parameters. Repeating this procedure (the dot-line-circle in Fig.4.6 (b)), the agreement between the simulated and experimental images can be enhanced. In IDIM, the agreement between simulated and experimental images is presented by a cross-correlation factor (XCF):

$$XCF(A, B) = \frac{\Sigma(A_{ij} - \bar{A})(B_{ij} - \bar{B})}{\sqrt{\Sigma(A_{ij} - \bar{A})^2 (B_{ij} - \bar{B})^2}} \quad (4.14)$$



(a)



(b)

Fig.4.6 (a) schematic illustration of the electron wave propagation^[after Tchenychova], used for the multislice calculation method. (b) the diagram for quantitative HRTEM.

where A_{ij} is the value of intensity for the pixel which locates at (i, j) in the experimental image, and B_{ij} is that for the simulate image. \bar{A} and \bar{B} are the average values of intensity in the experimental and simulated images, respectively. For perfect agreement, the XCF should reach 100%. However, in reality it is lower, because the noise in the background of the experimental image cannot be removed.

In this work, quantitative HRTEM was used to determine the crystal structure of the new phase, by evaluating different structure models.

D. Analytical TEM

In the present work, a VG HB501UX STEM was used to perform both X-ray energy-dispersive spectroscopy and electron energy-loss spectroscopy. The chemical composition of the new phase was determined by the quantification of the EDS data. The VG HB501UX dedicated STEM has a cold field emission source and is equipped with a Noran EDS detector and a Gatan UHV Enfina system. The EDS system is inserted in front of the sample (see Fig. 4.7). The EELS spectrometer has a magnetic prism, which focuses the electrons with different energies at different points in a plane where a CCD camera is placed. A schematic drawing of the microscope is given in Fig.4.7.

Basics of EDS and EELS

When electron beams pass through the specimen, both elastic and inelastic scattering can occur. These scatterings processes can be accompanied by secondary effects, which are mainly the production of electrons or electromagnetic radiation. The signals from the emitted X-rays are collected by EDS, while EELS reveals the information of the transmitted electrons, as Fig.4.8 illustrates.

X-ray emission is one secondary effect which can occur due to inelastic scattering. When an outer electron falls into an inner shell hole, a characteristic X-ray photon can be released. The energy of the photon is determined by the difference between the energies of the two states involved. Because different atoms have different atomic energy levels, the emitted X-rays from various atoms will have different energy (or wavelength). In other words, the energies of emitted X-rays is a characteristic value for the corresponding element.

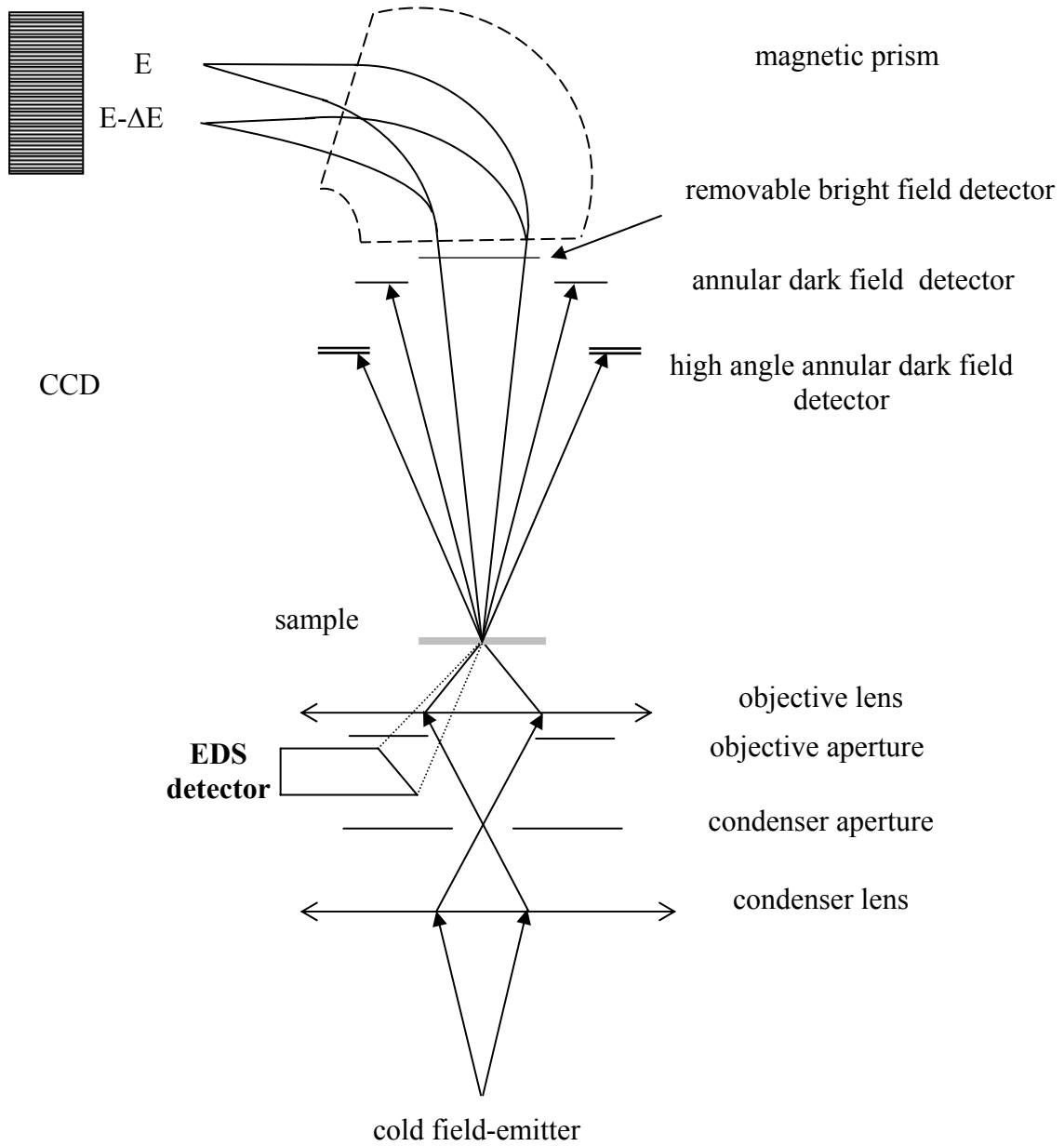


Fig.4.7 Schematic drawing of the analytical TEM VG HB501 UX, which is used to obtain the EDS and EELS data in this work.

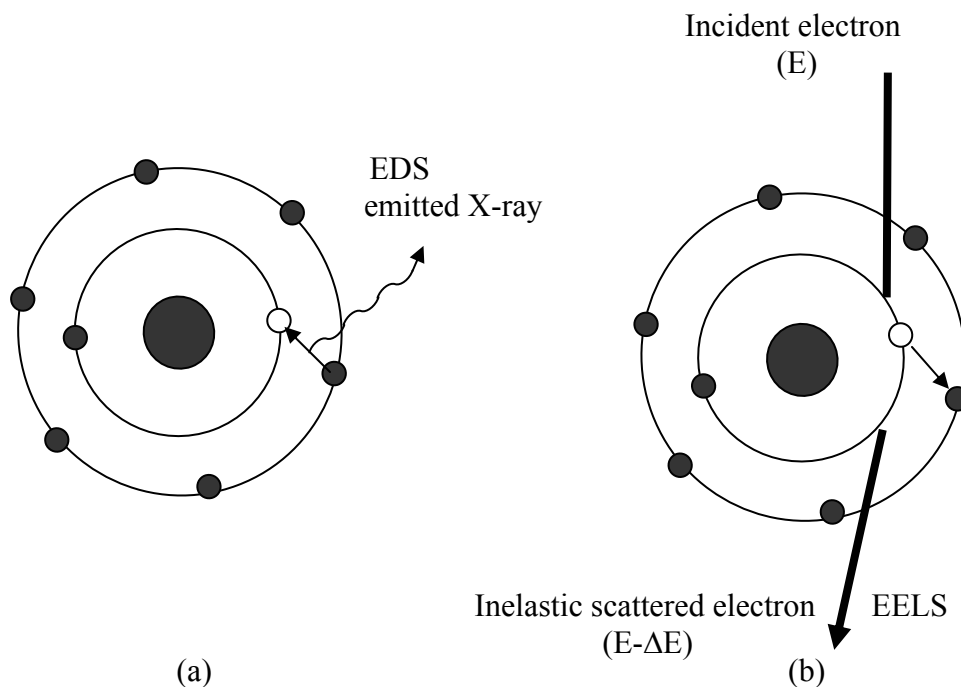


Fig.4.8 (a) In EDS, the transition of an outer electron into an inner hole can release an X-ray photon with a certain amount of energy, which is related to the energy difference between the two involved states. (b) In EELS, the energy difference (ΔE) between the incident and transmitted electron is due to the inelastic scattering within the specimen and the intensity of the transmitted beams versus the energy-loss is measured.

An EDS detector collects series of signals of the emitted X-rays and then the intensity versus the X-ray energy is plotted. EDS can reveal the chemical information from the specimen as described above.

Due to the inelastic interaction between the primary electrons and the specimen, a energy loss ΔE between the scattered and the incident beam occurs. This inelastic interaction can induce for example an excitation of an electron from an occupied state to an unoccupied state. When the excitation occurs between a core-shell and the conduction band or within the conduction band, the excitation is called interband or intraband transition, respectively. The elementspecific ionization edges (core-losses) are associated with an electron energy loss near-edge structure (ELNES) and an

extended energy loss fine structure (EXELFS), which occur up to ~ 50 eV and above 50 eV respectively, from the edge onset. The transitions are shown schematically in Fig. 4.9. Compared to EDS, EELS can reveal the bond state of the investigated material, besides to detect the chemical composition.

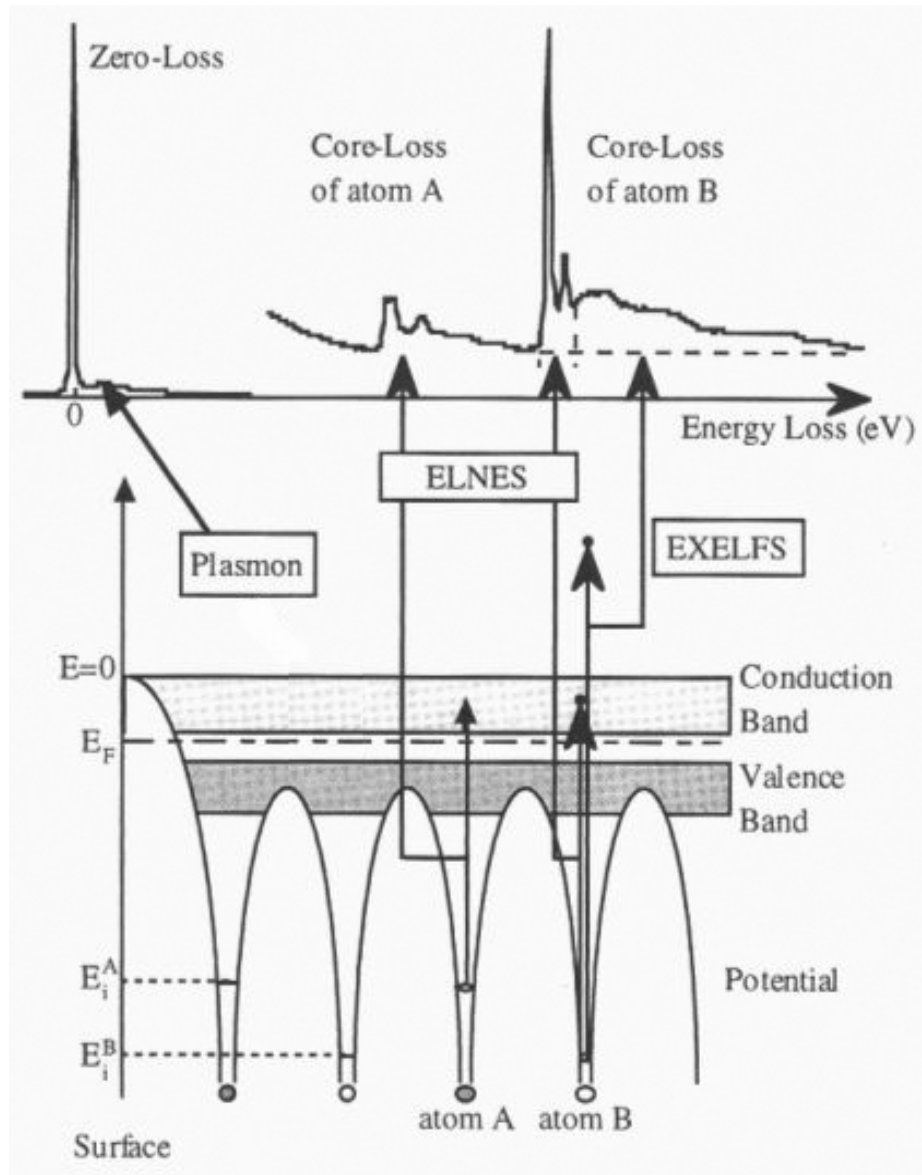


Fig. 4.9 An EELS spectrum and the corresponding energy levels. ELNES is the energy-loss near edge structure and EXELFS is the extended energy-loss fine structure (taken from Kurata^[Kurata]).

Quantification analysis

In both EDS and EELS, the concentration of certain elements can be determined from the quantitative analysis of the data. For a binary system with elements A and B, if the foil is very thin, absorption and fluorescence of X-rays within the specimen can be neglected. Then the concentration ratio between different elements can be related to the ratio of measured intensities, by the so-called Cliff-Lorimer equation ^[williams]:

$$\frac{C_A}{C_B} = k_{AB} \cdot \frac{I_A}{I_B} \quad (4.15).$$

Here I is the measured intensity, C is the chemical concentration, k is the Cliff-Lorimer factor, which is also named as sensitivity factor. For quantitative EELS analysis, a similar equation is valid ^[williams]:

$$\frac{C_A}{C_B} = \frac{\sigma_B}{\sigma_A} \cdot \frac{I_A}{I_B} \quad (4.16).$$

Here σ_A and σ_B are the cross- sections for the transitions involved.

For different chemical systems, k factors are different. Even for a certain system, the k factor is not a constant. It is sensitive to the detector, microscope setup, microanalysis conditions, thickness and peak-integration methods. Thus, k factors can only be used for different analysis when they are obtained under similar conditions. There are two ways to determine the k factor: one is obtaining it from experiments using standards, the other is to calculate it.

Experimental determination of the k factor requires a sample with known composition (C_A and C_B) as a standard. EDS experiments are performed on the standard to get I_A and I_B . Then the k factor can be determined by inserting the four values into Eq.(4.15).

Combining the experimental determined k_{AB} , with the intensities from EDS experiments, the concentration ratio in the investigated samples can be obtained by Eq.(4.15). In the present work, bulk CuAl_2 samples acted as a standard to obtain the k_{CuAl} for the Cu-Al system, and the chemical composition of the interlayer between Cu and Al films was determined using this experimental k factor.

4.2 Sample preparations

In this part, the Cu/Al layer deposition, the preparation of TEM samples and the fabrication and identification of a standard sample for the Cu-Al system will be presented.

4.2.1 Film deposition

To deposit layered Cu/Al on ceramic substrates (Si and α -Al₂O₃), two methods have been employed, i.e. sputtering and molecular beam epitaxy (MBE).

A. Sputtering

Multilayer Cu/Al films were deposited on Si substrates by sputtering. The first deposited layer was Al, and then Cu was deposited on top of it. The total thickness of the layers was always kept constant to 800nm with an additional 5nm Al cap layer. The individual layer thicknesses are 100, 200 and 400nm, leading to multilayer systems with 8, 4 and 2 layers. Before deposition, the wafers are heated up to 850°C. For all films the first 50 nm Al were deposited at 150°C. After that the sputter chamber was cooled down to room temperature and then the deposition was continued. The parameters during deposition were as follows: base pressure $< 4 \times 10^{-10}$ mbar; sputter power of 100W; argon flow of 30cm³/min; deposition rate of 7.30 nm/min for Al and 8.97 nm/min for Cu.

B. MBE deposition

Two kinds of bilayer film samples consisting of 400 nm Cu / 400 nm Al on sapphire (0001) and 100 nm Cu / 100 nm Al on sapphire (0001) were prepared by MBE. Before deposition, an Argon beam with an energy of 200 eV was used to clean the surface of the Al₂O₃ substrate from contaminants. Then the substrate was heated at $\sim 1000^\circ\text{C}$ for 3 hours to remove the surface defects stemming from the cleaning procedure. The pressure of the deposition chamber was kept around 10^{-9} mbar. The film consisting of 100 nm Cu / 100 nm Al was deposited at RT, while the 400 nm Cu / 400 nm Al bilayer film was grown at Al₂O₃ at 200°C. The deposition rates for both metal films were ~ 0.1 nm per second.

4.2.2 TEM sample preparation

A TEM specimen with high quality should have an optimum specimen thickness and an undistorted crystal structure i.e. minimum amorphous region. To prepare a cross-section TEM specimen of a film sample, several preparation methods can be employed, i.e. TEM specimen with a ceramic holder (polycrystalline Al_2O_3 tube), silicon dummy and titanium clamp holder. The main differences between them are the materials of the holders and the ways the sample is embedded.

Generally, the process of the preparation of a cross-section TEM sample is the following: the film sample is cut into small strips, and these are embedded into the holders (this step will be described further below). After that, the tubes or dummies with inserted sample stripes will be cut into thin disks. The disk will be grinded to $\sim 100 \mu\text{m}$, and then dimpled until the thinnest part of the disk is $\sim 25 \mu\text{m}$. As a final step, the dimpled disk will be ion-milled until the edge is electron transparent. Liquid nitrogen can be applied for cooling samples during the ion-milling procedure. A schematic drawing of the process is given in Fig. 4.10.

The details for the different embedding methods are:

(1) For ceramic holders:

cut the film specimen into stripes with 2 mm width; choose an Al_2O_3 tube, in which the inner tube has a slit with suitable width compared to the thickness of the strip; insert one (or one sandwich couple, i.e. two pieces set face to face) strips into the slit of the inner Al_2O_3 tube and then put the inner tube into the outer Al_2O_3 tube; use well mixed glue (M-Bond 610 and M-Bond AE15 with the ratio of 1:10) to fill the gap; dry and harden the glue in an oven or in air.

(2) for Si-dummy holders:

cut film into stripes with 2.5 mm width; choose two Si-dummies with suitable size, and then glue one piece of them on the wafer and the other on the film (for sandwich samples, glue two films face to face and then glue dummies to the two wafers, separately); if it is necessary, grind the dummies to keep the total size (the dummies and strip(es)) to around 2.5 ~ 3 mm.

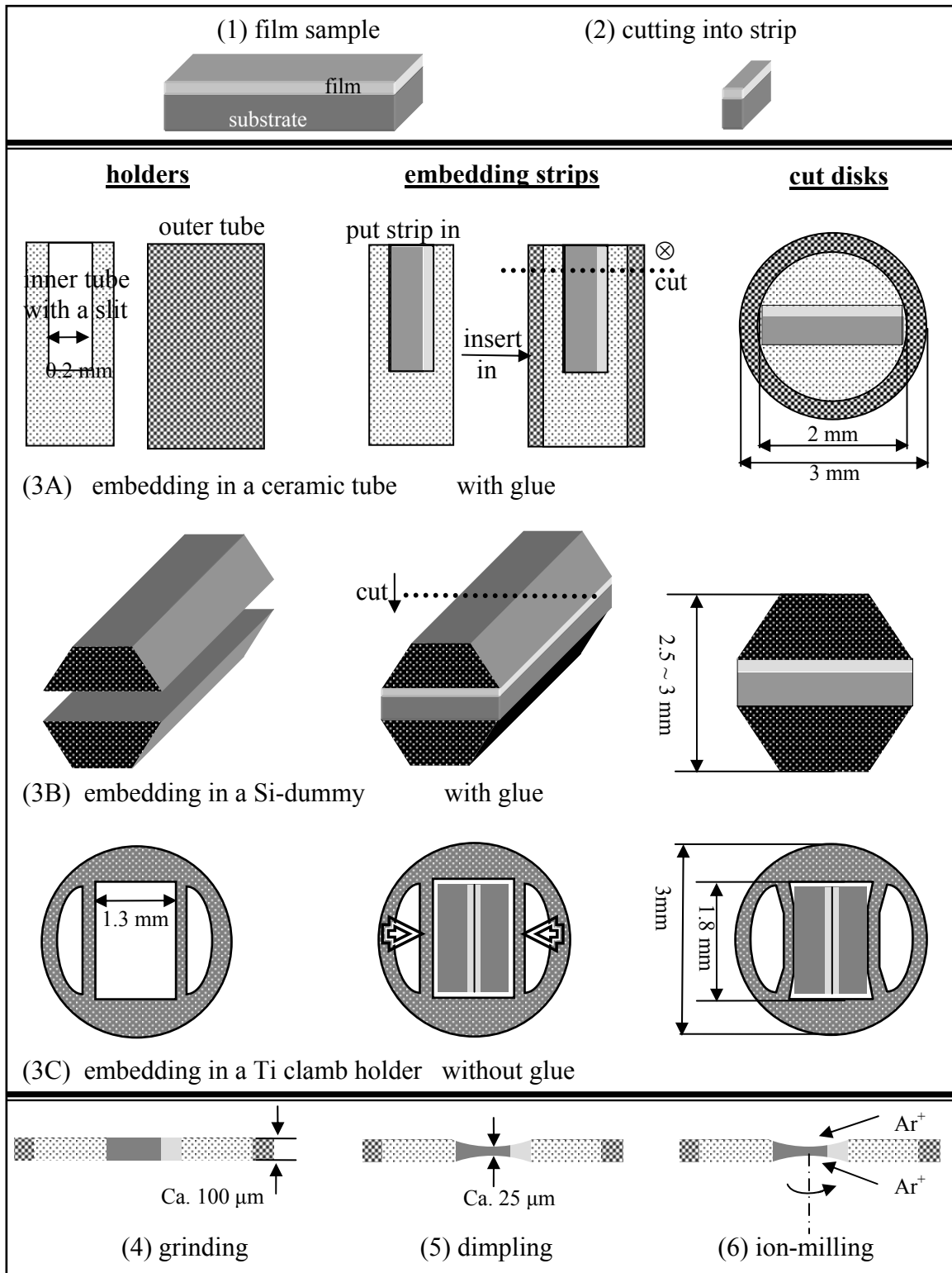


Fig.4.10 Cross-sectional TEM specimen preparation with different embedding ways.

(3) for Ti-holders:

the cut stripes are inserted into the Ti-holder face-to-face; if it is necessary, grind the stripes to fit to the hole (1.3 mm × 1.8 mm) of the holder, push the Ti arms in the holder that they deform to fix the stripes.

Compared to the first two methods (holders with Al₂O₃ tubes and Si dummies), Ti-holders have an advantage that they do not require any glue. Since the glue can melt at higher temperatures, the third method is usually used to prepare samples for *in situ* TEM heating experiments. As to the first two methods, silicon dummies are especially used for films grown on Si substrates, while the Al₂O₃ tube is taken for films grown on sapphire (single crystalline Al₂O₃). The reason for this is that the TEM sample will be easier to be prepared if the substrate and the holders have similar properties during grinding and ion-milling.

4.2.3 Fabrication, identification and *k*-factor of the standard sample for the Cu-Al system

According to the Cu-Al binary phase diagram (Fig.2.6), if the alloy is cooled down from the liquid state to RT, 6 intermetallic phases can form. From these intermetallic phases, CuAl₂ has the lowest melting point, it is directly formed from the liquid and does not transform to other phases during further cooling. Thus CuAl₂ was chosen as a standard sample for the Cu-Al system investigated in this work. Here, the fabrication and identification of a standard single phase CuAl₂ sample will be described first, then the determination for the *k*-factor will be discussed.

(a) Fabrication

A CuAl₂ alloy was fabricated by conventional powder metallurgy methods. The chemical formula of CuAl₂, which is related to atomic percent, can also be expressed as Cu_{53.62}Al_{46.38} in weight percent.

A Cu rod and an Al plate with the purity of 99.999 wt% were used to produce the standard sample. They were cut into small pieces and washed by liquid HNO₃ (for Cu) and HCl (for Al). The acids were used to remove the oxides on the metal surfaces. Then the cleaned Cu and Al pieces were

weighed by an electronic balance. For the production of 25g CuAl₂, 13.4189g Cu and 11.6077g Al were needed. To reach the weights precisely, metal powders with the same or higher purity grade are used in addition. After that, the whole Cu and Al were mixed together and pulled into a ceramic crucible. This crucible was transferred into a furnace and heated to ~ 600 °C in high vacuum. Then the metal was cast into a Cu tube with an inner-diameter of 2cm. After the temperature of the Cu tube reached RT, the oven was opened and the cast alloy was removed from the Cu tube.

In general, the composition might deviate from the ideal composition of CuAl₂ due to mass loss and unavoidable experimental errors. Therefore some precautions were performed before and during the casting experiment. (1) Since Al has a much lower melting point (660°C) than Cu (1085°C), Al can be easier lost during thermal treatment. Therefore, in the experiment some additional Al was used to compensate this loss, in order to maintain the ideal composition. (2) The casting temperature is chosen to 600 °C, which is slightly higher than the melting point of CuAl₂ (590 °C). When the original composition is close to the stoichiometric composition of CuAl₂, this casting temperature could decrease the possibility of forming other equilibrium intermetallic phases. (3) A high cooling rate after casting should be chosen to avoid forming other phases (CuAl, especially when the initial composition is not exactly stoichiometric at CuAl₂). Quenching would be preferred, but the grain size would be smaller and thus more grain boundaries would occur in the sample. Such characteristics are not favored for a reference sample in EDS experiments. Therefore, the Cu tube was rapidly taken out from the furnace as soon as casting finished but it was not quenched. (4) The usage of a Cu tube is not the best solution, since it might react with the initial melt leading to a change in the chemical composition, especially at the surface of the cast. However, only two kinds of metal containers (Al or Cu) were available in the laboratory and from these the Cu with its higher melting point was taken.

(b) Identification

Though the original composition of the fabricated alloy has been set as CuAl₂ before casting, and some precautions have been performed trying to keep the composition of the cast, an identification of the standard sample had to be carried out. The motivation for this was that the standard sample will strongly influence the interpretation of the experimental results.

❖ Phase and structure

Light microscopy was used to investigate the grain size of the cast. The images taken with polarized light (Fig. 4.11(a)) showed some lamellas formed at the center of the casting, with a width from $80\mu\text{m}$ to 0.5mm . The image taken with white light (Fig. 4.11(b)) is near the surface area, which has smaller grain size compared to the center of the casting.

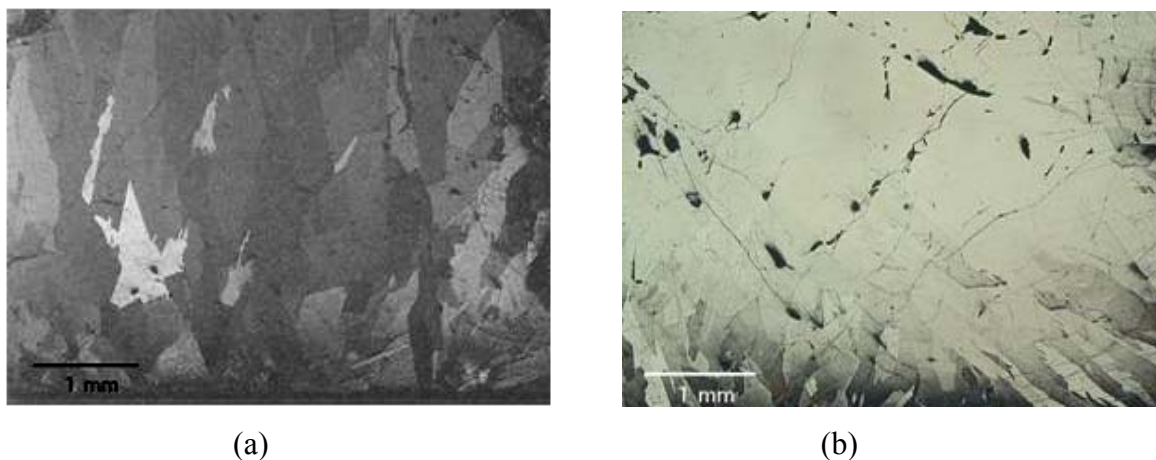


Fig.4.11 Light microscopy images of the cast material taken with polarized (a) and white (b) light.

X-ray θ - 2θ diffraction experiments were performed on the cast sample to determine the occurring phase(s). Fig. 4.12 shows the θ - 2θ plot, which was acquired from the middle part of the cast. All of the peaks in this plot were identified to belong to CuAl_2 with a tetragonal structure. This proved that the casting within the detection limits is a single CuAl_2 phase. The fact that various sets of planes were present suggested that the sample is polycrystalline.

❖ Chemical composition

The Cu-Al phase diagram (see chapter 2), shows that CuAl_2 has a narrow chemical composition range in which the wt% of Cu is ranging from $53.39 \sim 53.96$ wt % ($32.5 \sim 33.0$ at %). The quantitative chemical analysis requires that the standard sample has exactly this chemical

composition. Therefore, scanning electron microscopy (SEM) and electron probe microanalysis (EPMA) were used to determine the chemical composition of the cast. Both of these methods are using focused electron beams to bombard the specimen surface, and then collect and analyze the X-ray photons. EPMA uses a higher beam current density and thus gives a better signal to noise ratio in the data, compared to standard SEM/ EDS systems. The EPMA is also equipped with a WDS (wavelength dispersive spectroscopy) detector which has a higher sensitivity for light elements. In the present work, EDS spectra are randomly taken from 12 different areas from the cast CuAl_2 sample. The average atomic percent of Cu is 31.4 ± 0.3 at %, with 1- 2% systematical error as determined by EDS in the SEM. With the EPMA, line scan experiments were performed. 400 points have been investigated with a step length of $5.5\mu\text{m}$, within a region as wide as 2.2mm. The result revealed that the average atomic percent of Cu is 33.9 ± 0.2 at % in the cast. For the line scan experiment, the systematical error is 0.2 % and 0.1 % for Cu and Al respectively.

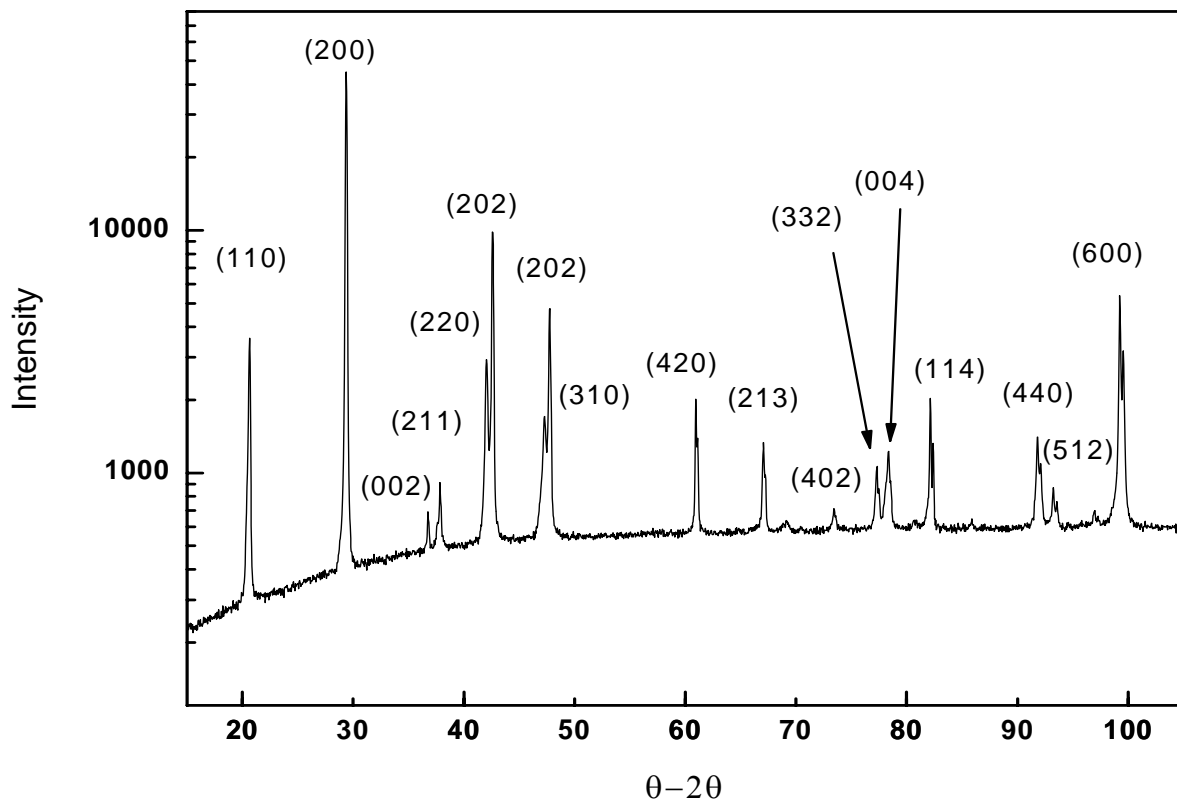


Fig.4.12 XRD profile from the cast sample. All the peaks can be identified and correspond to planes from CuAl_2 .

The values from these two methods are similar but not identical. Because EPMA gives more precisely information and also a larger area was investigated by EPMA, it is more reasonable to take the result from the EPMA as the chemical composition of the standard sample.

❖ k_{CuAl} in the Cu-Al system

The identified cast sample was prepared for TEM investigations and analyzed in the VG HB501 UX. EDS data have been taken at different points in one grain with various thicknesses. The intensities of the peaks from Cu and Al in the EDS data were determined. Inserting the average intensities for each position and the composition obtained from the electron probe microanalysis into Eq.(4.15), the values for the k_{CuAl} factor were obtained. The average k_{CuAl} can be determined to amount to 1.9 ± 0.2 .

Chapter 5

Experimental results and analysis

After film deposition different methods such as XRD, XRR, CTEM, EELS, EDS, HRTEM, quantitative HRTEM and in-situ HRTEM, have been applied to determine the microstructure of the bilayer films. According to the type of substrates employed during film fabrication, this chapter will be divided into two parts, Cu/Al films on Si and sapphire substrates, respectively.

5.1 Cu/Al multilayer films on Si

The Cu/Al multilayer films on Si substrates were produced by magnetron sputtering as described in chapter 4.2.

X-ray diffraction

For the Cu/Al multilayer film systems, XRD methods¹ were employed to characterize the phases, orientation relationships between films and substrates, as well as the texture of the films. The OR was detected from θ -2 θ scans, and the texture structure from pole figures.

θ -2 θ scan XRD profiles were acquired for the multilayer films consisting of 2, 4 and 8 Al and Cu layers, respectively. All the samples show a similar behavior. Fig.5.1 displays as an example the results for the film consisting of 400 nm thick Al and 400 nm thick Cu layers.

Firstly, all the detected peaks were identified and belong either to Cu, Al or Si reflections. No other phases were found in the θ -2 θ scan.

¹ Both θ -2 θ scans and pole figures were performed by Dipl.-Ing. G. Maier, ZWE-Röntgenbeugung

Secondly, the θ - 2θ scans exhibited many peaks which came from various planes with different orientation. As has been introduced in Chapter 4.1, it denotes that, these films have no preferred orientation relationship with the substrate in-plane and thus are polycrystalline. Nevertheless, pole figures were taken to check for a preferred in-plane orientation between the films and the substrate. During measurements, the angle θ belonging to the Cu (111) plane was fixed, while ψ and ϕ were continuously changed. The results are displayed in Fig. 5.2 for the Cu/Al bilayer film. The rings indicate that many different orientated grains exists in the film. Thus it states that in the Cu/Al/Si film system, the multilayer films are polycrystalline. The θ - 2θ profiles and pole figures of 2, 4 and 8 layers show all a similar behavior.

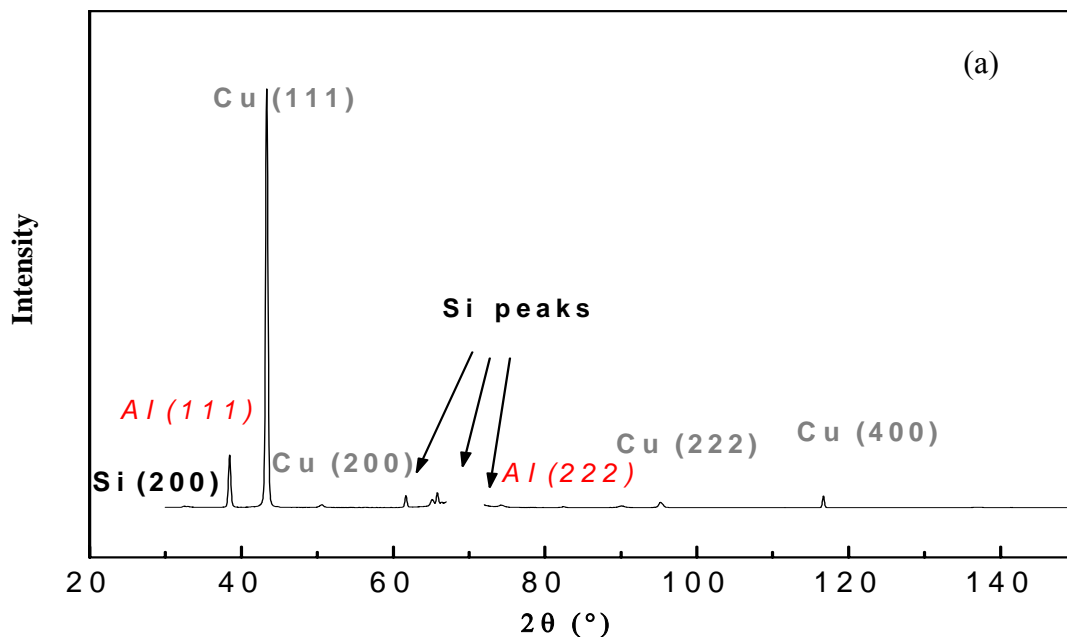
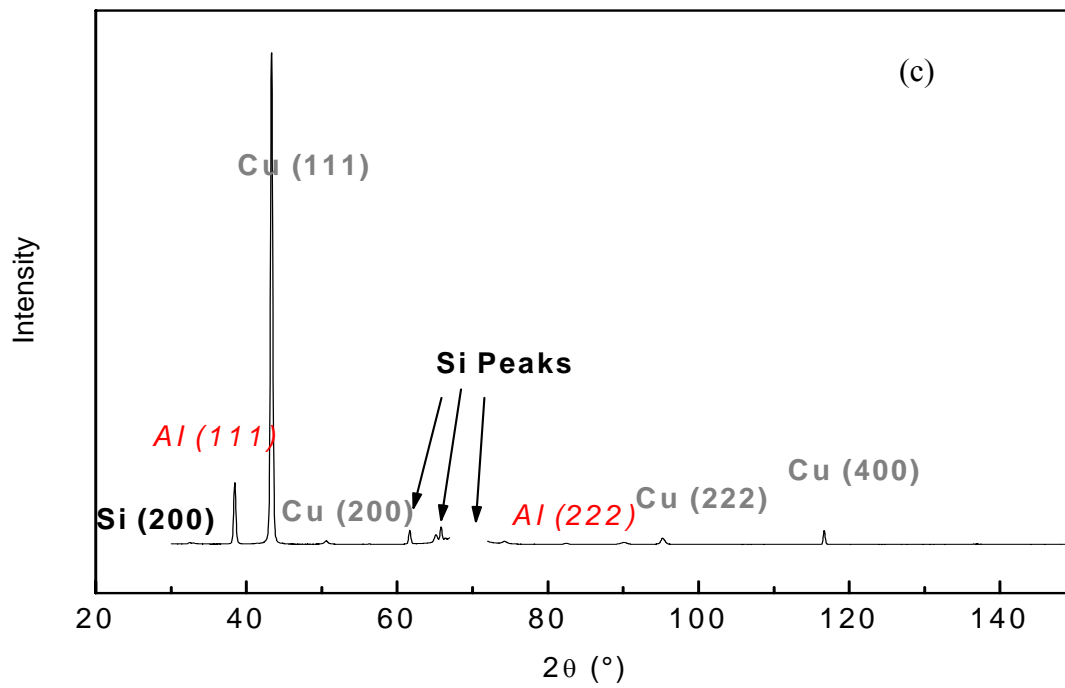
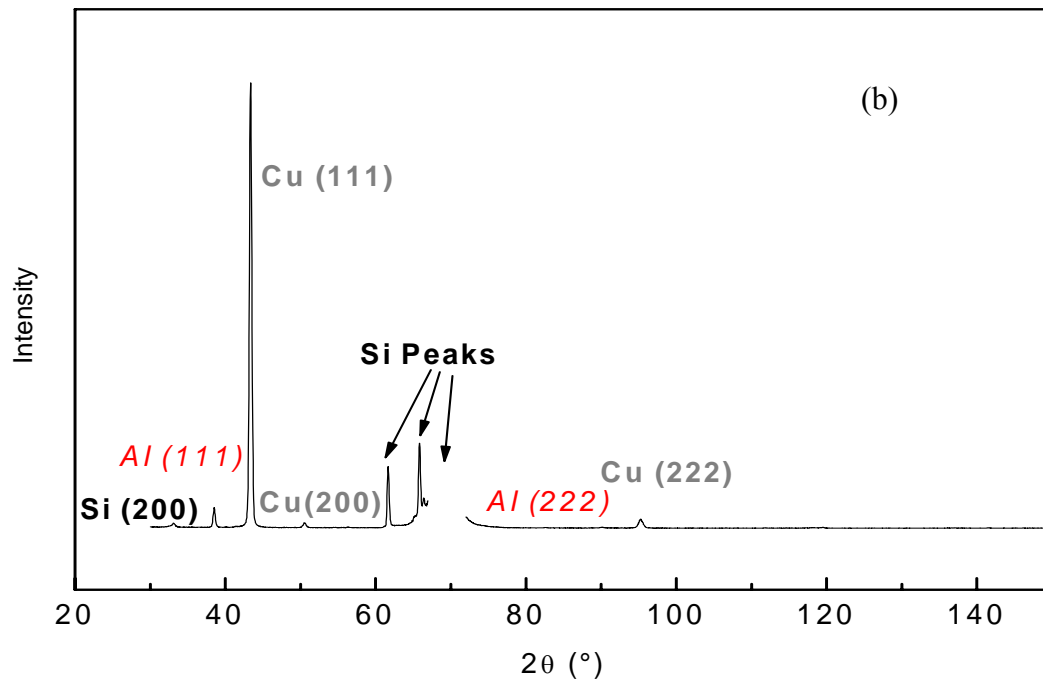


Fig. 5.1 XRD θ - 2θ scans of multilayer Cu/Al films on Si (001). (a), (b) and (c) are the profiles for 2 layers, 4 layers and 8 layers, respectively. They reveal that the Cu/Al films are polycrystalline. (b) and (c) are on the next page. The region at $2\theta \approx 70^\circ$ shows a strong peak from the Si substrate and is hidden for better visibility.



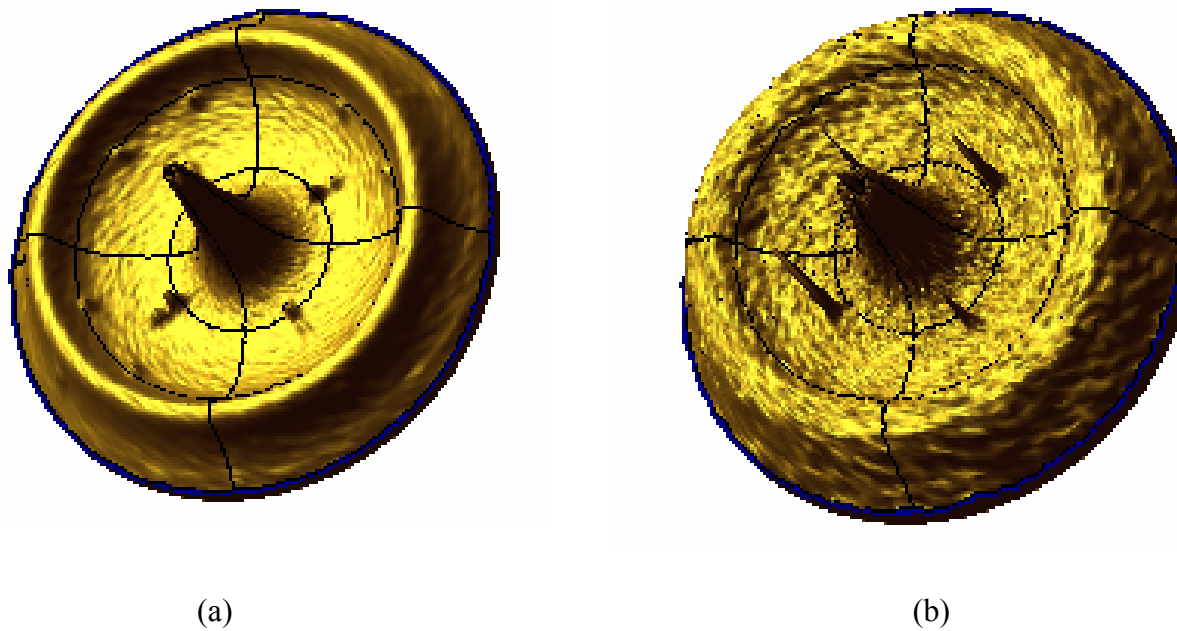
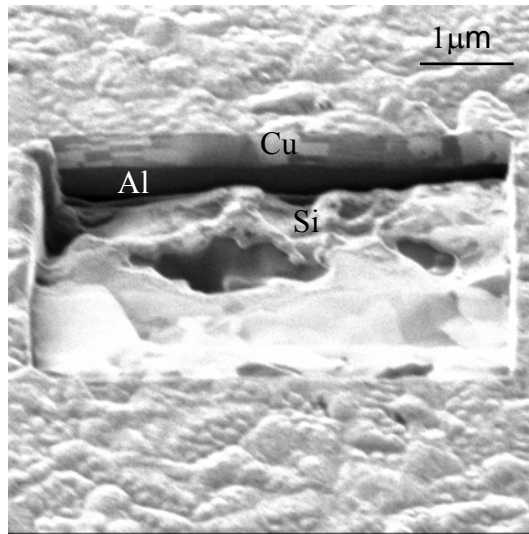


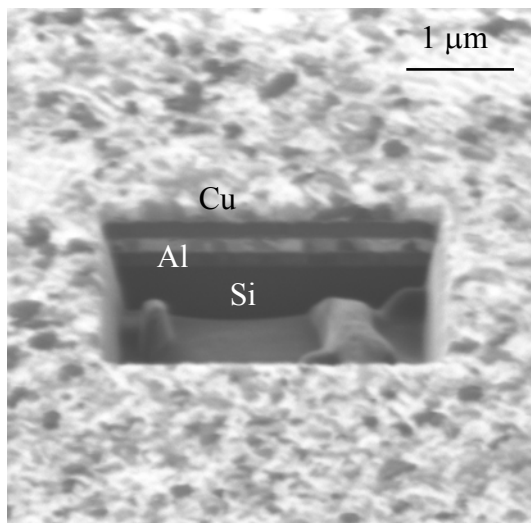
Fig. 5.2 XRD Pole figures for (a) (111) Cu plane and (b) (111) Al plane of the 2 x 400nm Cu/Al bilayer. Besides the four-fold symmetrical peaks belonging to the substrate, there are a few rings visible.

Focused ion beam

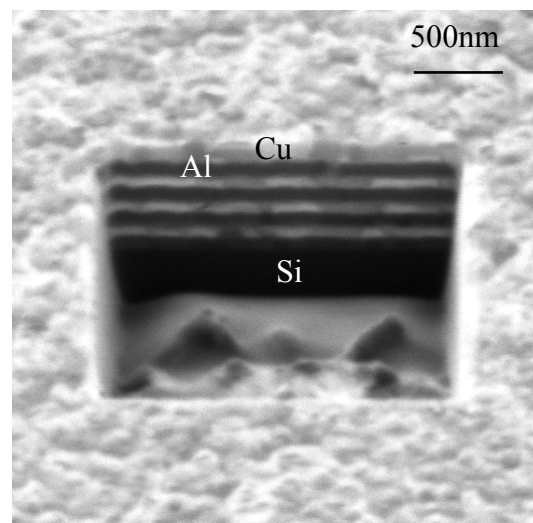
Focused ion beam (FIB) measurements allow a simple and efficient way to investigate the crystal orientation by comparing the contrast of the various grains. To reveal the films microstructure, material was removed by the ion beam from the top layer down to the substrate. As Fig. 5.3 shows, Al is the black appearing layer and Cu is appearing bright. The contrast is not uniform within each layer but changing with position. That demonstrates that the films are not single crystalline and consist of grains with different orientations.



(a)



(b)



(c)

Fig. 5.3 Focused ion beam images of Cu/Al multilayer films on Si with (a) two, (b) four and (c) eight layers with a total thickness of 800 nm. The films are polycrystalline and the grain size is decreasing with increasing number of layers.

Transmission Electron Microscopy

TEM was employed to determine the grain size of the multilayer films and the bright field TEM images are displayed in Fig. 5.4. When the number of layers is increasing from 2, 4 to 8, the grain size is decreasing from 400-200nm to 80nm; the interface between Cu and Al layers are rougher.

The TEM investigations support the XRD and FIB results that the Cu/Al multilayer films on the Si (001) substrate are polycrystalline and random orientated in plane. The interface roughness increases with decreasing layer thickness, and there are some overlap or reaction layers between Cu and Al layers (Fig.5.4).

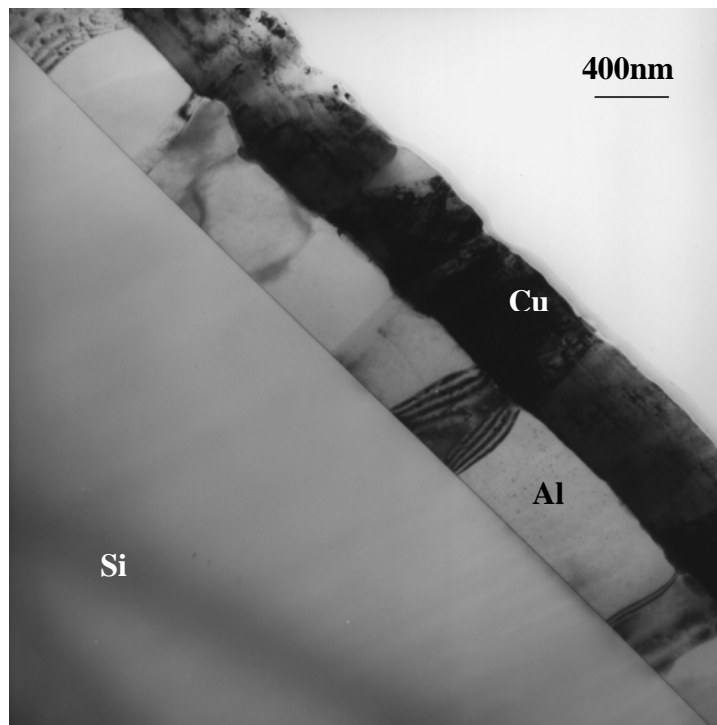
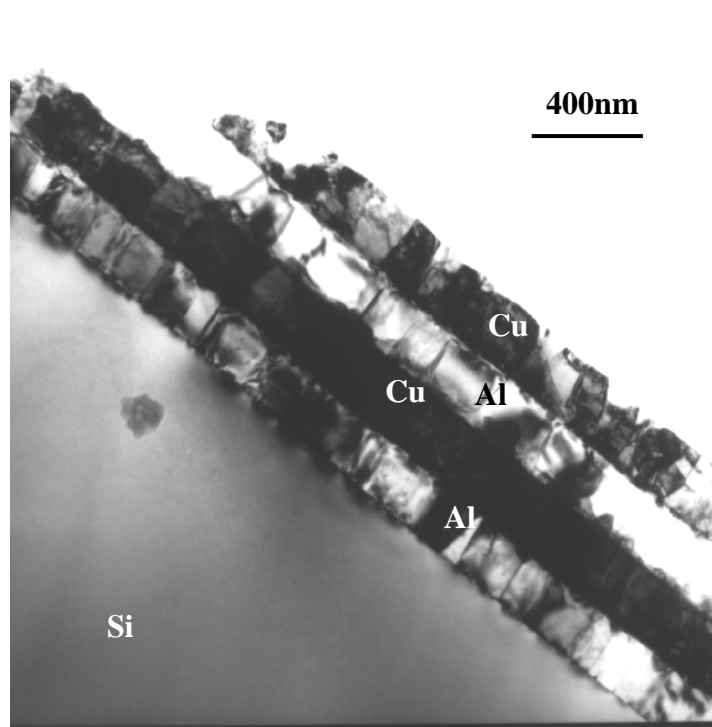
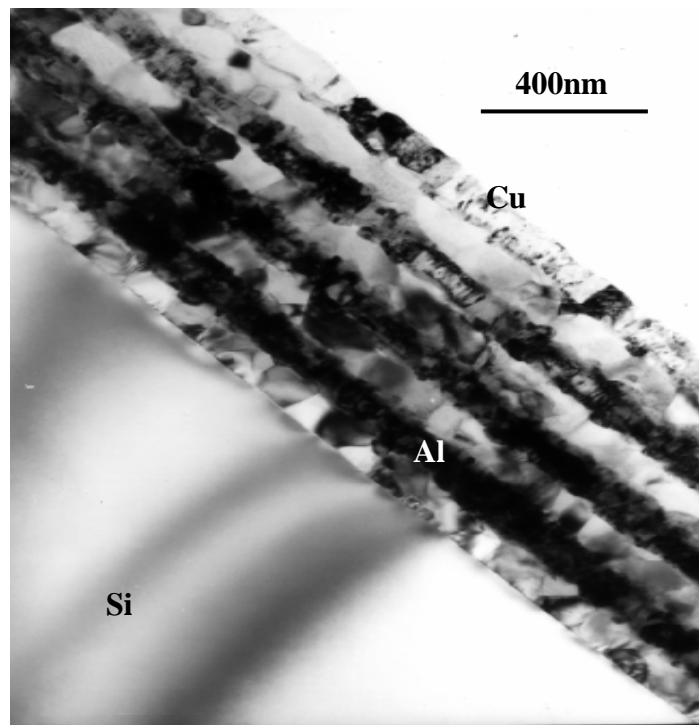


Fig. 5.4 Bright field TEM images for (a) 2, (b) 4 and (c) 8 layers Cu/Al films deposited on Si substrates. The total film thickness is 800 nm. (b) and (c) are on the next page.



(b)



(c)

In summary, the films deposited on Si substrates do not reveal any epitaxial orientation relationship between the various layers and are thus not suitable to perform detailed studies on the Cu/Al interface. Therefore, Cu/Al bilayer films were deposited on sapphire and the results will be presented in chapter 5.2

5.2 Cu/Al bilayer films on sapphire

In order to obtain epitaxial Cu/Al multilayer films, α -Al₂O₃, i.e. sapphire was employed as a substrate. Assuming that the (111) plane of Al stack on the (0001) plane of sapphire, the lattice mismatch is -4%. This is not too large to get a coherent growth. Both magnetic controlled sputtering and molecular beam epitaxy techniques were employed to fabricate Cu/Al bilayer films, trying to get Cu/Al interface with a well defined OR.

The method which leads to higher quality films in terms of epitaxial behavior is then used for further defined investigations.

5.2.1 Cu/Al bilayer films fabricated by sputtering

Cu/Al bilayer films (400nm/400nm) were deposited on the (0001) plane of sapphire at 200°C. The preparation condition has been listed in chapter 4.2.1. After deposition, XRD, FIB and TEM were used to characterize the film. The results and corresponding analysis are described in the following.

XRD

Fig. 5.5 shows the θ -2 θ scanning profile acquired at the Cu/Al/sapphire system. It reveals that only one set of {111} planes corresponding to the FCC structure of Al and Cu are present, which are parallel to the surface of substrate, i.e. (0001) of sapphire.

In order to determine whether the films are single crystalline or textured, pole figures of the {111} planes of the FCC films have been measured. As Fig. 5.6 shows, both the pole figures taken

from $\{111\}$ Cu and $\{111\}$ Al planes reveal six-fold symmetry. In perfect single crystalline FCC samples, the $\{111\}$ set of planes have only a three-fold symmetry in $\langle 111 \rangle$ viewing direction. If there are two sets of orientated planes with $n \cdot 60$ degree rotation (n is odd) in the $\{111\}$ plane, then a six-fold symmetry can be observed in the pole figures indicating the presences of twins. The results reveal that each layer has two, twin-related OR with the substrate. The orientation relationships are: $\pm (111)_{\text{Cu}} [-110]_{\text{Cu}} // \pm (111)_{\text{Al}} [-110]_{\text{Al}} // (0001)_{\text{sapphire}} [2-1-10]_{\text{sapphire}}$. The \pm sign indicates the twin variants.

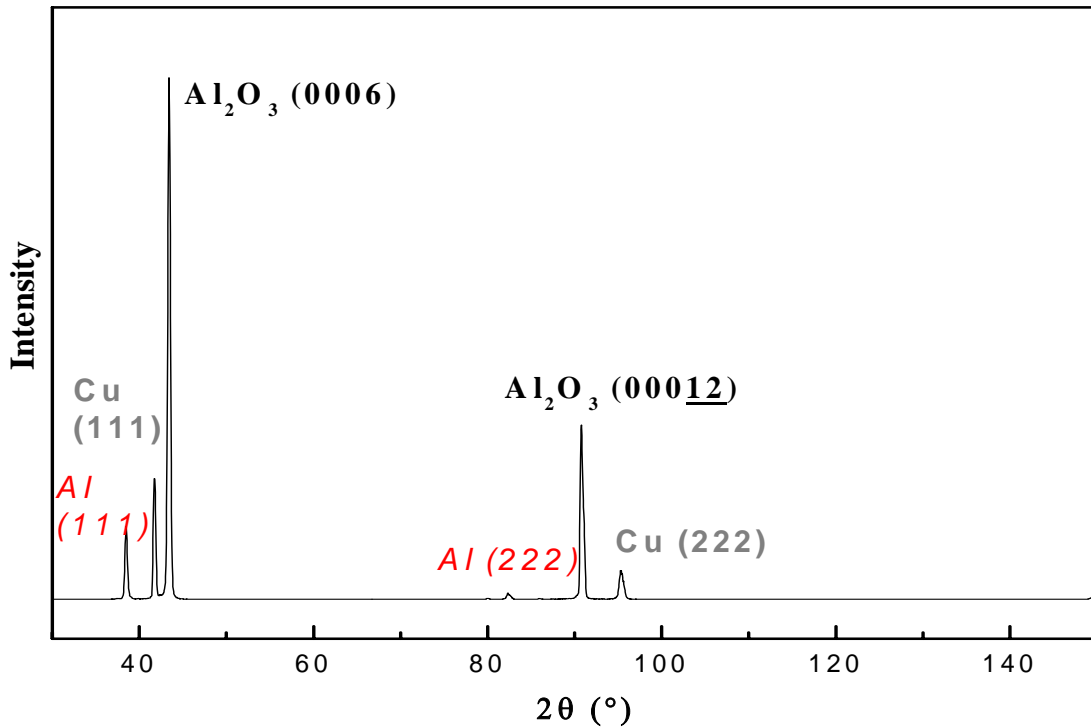


Fig. 5.5 XRD θ - 2θ scan of a bilayer Cu/Al film grown on sapphire (0001) by magnetron sputtering showing that the Cu/Al films are epitaxial to each other and the substrate.

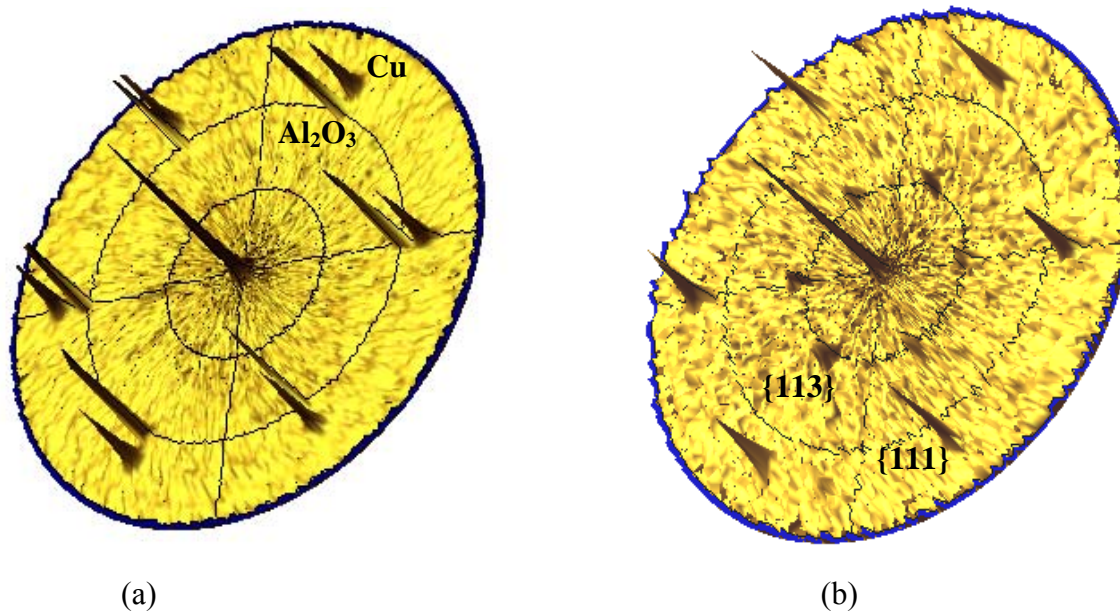


Fig. 5.6 XRD pole figures for (a) {111} Cu layer with {2-1-13} of substrate, and (b) {111} Al layer with {113} of Al were detected from 2*400nm Cu/Al bilayer film grown on sapphire.

FIB

FIB has been applied to determine the microstructure of the Cu/Al/sapphire bilayer film sample. The cross section cut by FIB is shown in Fig. 5.7. The contrast of the Al layer is darker and homogeneous compared to the Cu layer. The inhomogeneous contrast manifests that the Cu layer contains at least two kinds of grains with different orientations. The presence of twin variants was not detected in the chosen area for the Al layer but this might be due to the large size of the twins.

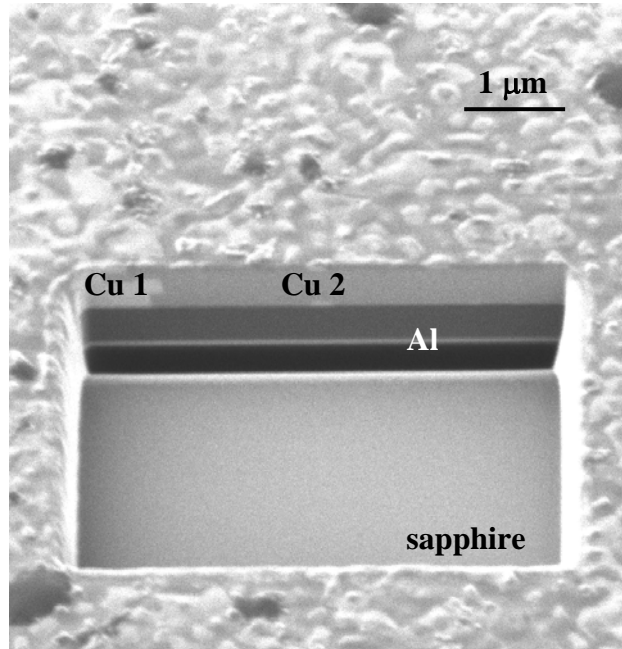


Fig. 5.7 FIB image for a 2*400nm Cu/Al bilayer film prepared by magnetron sputtering on a sapphire substrate.

TEM

TEM studies of the bilayer system revealed that the metal layers have a nominal epitaxial orientation relationship with $(0001)_{\text{sapphire}} // \{111\}_{\text{Al}} // \{111\}_{\text{Cu}}$ and $\langle 2-1-10 \rangle_{\text{sapphire}} // \langle 110 \rangle_{\text{Al}} // \langle 110 \rangle_{\text{Cu}}$, possessing some small-angle grain boundaries. The orientation relationship of the Cu/Al bilayers was determined by CTEM studies and the results are summarized in Table 5.1. As an example, Fig. 8 (a) and Fig 8 (b) show a SAD pattern acquired in $\langle 110 \rangle_{\text{Al}}$ zone axis and the corresponding bright field image.

The SAD experiments revealed that the Cu film consists of two kinds of grains with different orientations. The two variants rotate from each other by 60° in the (111) plane, as the XRD pole figure in Fig.5.6 shows. Combining DP and XRD, the orientation relationship (in and out-of plane) between the substrate and bilayer films can be achieved in more detail. It is found that the in-plane orientation deviates between 6.1° and 7.5° from the perfect OR (see Table 5.1.)

	Cu (111)	Al (111)	sapphire (0001)	in-plane rotation between substrate and film
viewing direction 1)	$\langle 011 \rangle$	$\langle 011 \rangle$	$\langle 2-1-10 \rangle$	$\sim 7.5^\circ$
viewing direction 2)	$\langle 112 \rangle$	$\langle 112 \rangle$	$\langle 10-10 \rangle$	$\sim 6.1^\circ$

Table 5.1. OR of Cu/ Al/sapphire bilayer (400nm/400nm) films prepared by sputtering

From the BF image in Fig. 5.8 (b), it can be deduced that the grain sizes are larger than 1000nm, and that a continuous interlayer between the Cu and Al film exists. The thickness of the interlayer is not homogenous, but ranging from 20nm to 50nm. In some areas the interlayer consists of two layers and there are some Morie fringes present, indicating the occurrence of overlapping crystals in viewing direction, as Fig. 5.8 (c) shows.

The atomic structure of the interlayer was studied by the HRTEM. Fig.5.9 reveals that the region 1 of the interlayer has a different structure, d-spacing and lattice symmetry compared to both Cu and Al layers. Although along $[111]_{\text{FCC}}$ direction, the d-spacing of the interlayer is 0.210nm, which is in between those of Cu and Al (0.2087nm and 0.2338nm), the interlayer has a different structure which does not correspond to pure Cu nor to pure Al. The atomic structure of the region 1 of the interlayer has a four-fold symmetry and is most likely tetragonal, but not FCC. Another region (which is labeled region 2 in Fig. 5. 10) of the interlayer was also viewed in $[110]$ direction of Al, but possesses a different d-spacing along $[111]_{\text{FCC}}$ compared to region 1. The spacing is 0.204nm and also does not correspond to the spacings of Cu and Al. If these two structures parameters are compared to the known thermostable or metastable Cu-Al intermetallic phases, it is found that three alloy phase have the similar d-values, i.e. CuAl_2 , Cu_9Al_4 , for region 1 and Cu_3Al_2 for region 2. The orientations of the possible compounds are listed in Table 5.2. But these alloy phases have very similar d-spacing values, so it is not possible to distinguish them only by HRTEM studies.

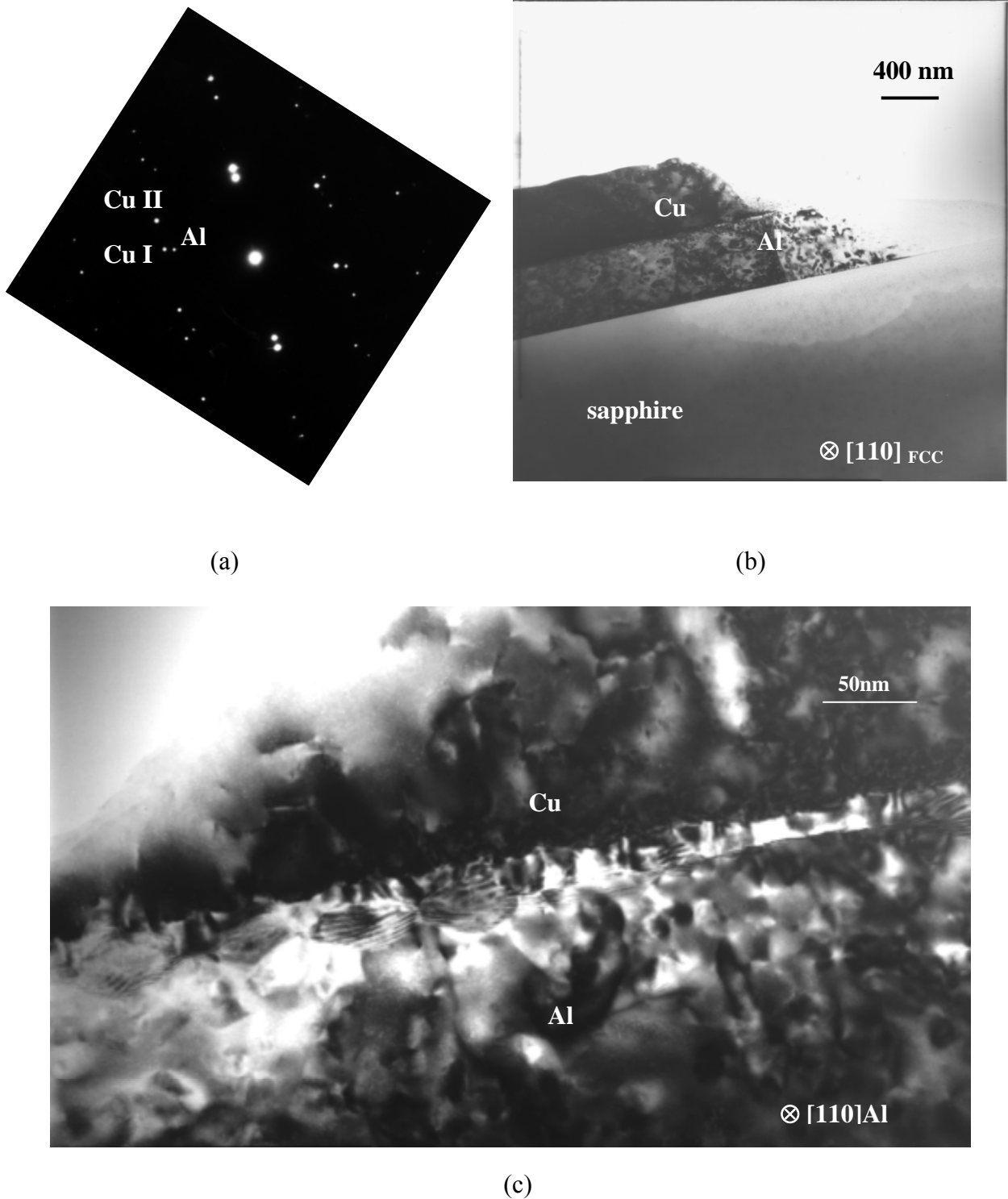
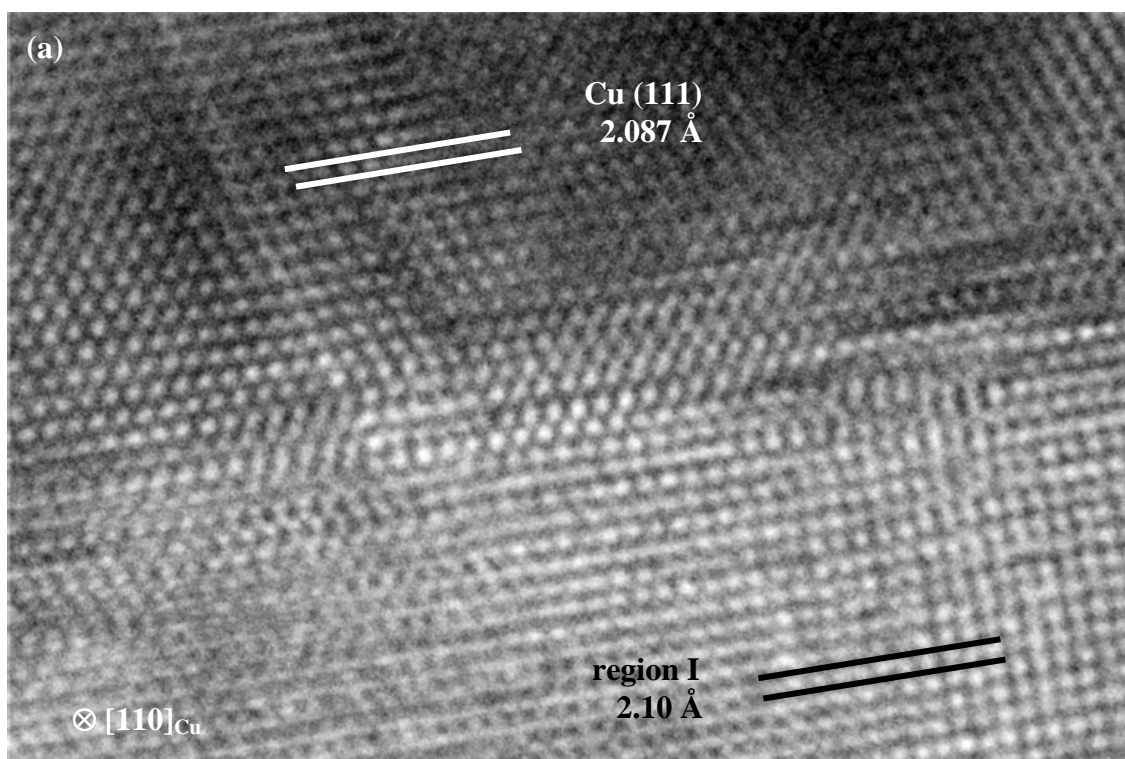


Fig. 5.8 TEM investigation of the Cu/Al films deposited by magnetron sputtering indicate the presences of an reaction layer. (a) SAD pattern of the Cu/Al interface taken in [110] direction, (b) corresponding bright field image, (c) shows a bright field image taken at higher magnification.

Therefore, analytical TEM was also used to study the phases at the interlayer. From the images taken by the VG STEM HB 501 UX (Fig. 5.11 and 5.12), it can be seen that the interlayer consists of two layers possessing different contrasts. EELS spectra were taken from the near-Cu layer and near-Al layer, respectively, and compared with those from the pure metals. In Fig. 5.13, it is obvious that independent of the energy loss region, the EELS data from the near-Cu layer differs from that of the near-Al layer, and both of them are different compared to the pure metals. The different EELS features reveal that these two layers have different electronic structures compared to bulk Al and Cu and each other. It indicates that diffusions must occur between Cu and Al layers, so the chemical composition of the layers at the interface are changed, or that phase transformation happened at this region. Quantification of the spectra was performed using the Digital micrograph software from Gatan, and the relative chemical ratio was calculated and is listed in Table.5.3. With respect to the chemical composition, only two phases could be the candidates for the interlayer, CuAl_2 and Cu_9Al_4 . These results agree with the HRTEM analysis. However, no candidate which fits the HRTEM result for the structure in region 2, was detected by EELS. This might be due to the limited size of the region 2 preventing that EELS data could be taken from this area.



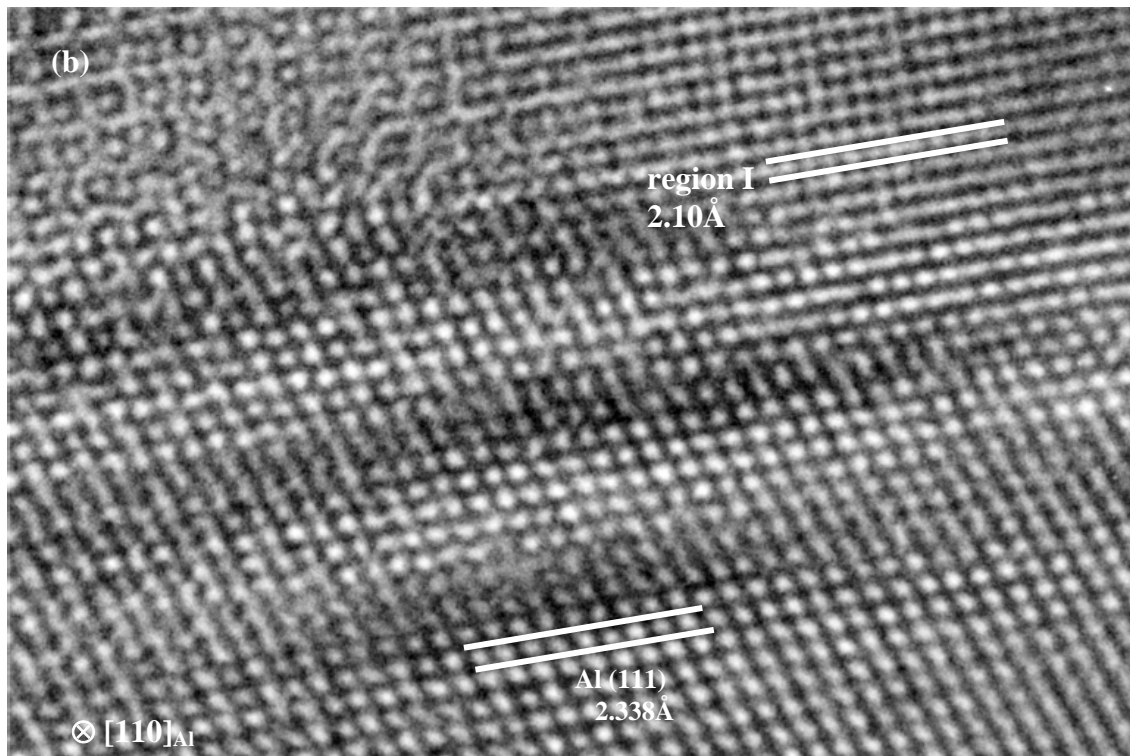


Fig. 5.9 HRTEM image of the interlayer between Cu and Al. Region 1 has a different lattice parameter and symmetry compared to (a) pure Cu and (b) pure Al .

	d1 (Å)	d2 (Å)	d3 (Å)	possible viewing direction // [111] _{FCC}
possible phases for region 1	2,10	2,10	1,48	
Cu₉Al₄	(4-10)	(140)	(530)	⊗ [001]
CuAl₂	(220)	(2-20)	(400)	⊗ [001]
possible phases for region 2	2,04	2,04	1,87	
Cu₃Al₂	(202)	(20-2)	(400)	⊗ [010]

Table 5.2 Possible phases for the interlayers formed at the Cu-Al interface.

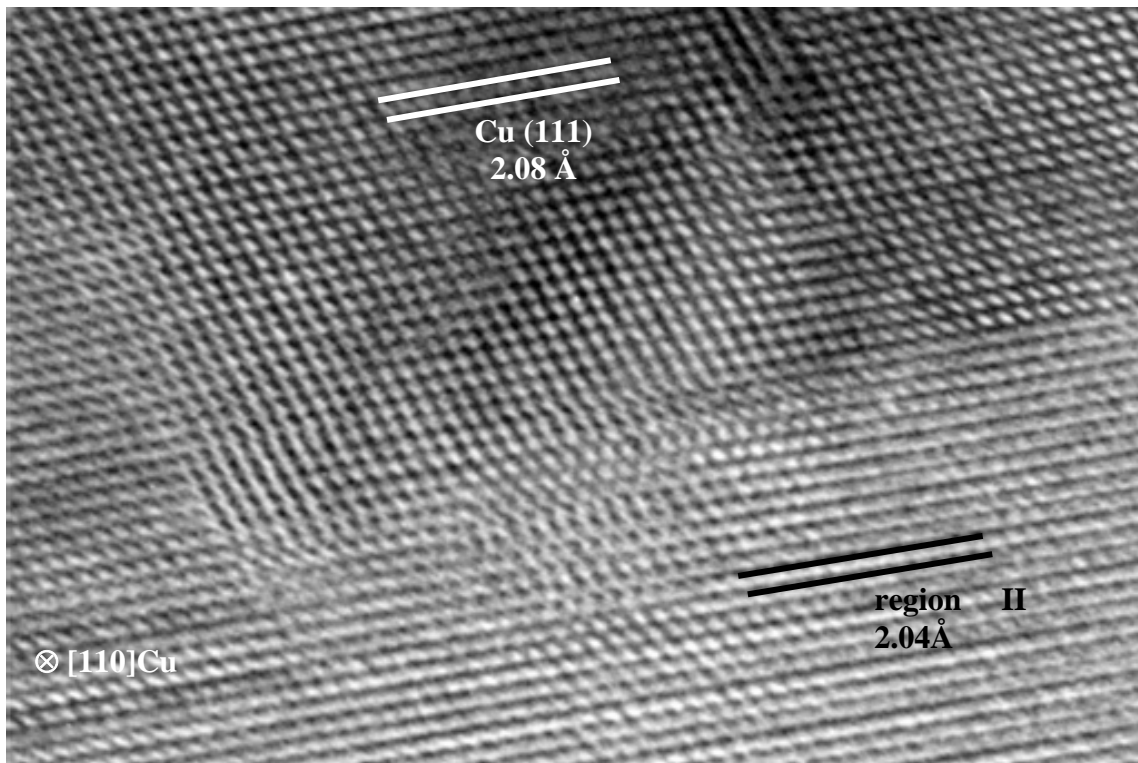


Fig. 5.10 HRTEM image of the interlayer between Cu and Al. Region two has different lattice parameter and symmetry compared to pure Cu (upper part) and Al layers.

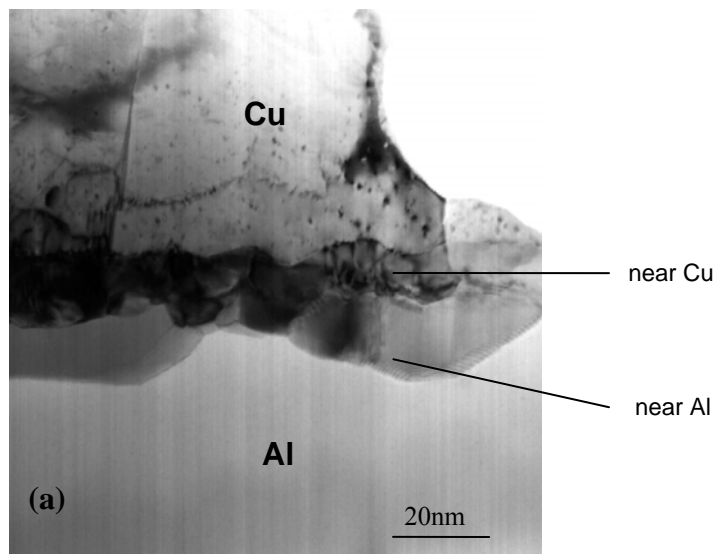


Fig. 5.11 (a) BF STEM image of the interlayers between Cu and Al. The layer near the Cu has different contrast compared to that close to the Al.

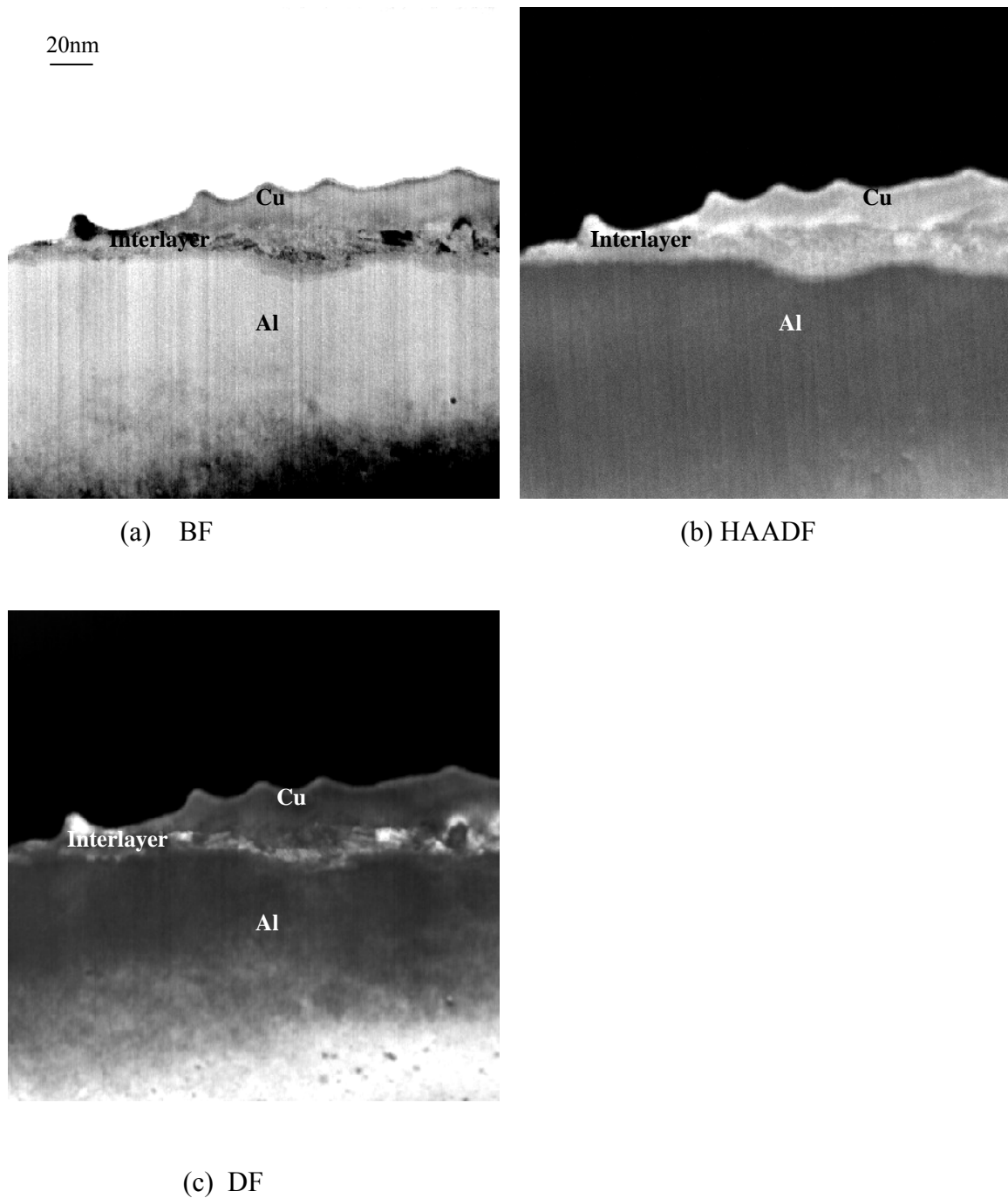


Fig. 5.12 (a) Bright-field, (b) high-angle annular dark field (HAADF) and (c) dark-field images of the interlayer at Cu/Al interface of the bilayer film.

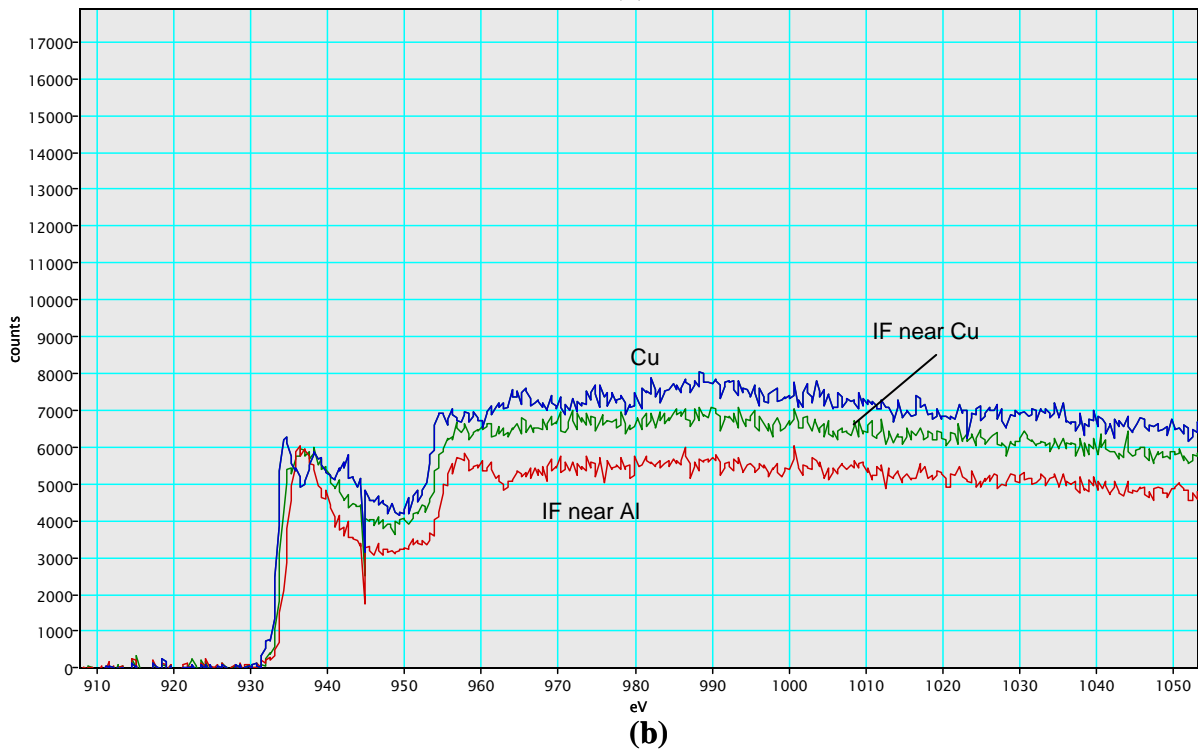
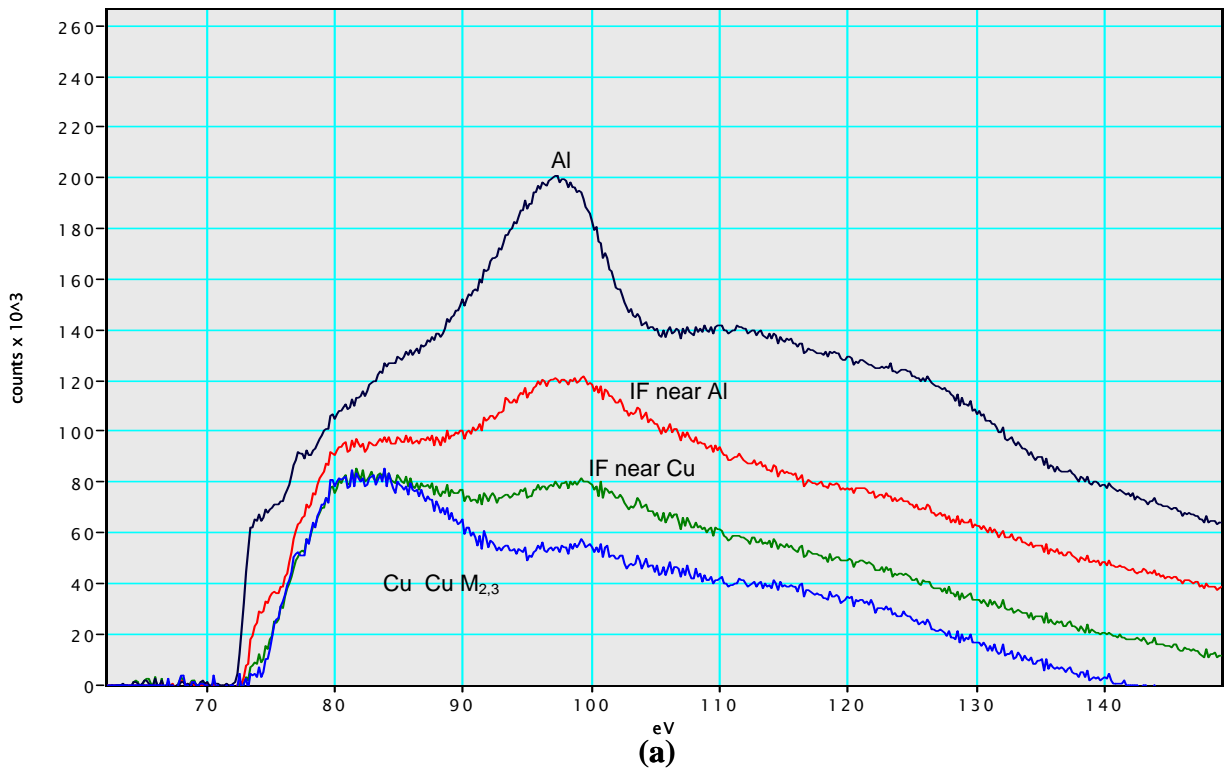


Fig. 5.13 EELS spectra from various regions in the Cu-Al bilayer film. (a) is taken at the Al L_{2,3} and Cu M_{2,3} energy loss region; (b) shows the Cu L_{2,3} edge.

	C_{Al} / C_{Cu}	possible phase
Cu rich part:	$\sim 0.39-0.40$	Cu_9Al_4
Al rich part:	$\sim 1.97-2.53$	$CuAl_7$

Table 5.3 Chemical composition determined by EELS and possible phases at the interlayer between Cu and Al films grown on sapphire at 200°C

Interface between film and substrate

HRTEM experiments revealed that most interface areas possess the orientation relationship as summarized in Table 1. Besides this, a tilt about 3° between the [111] axis of the Al film and [0006] of sapphire corresponding to a 3° deviation between (111) planes of the Al film and (0006) of sapphire was observed; and a distinct layer of 1nm thickness occurs between Al and the substrate (Fig. 5.14). The HRTEM micrographs displayed in Fig 5.14 were taken from different samples. It is assumed that the layer between Al and sapphire is γ -Al₂O₃, which had been found by other studies, and whose formation induces the rotation of the film and substrate.

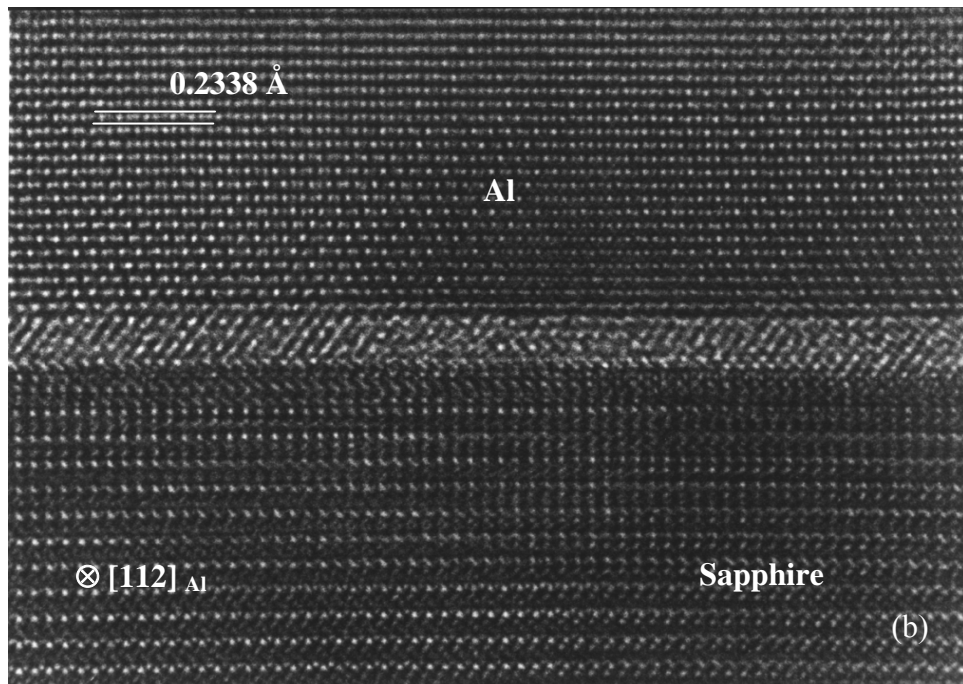
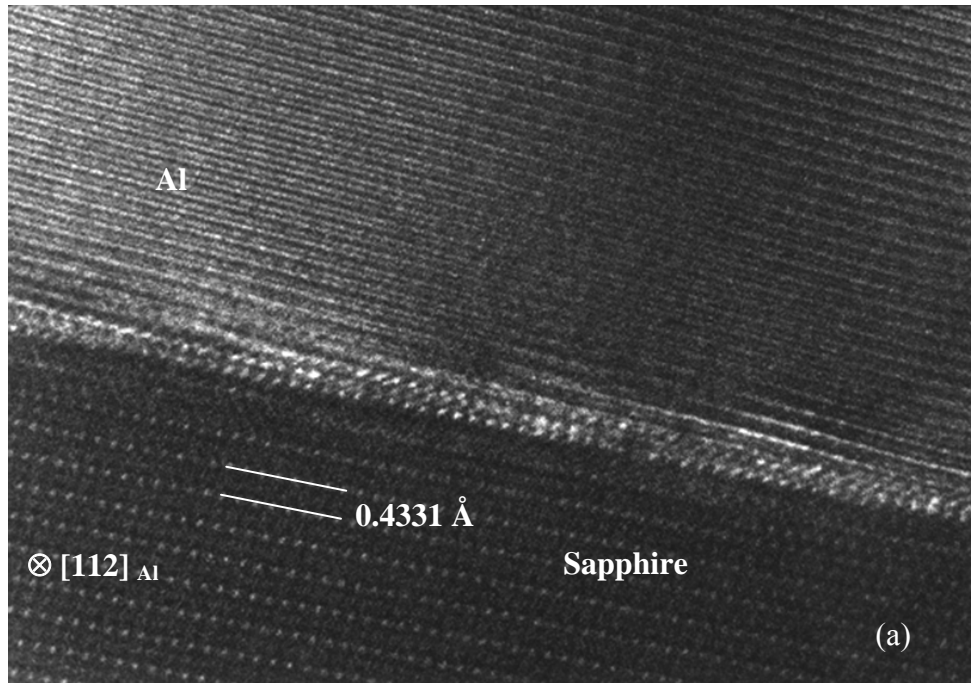


Fig. 5.14 HRTEM images from the Al/Al₂O₃ interface. (a) There is a 3° angle between the (111) plane of Al and (0006) plane of sapphire and (b) reveals a ~1nm thick layer between Al and sapphire.

5.2.2 Cu/Al bilayer films processed by MBE

The Cu/Al bilayer film on sapphire prepared by magnetron sputtering is epitaxial, but the interlayer between Cu and Al consists of grains with different structures and a reaction layer exists between Al and the substrate. In order to get simple Cu/Al interfaces, MBE was applied to fabricate Cu/Al films on sapphire.

XRD and X-ray reflectivity

XRD scan profiles (Fig.5.15) revealed that pure Cu and Al exist in the film, and that this bilayer film is out-of plane orientated compared to the substrate, i.e., $(111)_{\text{films}} // (0001)_{\text{sapphire}}$.

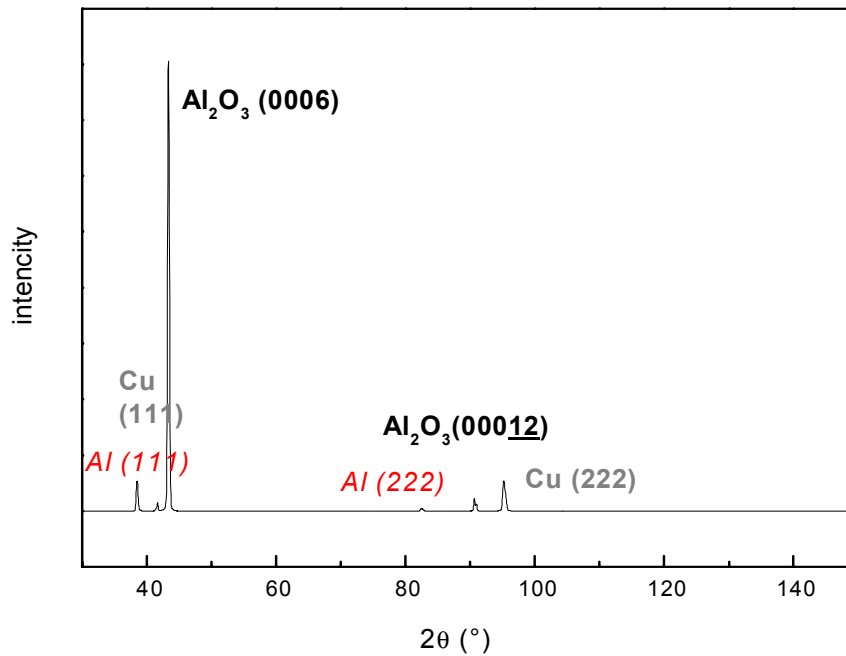


Fig.5.15 XRD profile of the bilayer Cu/Al film deposited by MBE.

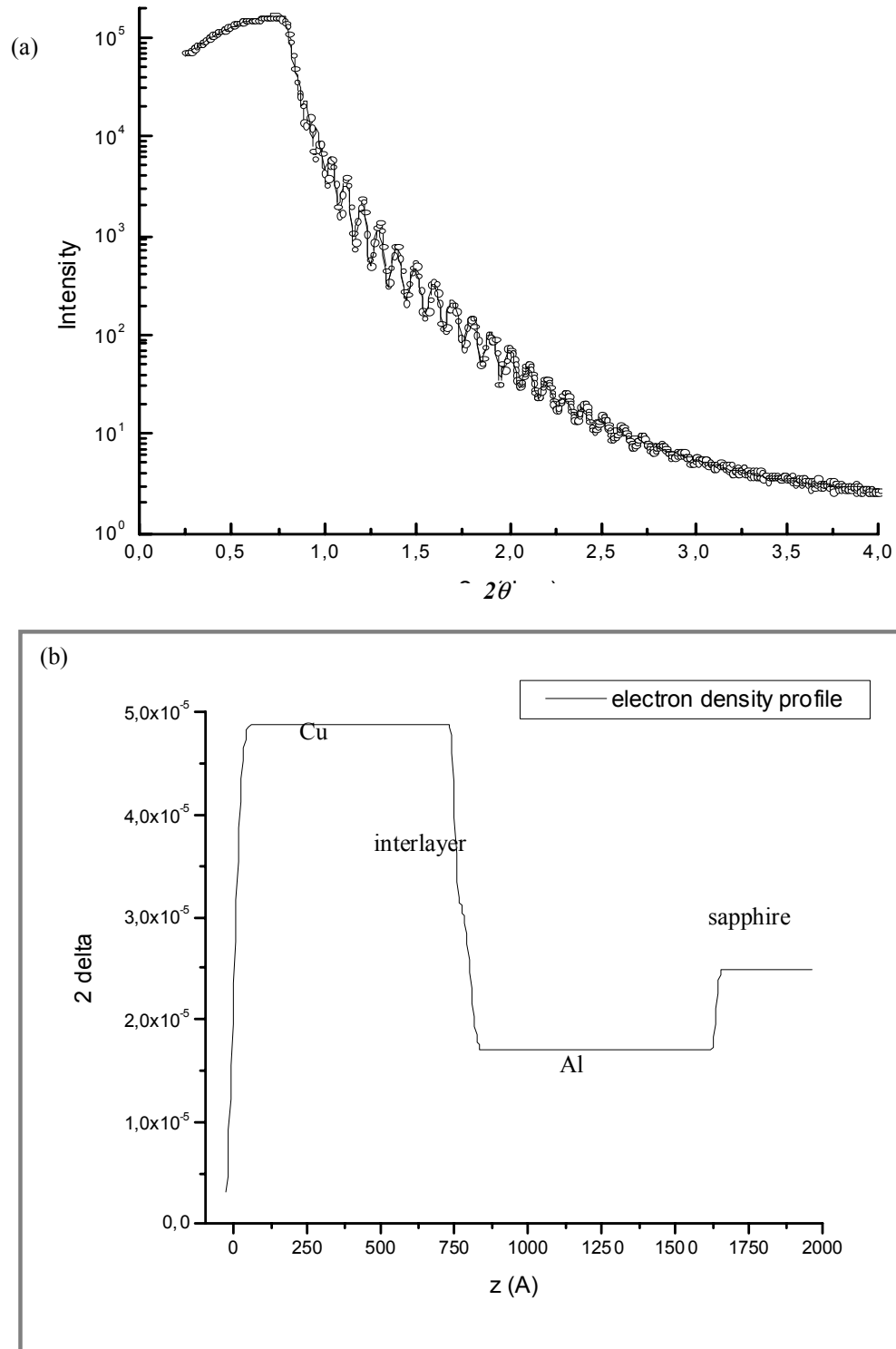


Fig.5.16 (a) The experimental reflectivity curve obtained for Cu/Al/Al₂O₃ (open circles) the simulated reflectivity curve (solid line). (b) is the electron density profile.

The XRR measurements are displayed in Fig. 5.16. The reflected intensity (open circles) is plotted as a function of the magnitude of the exit angle, 2θ (Fig 5.16 (a)). The solid line is a fit to the data points using the Parratt formalism; this allows one to determine the surface and interface roughness, the layer thickness, as well as the electron density profile (EDP) (Fig.5 16 (b)). It reveals that an interlayer is present between the Cu and the Al film with a thickness of 8nm. The electron density of this interlayer is not uniform but gradually changed. The thickness (d) of every layer and the roughness (σ) of every interface also can be determined by the simulation. All of them are listed in the Table 5.4 with a model of the film layers. The system errors are 1% for thickness and 10% for roughness.

thickness (d)	roughness (σ)
	$\sigma_{\text{Cu}} = 18.70 \text{ \AA}$
$d_{\text{Cu}} = 748.58 \text{ \AA}$	
	$\sigma_{\text{Cu/interlayer}} = 7.40 \text{ \AA}$
$d_{\text{interlayer}} = 53.22 \text{ \AA}$	
	$\sigma_{\text{interlayer/Al}} = 15.17 \text{ \AA}$
$d_{\text{Al}} = 835.76 \text{ \AA}$	
	$\sigma_{\text{Al/Al}_2\text{O}_3} = 8.00 \text{ \AA}$

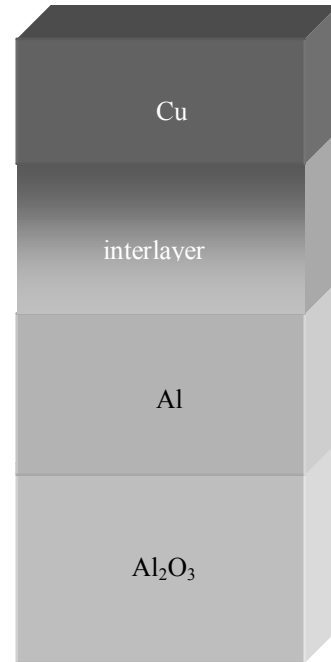


Table 5.4 The values of thickness and roughness of layers in Cu/Al bilayer film

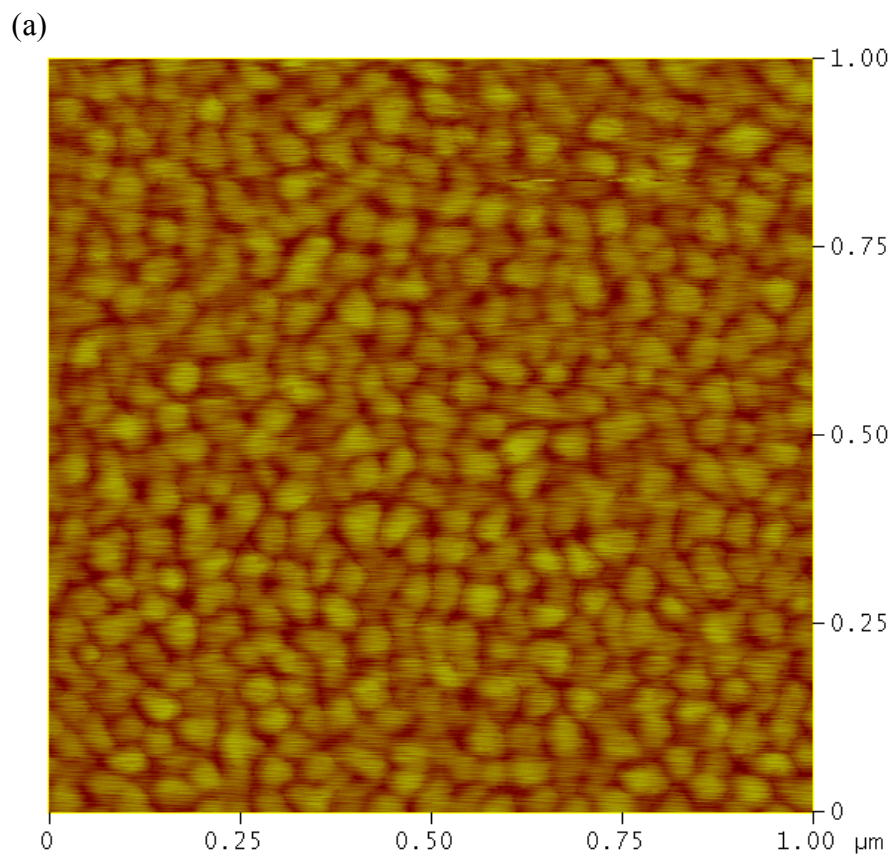
It can be seen that the sum of the thicknesses of the interlayer and the roughness of the Cu/interlayer and Al/interlayer is 7.932nm, which corresponds to the electron density profile.

Another interesting phenomenon is that the roughness of the Cu/interlayer is lower than that of the Al/interlayer, though Cu was deposited on the top of Al.

The open question for this measurement is that, whether the interlayer is a diffusion layer or a layer consisting of an alloy phase(s). Because the electron densities of Al and Cu have not a large difference and the interlayer is not thick enough, this question can not be answered by XRR.

AFM

An Al film (100nm thick) was deposited on sapphire at the same deposition condition as for the Cu/Al bilayer films. After deposition, atomic force microscopy was applied to investigate the roughness of the film (Fig. 5.17). It revealed that the surface of the Al film has a roughness of 8.36 ~ 8.90 nm, very similar to the thickness of the interlayer between Cu and Al. Combing this result with the result from XRR which indicates that the interlayer is about 8nm thick, it is a possible explanation why a mixed layer with ~8.5nm thick can form at the Cu/Al interface and still a flat Cu layer can grow on the mixed layer continuously.



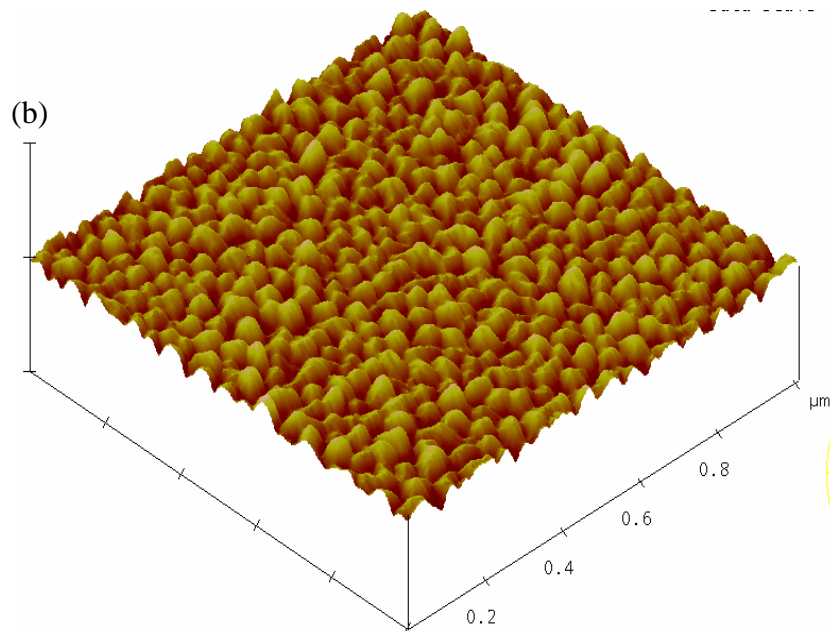


Fig. 5.17. AFM images of 100nm thick Al film grown on sapphire. (a) is in 2-dimentional and (b) is in 3-dimention.

TEM

Bright field TEM images and diffraction patterns from the interface of the bilayer films have been taken. Fig.5.18 illustrates the BF and corresponding SAD in $[112]$ direction of a FCC lattice. In the BF image, it can be seen that a continued interlayer lies in between Cu and Al. In the SAD pattern taken in $[112]$ direction, there are two sets of diffraction spots which belong to pure Cu and Al, respectively. In addition, there are some unidentified diffracted spots, which belong neither to Al nor Cu. The in-plane orientation between the substrate and films could be determined as $(111)[110]_{\text{films}} // (0001)[10-10]_{\text{substrate}}$, and there is no twists between them.

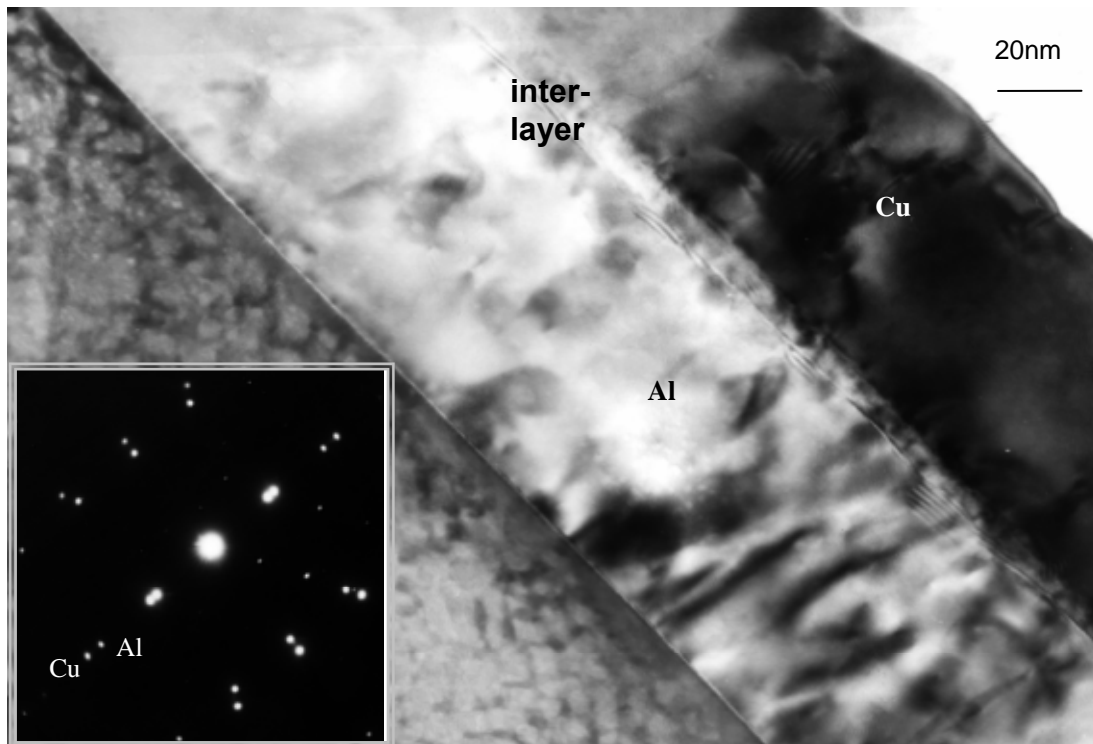


Fig.5.18 BF image and SAD (the inset) in $[112]_{\text{FCC}}$ viewing direction from the bilayer films deposited by MBE revealing the presence of an interlayer at the Cu/Al interface.

HRTEM was used to study the interlayer in more detail. It is found that the interlayer has a different structure than the FCC films, and the structure is not equivalent to the one formed in the specimen Cu/Al/sapphire fabricated by sputtering. Fig.5.19 shows a HRTEM image taken in $[110]_{\text{Al}}$ direction. The atomic stacking sequence varied from ABCABC in Al and Cu to ABABAB in the interlayer, parallel to the $[111]$ direction of FCC. This ABAB stacking sequence corresponds to that of a HCP structure in close packed direction, $[0001]$ HCP. The d-spacing of the interlayer is 0.423nm, larger than the double (111) d-spacing of Cu, however smaller than that of Al.

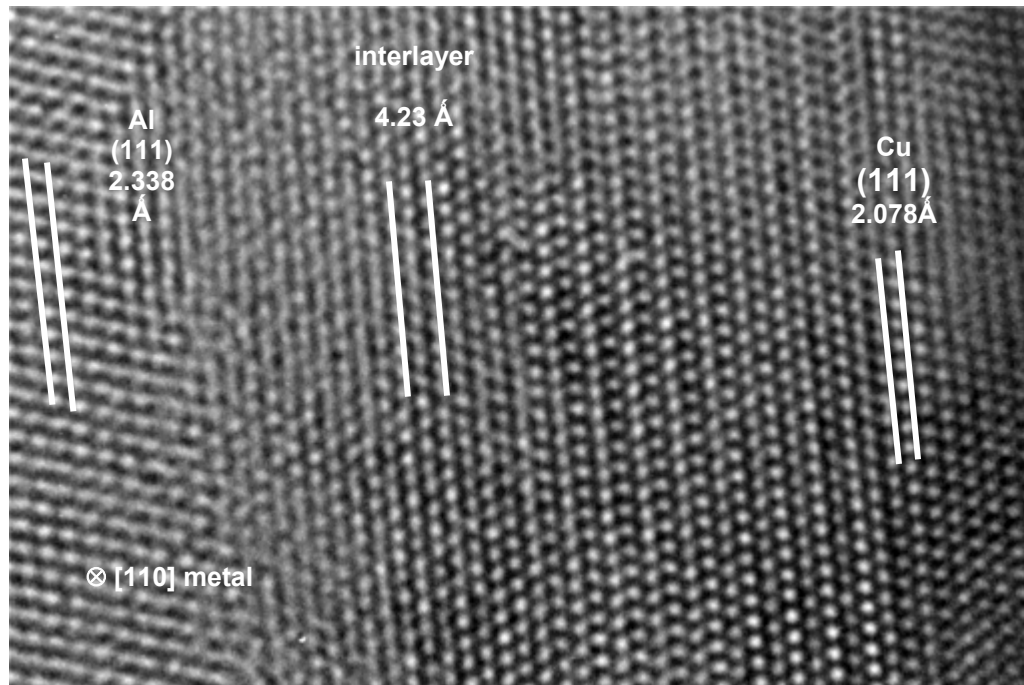


Fig.5.19 HRTEM image of the interlayer in Cu/Al bilayer films deposited by MBE. It is taken in [110] direction.

The interlayer contains also defects and some areas have a curved interface to Cu and Al. Fig.5.20 shows as an example a dislocation generated at the interface between Cu and the interlayer. In [111] direction of FCC, the stacking sequence of atoms is ABCABC in Cu and Al, while it is ABABAB for the interlayer. The atoms at left-down side of the dislocation are with an ABABAB stacking sequence, but the right-up side is with an ABCABC sequence. It is a direct illustration for the FCC to HCP transformation. This dislocation is a Shockley partial dislocation. When it has gone through the whole interlayer along the interface, a perfect interface could be formed. Simulation will be used to check this point.

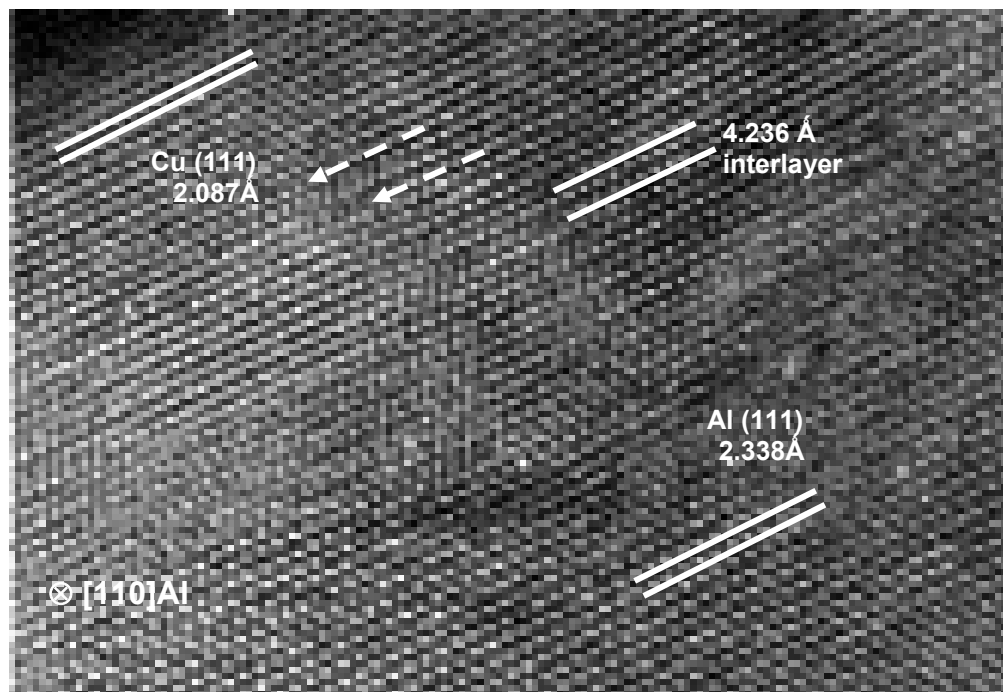


Fig.5.20 A dislocation, which is adjacent to the Cu layer and located between the two arrows. The left side has a HCP structure, while the right part is still FCC. The image was taken in $[110]_{Al}$ zone axis.

HRTEM also allows to determine whether the interlayer possesses one unique orientation relationship to the metal films. As Fig.5.21 (on next page) revealed, in $[112]$ view direction of Al, the HCP structure from a different area shows the same lattice image as that in $[110]$ view direction of Al, i.e. Fig.5.20. This means the HCP interlayer may have another OR with the bilayer films. This is similar to the observation between films and substrate in sputtered sample on sapphire where two kinds of OR were found. While most of the TEM specimens only reveal the OR between the interlayer and based metal films as that in Fig. 5.20.

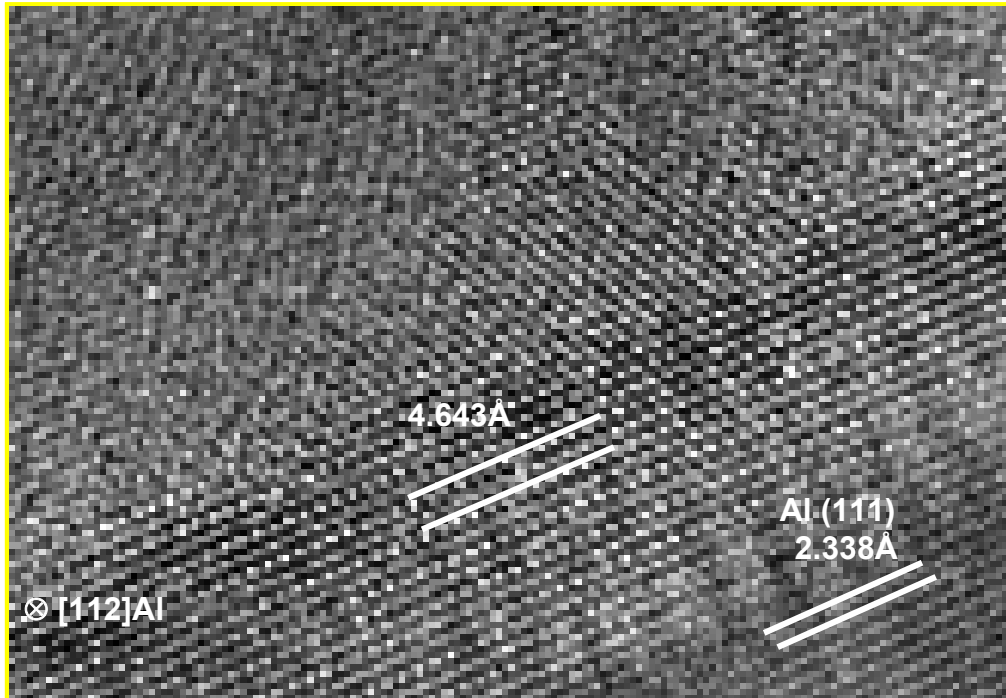


Fig. 5.21 HRTEM image of the interlayer and Al film taken at a different location compared to the one shown in Fig. 5.20. The image was taken in $[112]_{\text{Al}}$ zone axis.

Quantitative HRTEM

Quantitative HRTEM involves mainly two steps. The first is to simulate HRTEM images according to an atomic model, using the software package EMS ^[Stadelmann]. The second is to compare the simulated images with the experimental images pixel by pixel, then adjusting some parameters (atomic model or image conditions) until the best agreement is achieved, so the best structure or imaging condition can be determined. This step is performed by a software package called IDIM^[Möbus]. In this work, a reference with known structure is required to find the optimum image conditions, since the interlayer has an unknown structure. The details are as follows: according to the reference with known atomic structure (Cu or Al), a map of HRTEM images was calculated by EMS

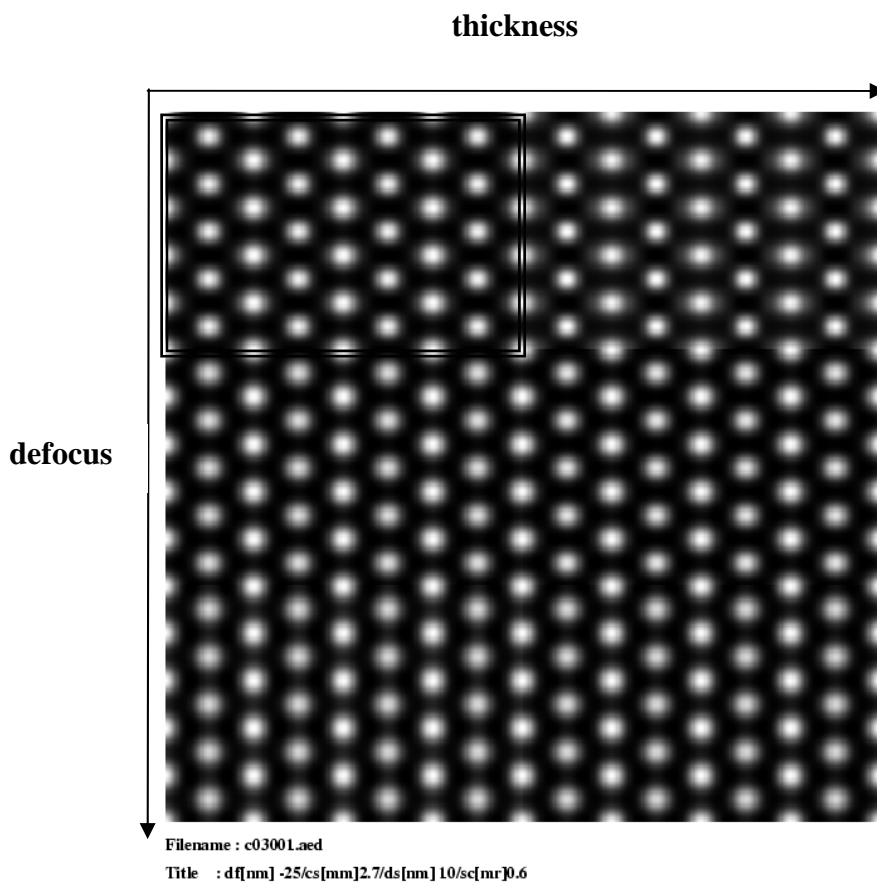


Fig.5.22 Simulated HRTEM image map made by EMS. The lattices in the box have the same image conditions, i.e. same thickness and defocus. There are 6 kinds of image conditions in this small map.

(Fig.5.22 shows a part of this map). The map has two imaging condition parameters, thickness and defocus. Comparing the image contrast of the experimental images with that of the map manually, the best imaging condition regions are found. Keeping these two imaging parameters in the fixed regions and adjusting the other parameters, for example, tilting angles, the software of IDIM can automatically find the best imaging condition by comparing the simulated images with the experimental one. The degree of similarity between them is given by the cross-correlation function (XCF), which is also calculated by IDIM. By repeated adjustments and comparisons, the best fitting results of the best imaging conditions of the reference could be determined precisely. Because the interlayer had been taken in the same image as the reference, it should have the identical imaging

conditions. Applying the image conditions of the best fitting for reference to the atomic model of the interlayer, an image can be simulated by EMS. With the same process, IDIM can compare the simulated one to the experimental one, and thus the model's reliability could be evaluated by the value of the XCF. If the XCF of the image simulated for the new phase with unknown structure is nearly as high as the XCF of the reference (Cu and/or Al) with the known structure, the assumed atomic model for the new phase is reasonable.

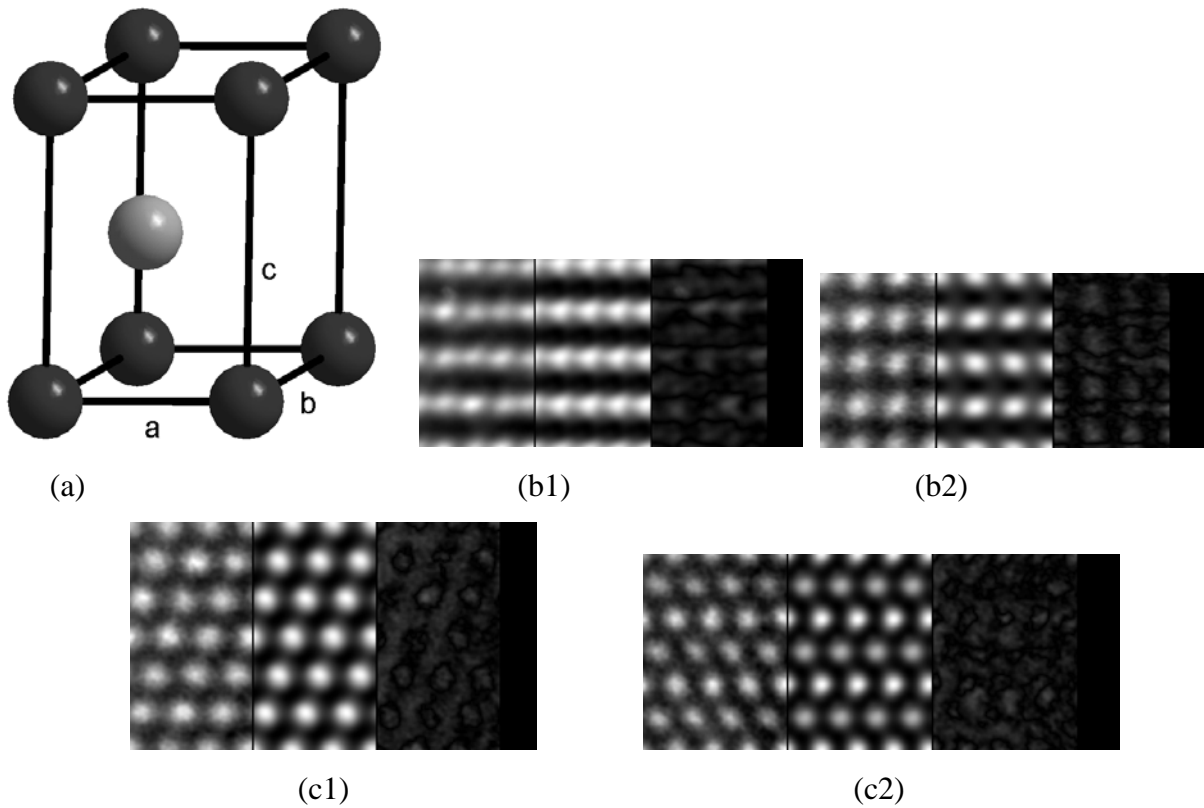


Fig.5.23 (a) Atomic model of the HCP structure used in the simulation with $a = b = 0.256\text{nm}$, $c = 0.419\text{nm}$. (b1) Comparison of an experimental micrograph (left side) and the best fitting contrast simulated image (middle) for Al in $[112]_{\text{FCC}}$ viewing direction, the right side shows the difference image of the experimental and simulated image and the XCF is 96.9; and (b2) is the comparison for HCP structure in the same view direction with 93.4 for XCF. (c1) is the comparison between experimental and simulation images for the reference Cu in $[110]_{\text{FCC}}$ direction, and (c2) is the comparison for the HCP structure in $[10-10]$ direction, with the XCFs are 95.9 for reference and 93.1 for HCP.

According to the experimental HRTEM image, a preliminary HCP atomic model with $a = b = 0.26\text{nm}$ and $c = 0.42\text{nm}$ was constructed for simulation work. The assumed orientation relationship between the FCC metals and the HCP interlayer is $\langle 110 \rangle (111)_{\text{FCC}} \parallel \langle 10\text{-}10 \rangle (0001)_{\text{HCP}}$. The best XCF of the simulated image in $[110]_{\text{HCP}}$ viewing direction obtained is 93.4%, which is close to 96.9%, the XCF of the reference Cu in $[110]_{\text{FCC}}$ viewing direction. To gain this high XCF value, the HCP atomic model had been adjusted to 0.2566 nm in a and b direction and 0.4187 nm in c direction, as Fig. 5.23 shows. If only one 2-dimensional image is used, it can not be concluded whether the 3-dimensional atomic model is correct. Thus the quantitation evaluation also had been performed on the HRTEM images taken in $[2\text{-}1\text{-}10]_{\text{HCP}}$ viewing direction, which is parallel to $[112]_{\text{FCC}}$. The HCP model with best fitting in $[110]_{\text{HCP}}$ viewing direction was fixed and Cu but not Al was chosen as reference since it had better quality in that image. In this direction, the XCF of the simulated image with HCP model is still as high as 93.1% (Fig. 5 (c)). These results confirmed that the interlayer has a HCP structure.

Lattice distortions at the interlayer

HRTEM revealed an interlayer with HCP structure connecting both Cu and Al. There is a lattice mismatch of $\sim 10\%$ between Cu and Al (the lattice constant of Cu is 0.3865nm and that of Al is 0.4095nm), and it looks like that lattice deformation may exist in this HCP structure. The lattice distortion was determined using the distance between 10 atoms measured near the Cu side and near the Al side, respectively (Fig.5.24). It is 340 pixels for the atoms near the Cu side, but the distance increases to 348 pixels for the atoms near to the Al side. It should be pointed out that these measurements were made by hand. A better accuracy could be reached by using the software named LADIA (LAttice DIstortion Analysis) ^[Du] which was employed further to investigate the HRTEM images from the interlayer.

The principle of the LADIA program is: some (at least two) columns were chosen as the reference, and the average lattice constants will be set as the values of the reference lattice; then the whole lattice (built by all atoms) will be compared to the reference and the relative difference between them will be plotted. This comparison only provides a relative difference, if the deformed

part is set as the reference, then the perfect part will show ‘distortion’. It is important that the reference lattice has the same crystal symmetry as the investigated part, otherwise the results are not reliable. The limitation of this programme is that it only can be applied to HRTEM images, whose 2-dimensional lattices are centre-symmetric in viewing direction. Because in [10-10] viewing direction of HCP, the 2-dimensional lattice is near-centre-symmetric but not centre-symmetric, it was divided into two sets of lattices according their various positions, i.e. atoms at near-centre and atoms at corner, then both of these sets were analysed by LADIA, separately.

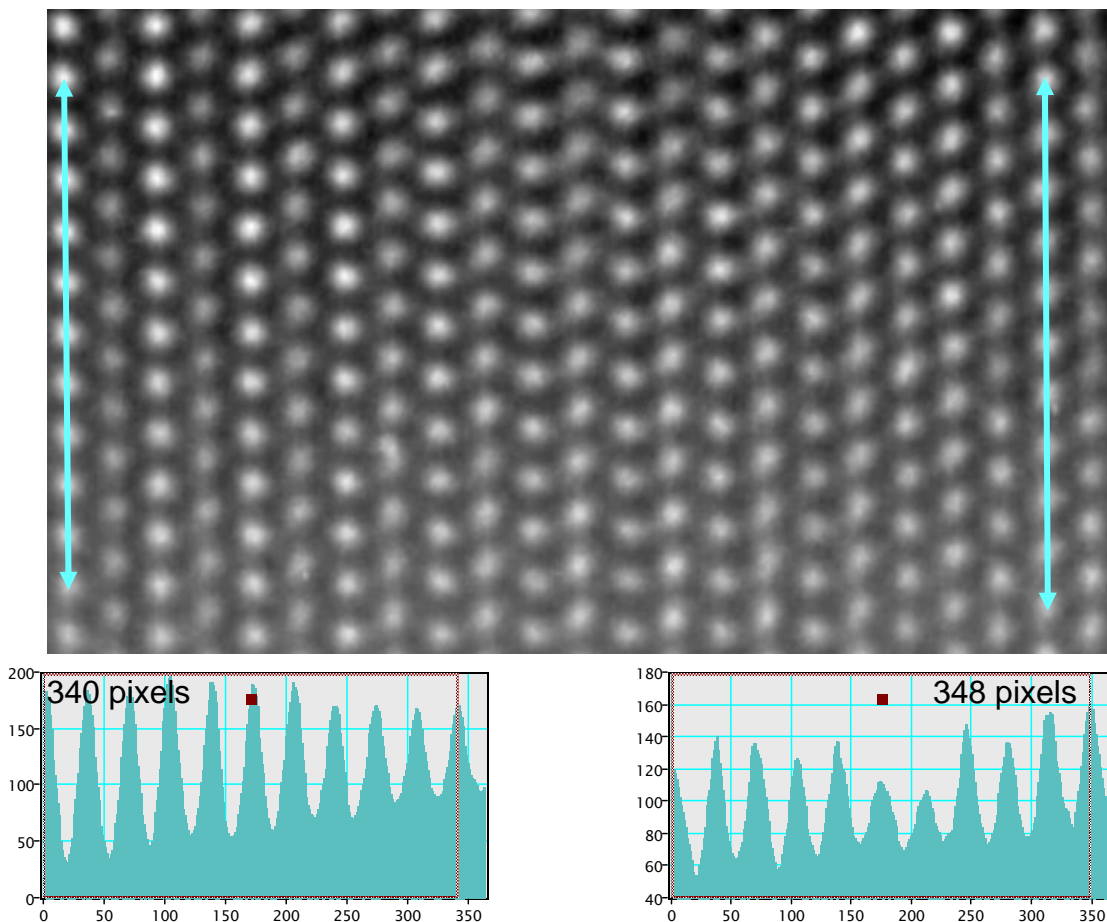
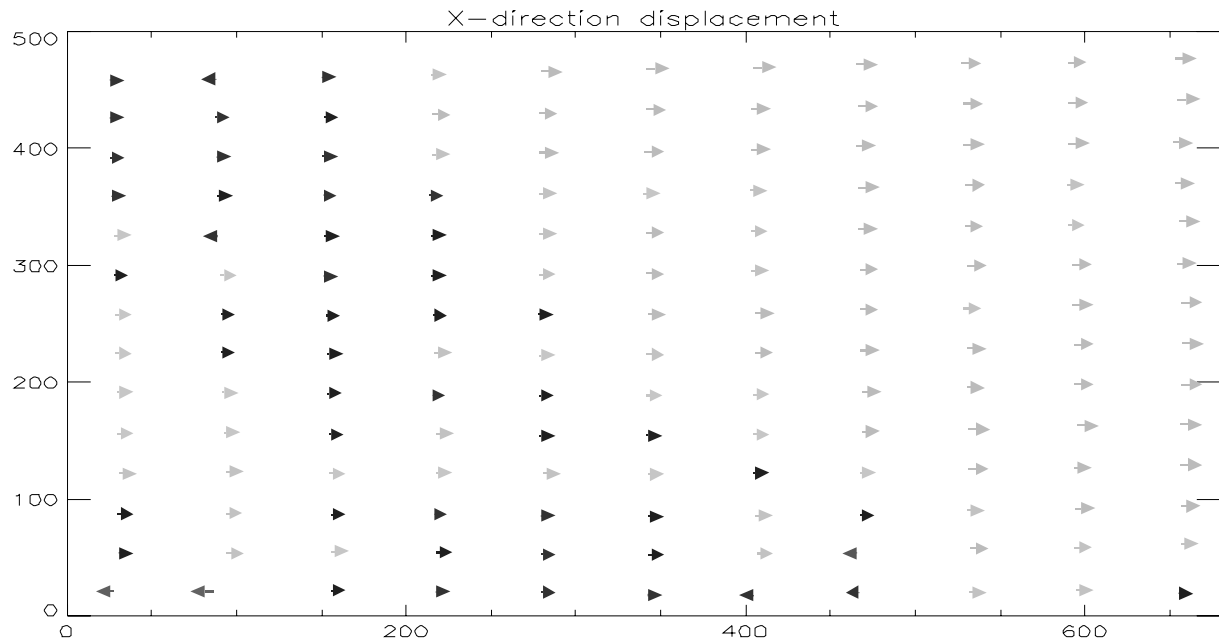
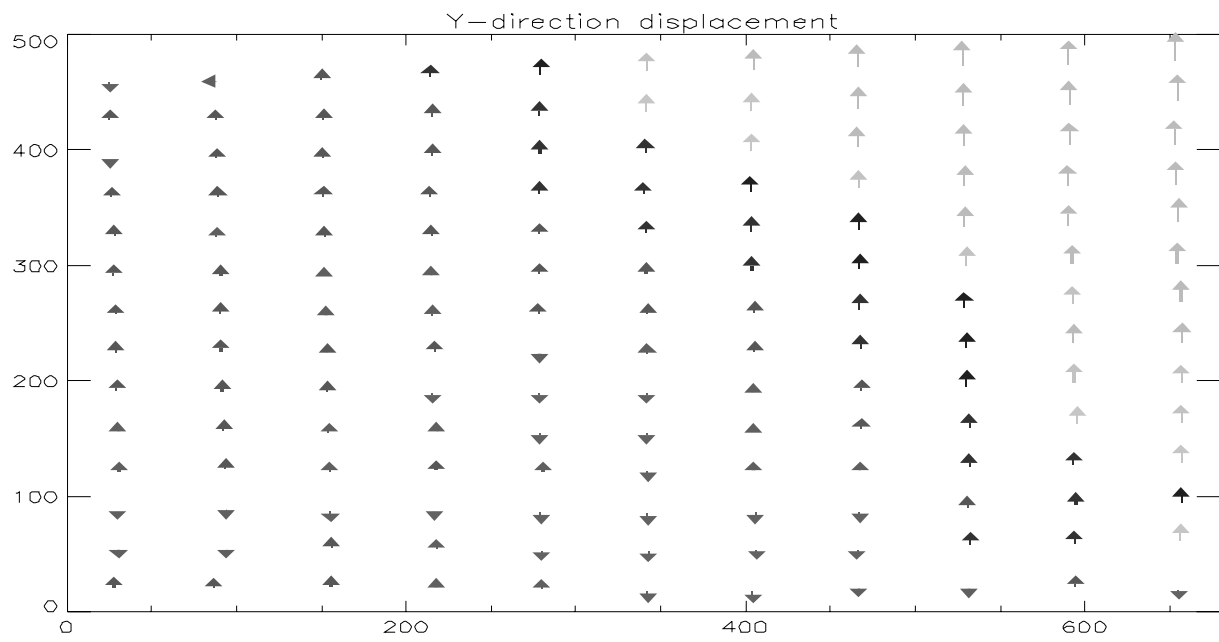


Fig.5.24 HRTEM image of the interlayer (up). The Cu layer is near to the left side and the Al layer is near to the right side. The whole distance between 10 atoms is 340 pixels for the atoms near Cu and 348 pixels for the atoms near Al.



(a)



(b)

Fig. 5. 25 Lattice deformation map of the interlayer. The reference is the left two columns. The head of the arrow is the real atom position and the end is the ideal position. The length of the arrow indicates the degree of deformation.

During this analysis, two columns which are nearest to the Cu layer were chosen as the reference. The analyzed results from both sets of lattices revealed that from near-Cu-side to near-Al-side, the lattice of interlayer is expanding in both x and y direction. Fig. 5. 25. shows the results from one set of the lattices. Since the interlayer was assumed to have HCP structure in which the a axis is identical to b axis, and the Y direction in HRTEM image is the same as the direction of $(a-b)$ vector in HCP atomistic model, the expanding in Y direction indicates that the HCP structure is growing in both a and b direction. The X direction in HRTEM, corresponds to the c axis in the HCP atomistic model. So the LADIA analysis provides the information that the interlayer is expanding in 3-dimensions from the Cu side to the Al side.

The results from LADIA also indicate that the atomistic model for the interlayer is accurate for the special area but will change for a large area, due to lattice distortions.

EELS and EDS

The chemical composition of the Cu/Al films were studied by energy dispersive X-ray spectroscopy in a VG HB 501 UX dedicated STEM operated at an accelerated voltage of 100 kV.

In order to investigate the chemical composition of the interlayer and the interdiffusion between Cu and Al, EDS linescans were taken. As has been described in the fabrication of the CuAl_2 reference, the average k -factor in the Cu-Al system was determined from this sample to amount to 1.6 ± 0.03 . Combining all of the intensity ratios from Al to Cu across the interlayer with this reference k -factor, the relative chemical composition at different area was obtained. Four EDS linescan experiments were performed and they are indicated in the bright field image in Fig. 5.26. The distance between one spot measurement within each linescan was 2.5nm in the interlayer and a 5nm step size was chosen in both metal layers. Since the interlayer is only around 8nm thick, while the minimal step length is 2.5 nm, it is hard to get a precise spatial distribution within the layer. Four profiles were measured where the chemical content is plotted against the distance, to understand the

chemical variation in this Cu-Al bilayer system (Fig.27). In the profiles, the Al/HCP interface was set as the origin. Considering the interlayer is around 8nm thick, the boundaries of the interlayer could be marked, and from this area the chemical composition of the interlayer was defined. It revealed that the interlayer has a broad chemical composition from the interlayer to both pure metal layers, exhibiting the typical concentration profiles for interdiffusion.

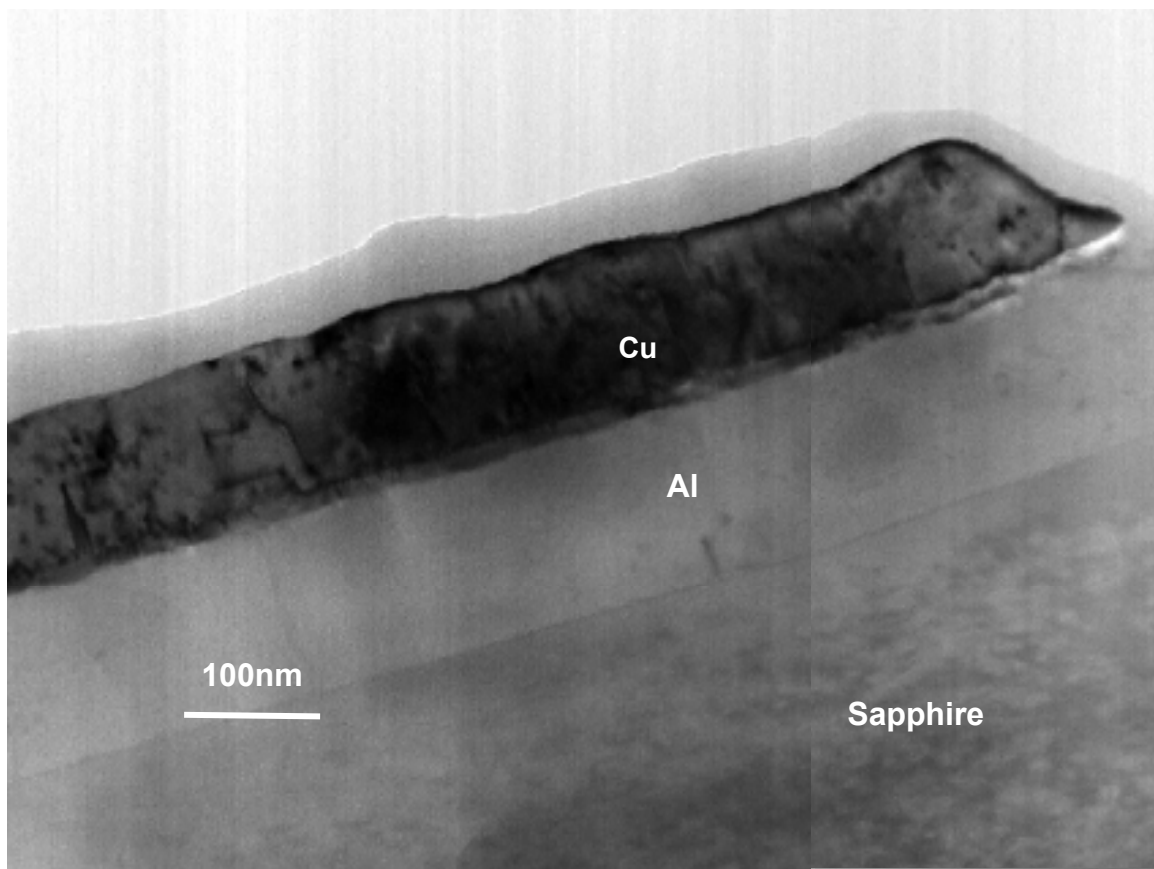


Fig.5.26 STEM bright field image of the Cu/Al bilayer system with an interlayer occurring at the Cu/Al interface. Four different position were chosen, where EDS linscans experiments were performed.

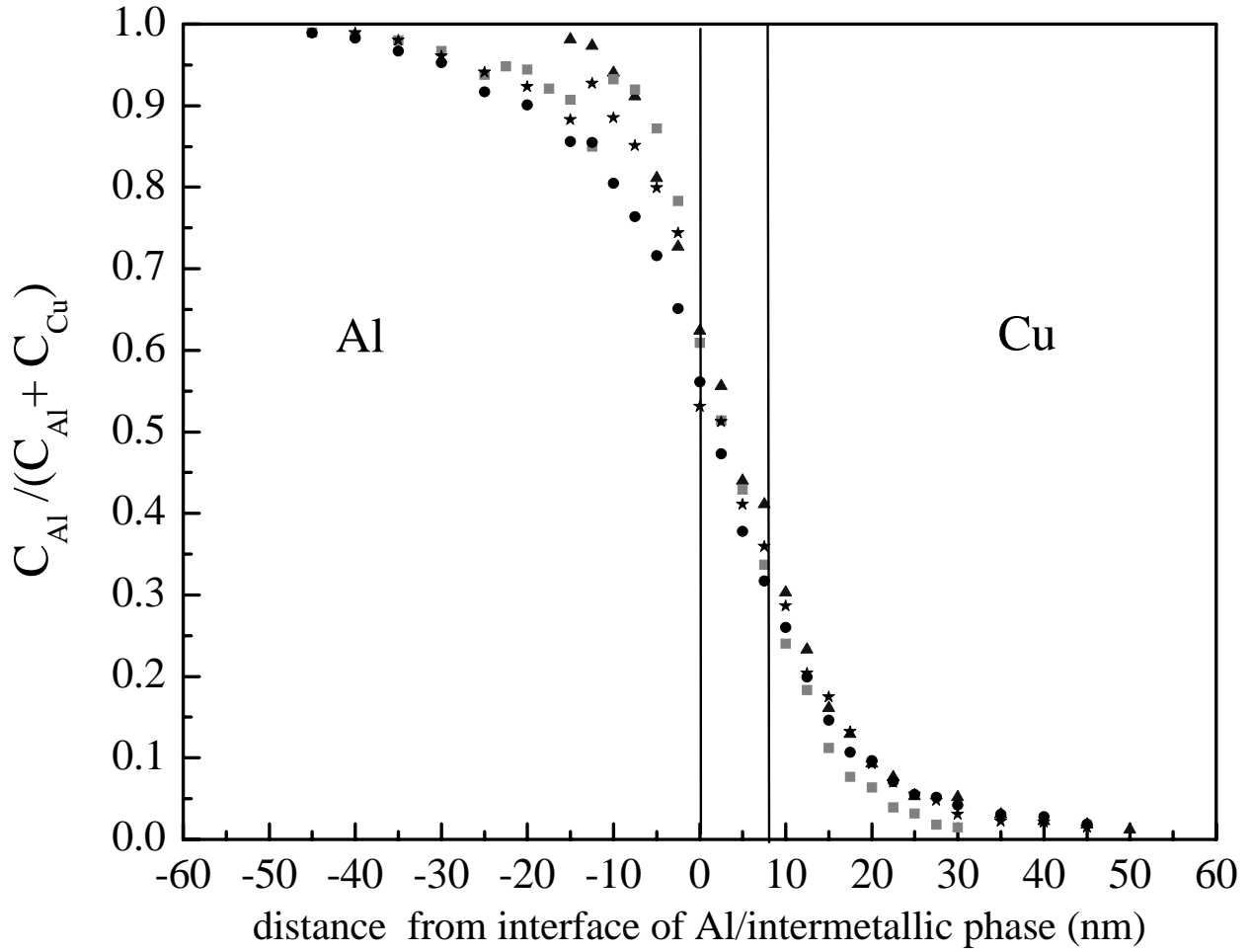


Fig.5.27 Linescan performed across the intermetallic phase from Al to Cu side. Different measurements are presented by symbols with various shapes. The position of the HCP layer is marked by the two lines. The width of the layer is 8nm as determined by HRTEM images.

Besides EDS, EELS experiments also have been performed for the bilayer Cu-Al films on sapphire. Fig.5.28 displays the profiles captured at the Al L_{2,3} edge and Cu M_{2,3} edge respectively, which lie in the same energy loss region. It reveals that going from the Al to the Cu layer, the ELNES

is changing. This indicates also that the chemical concentration is gradually changed from one of the pure metals to another; Al and Cu should be mixed at the interlayer; and the chemical content range of the interlayer is gradually changing between the two metal layers. But quantification / calculation for the chemical composition is difficult due to the overlapping edges.

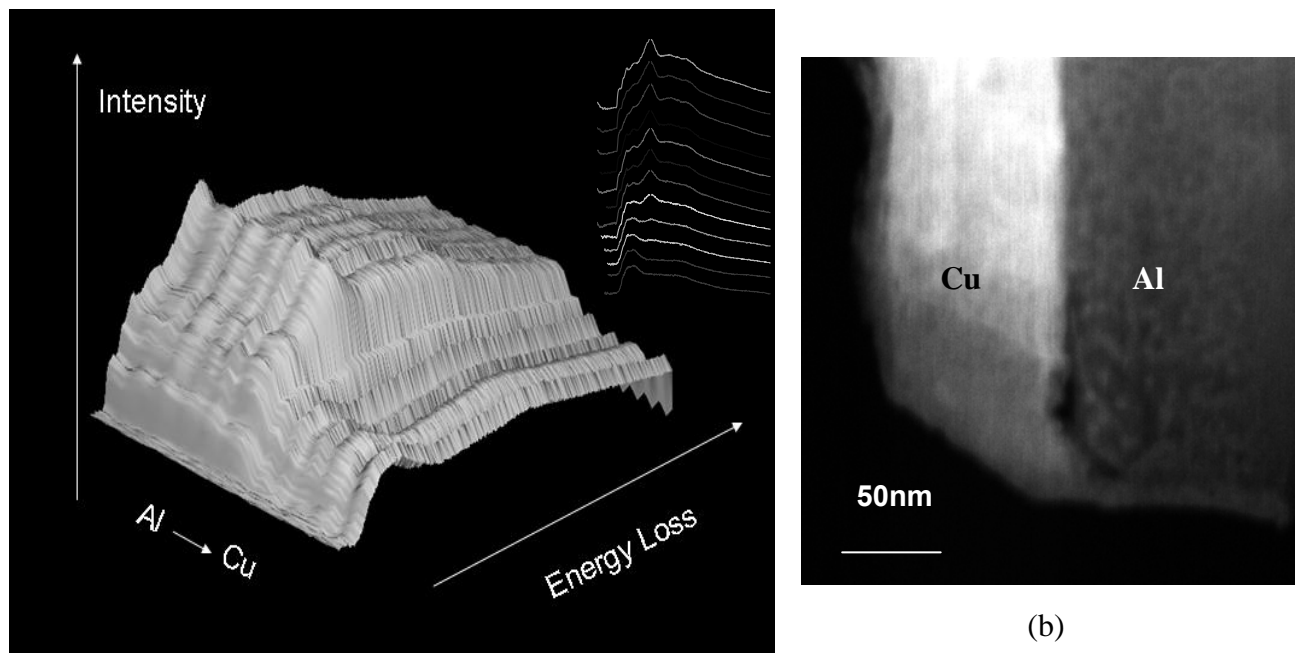


Fig.5.28 (a) EELS curves from line scan experiments at the Al L2,3 edge and the Cu M2,3 edge (2-dimensional curves are in the in-set). (b) is the DF image where the measurement was performed.

***In-situ* heating**

The results have shown that the interlayer has a broad chemical concentration with distorted HCP lattice structure. To determine its thermal stabilities, *in-situ* heating experiments were performed in the ARM at $\sim 600^{\circ}\text{C}$. The heating rate is 20°C per second and the heating time is around 1 second

after the final temperature of 600°C is reached. HRTEM images were immediately captured in the ARM after heating. The sample was then transferred to a CTEM and microdiffraction experiments were performed. The experiment in HRTEM revealed that the HCP phase disappeared during rapid annealing, and another equilibrium intermetallic phase formed, it is CuAl_2 in different orientations. Some Cu layers were still at the top of the film and Al layers between substrate and the newly formed intermetallic phase. Respective BF and HRTEM images are displayed in Fig.5.29 ~ 32.

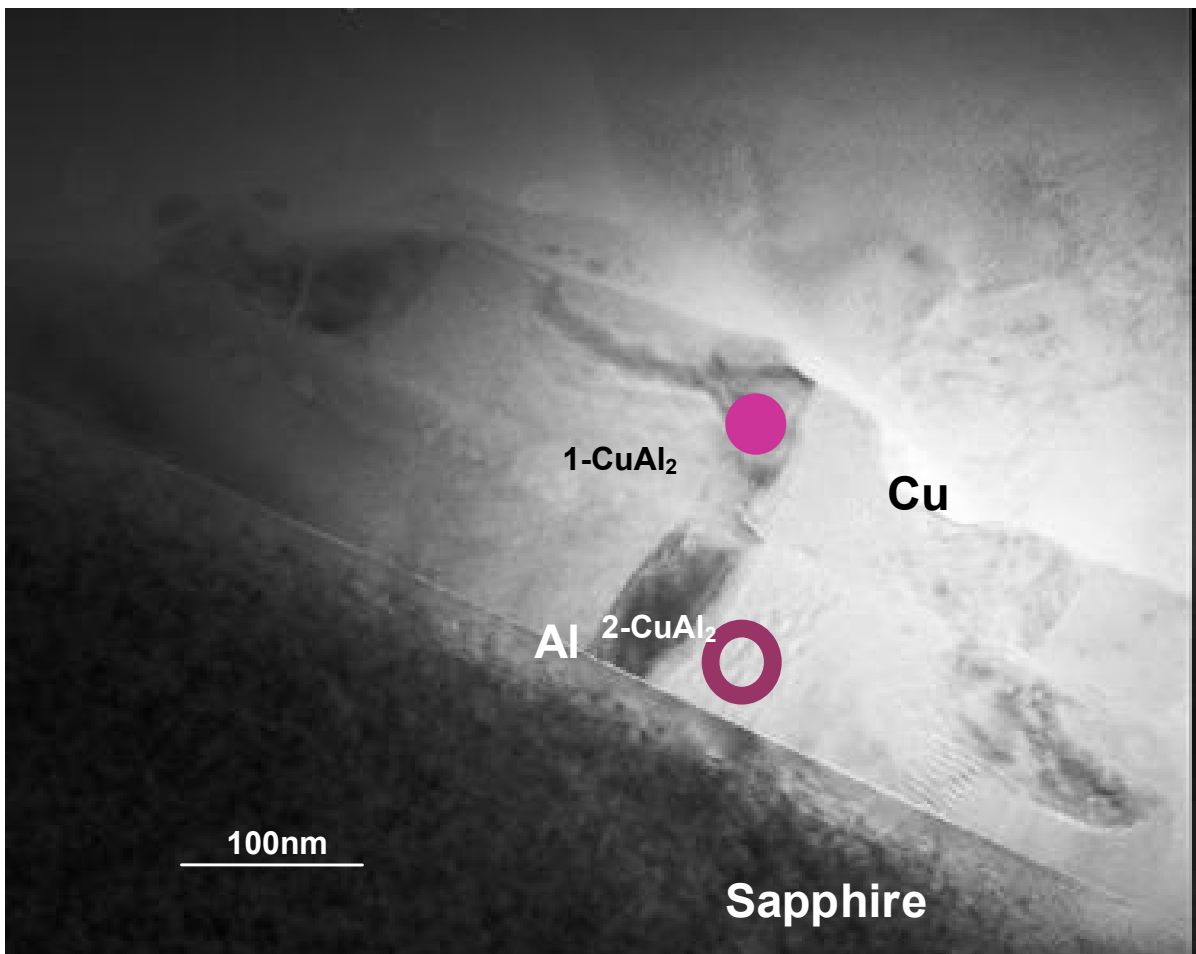
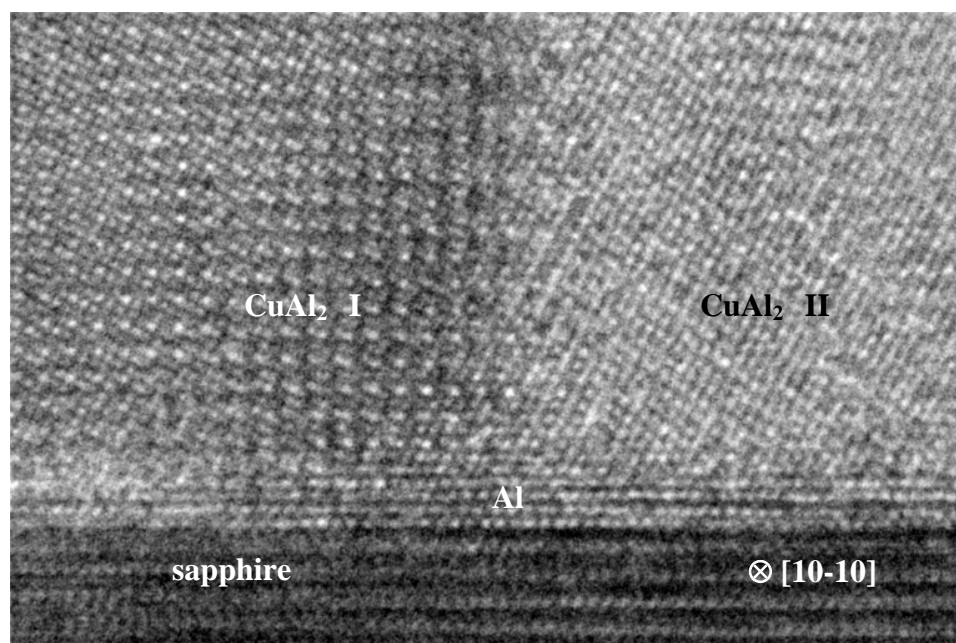


Fig.5.29 BF of the bilayer film after annealing at 600°C for 1 second.



5.30 HRTEM image of the Al layer, which is present between the substrate and two CuAl₂ grains with different orientations.

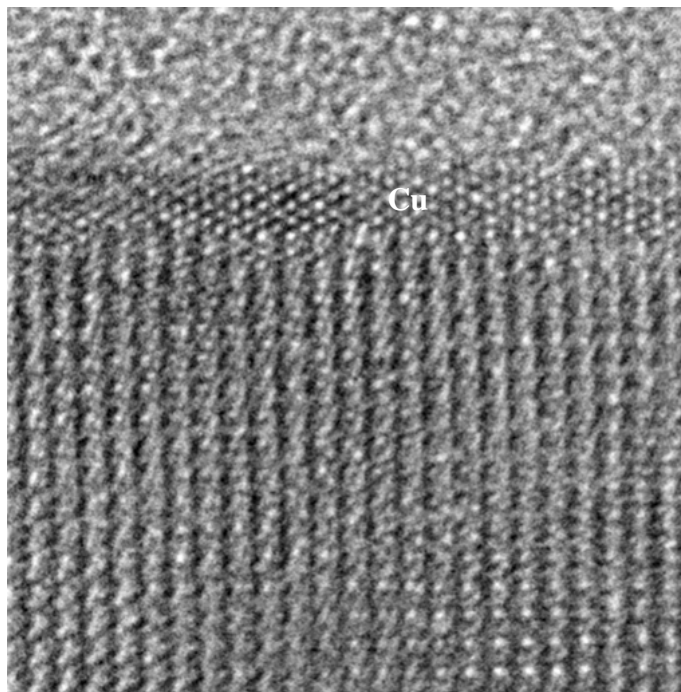


Fig.5.31 HRTEM image of a Cu layer, which is on the top of the whole film and adjacent to the CuAl₂ phase.

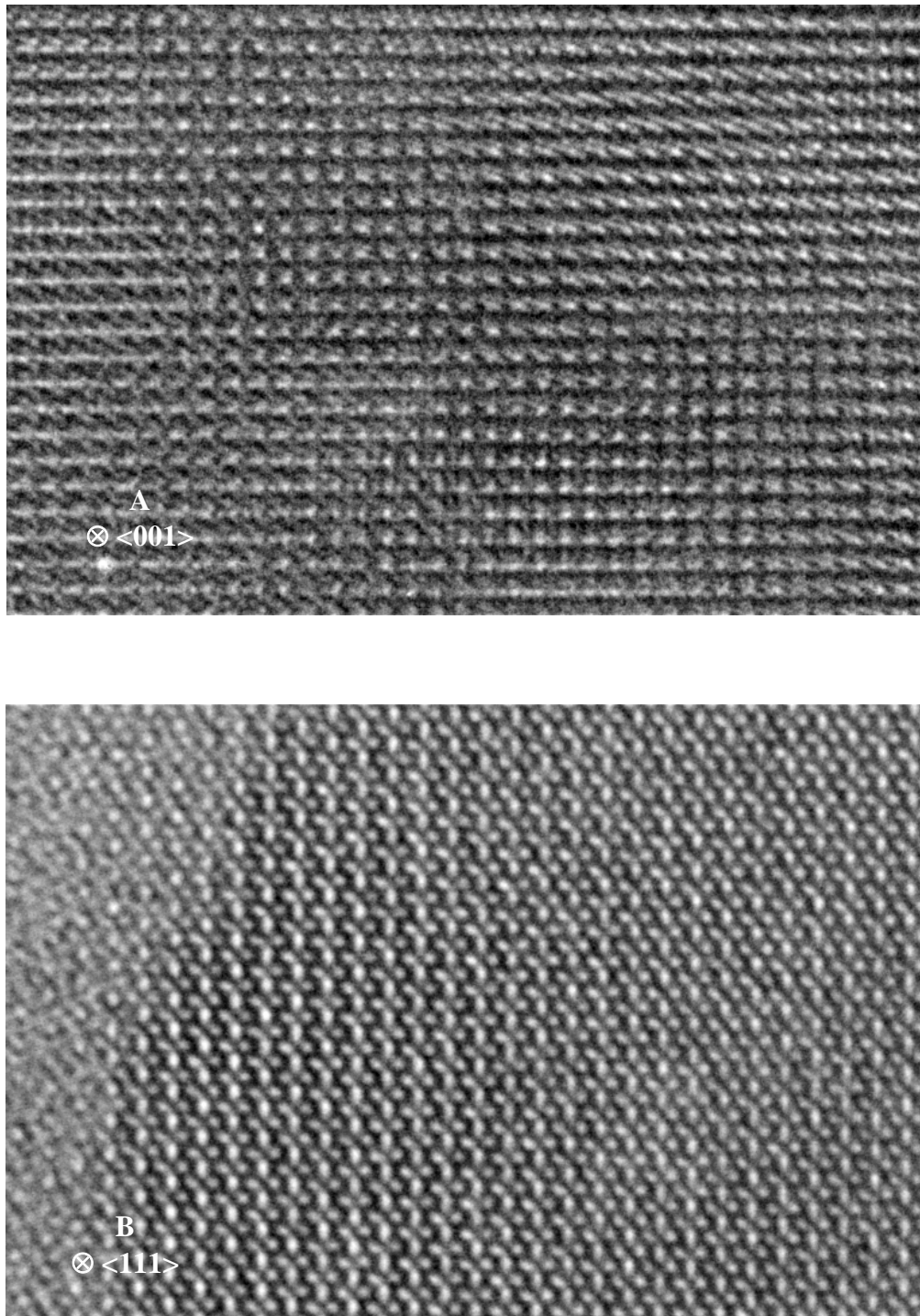


Fig.5.32 Two CuAl_2 grains with different orientations, both of them were taken in $[10\bar{1}0]$ direction of sapphire.

By microdiffraction in CTEM, it is revealed that CuAl and Cu₉Al₄ also existed besides CuAl₂. The BF and microdiffraction patterns are displayed in Fig.5.33 to 35. This indicates that the HCP intermetallic phase is metastable, and it will transfer to three different intermetallic phases, i.e. CuAl, CuAl₂ and Cu₉Al₄ after heating to 600 °C

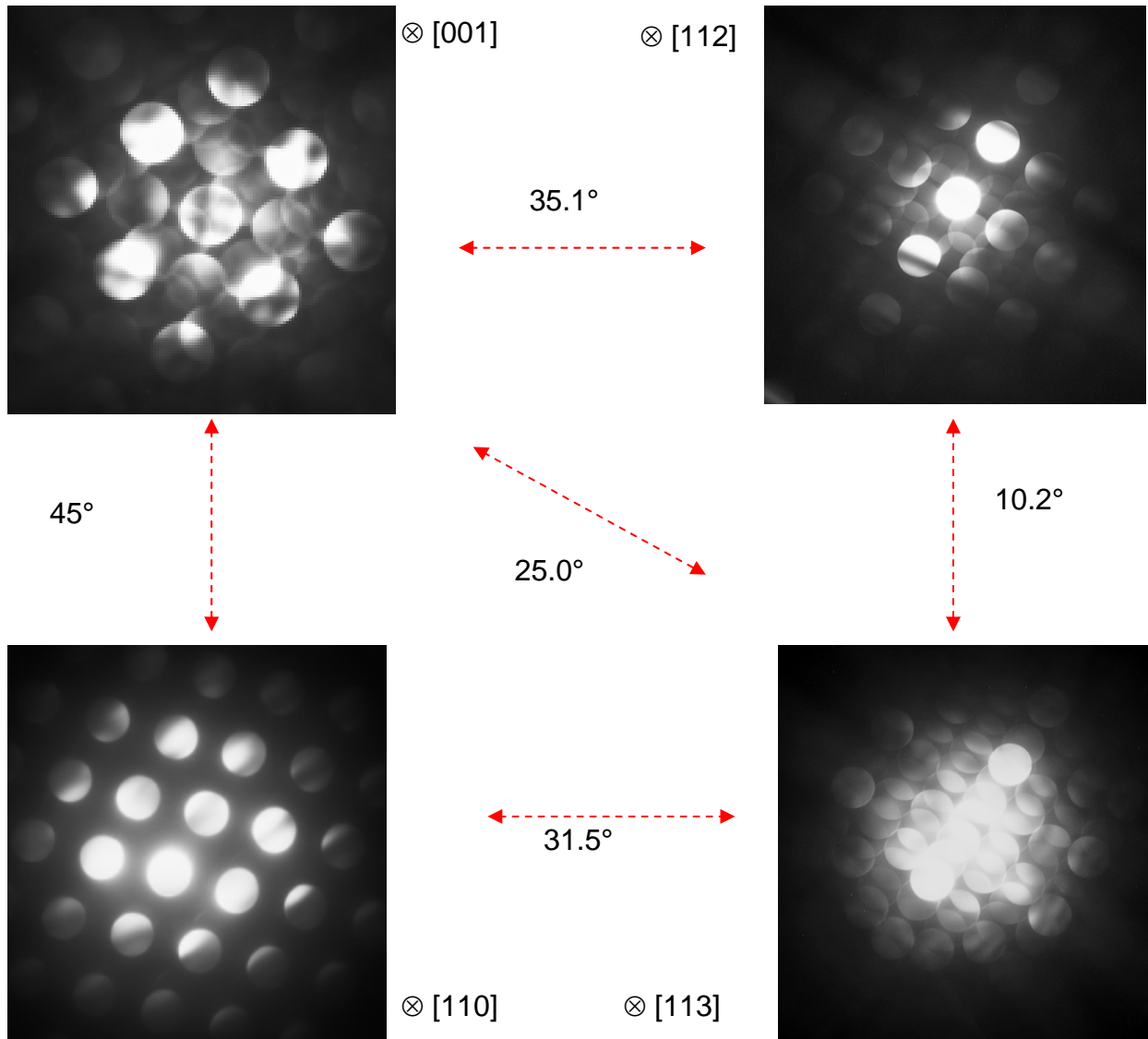


Fig.5.33 Microdiffraction patterns of Cu₉Al₄. They are from four different viewing directions. The tilt angles have been marked out.

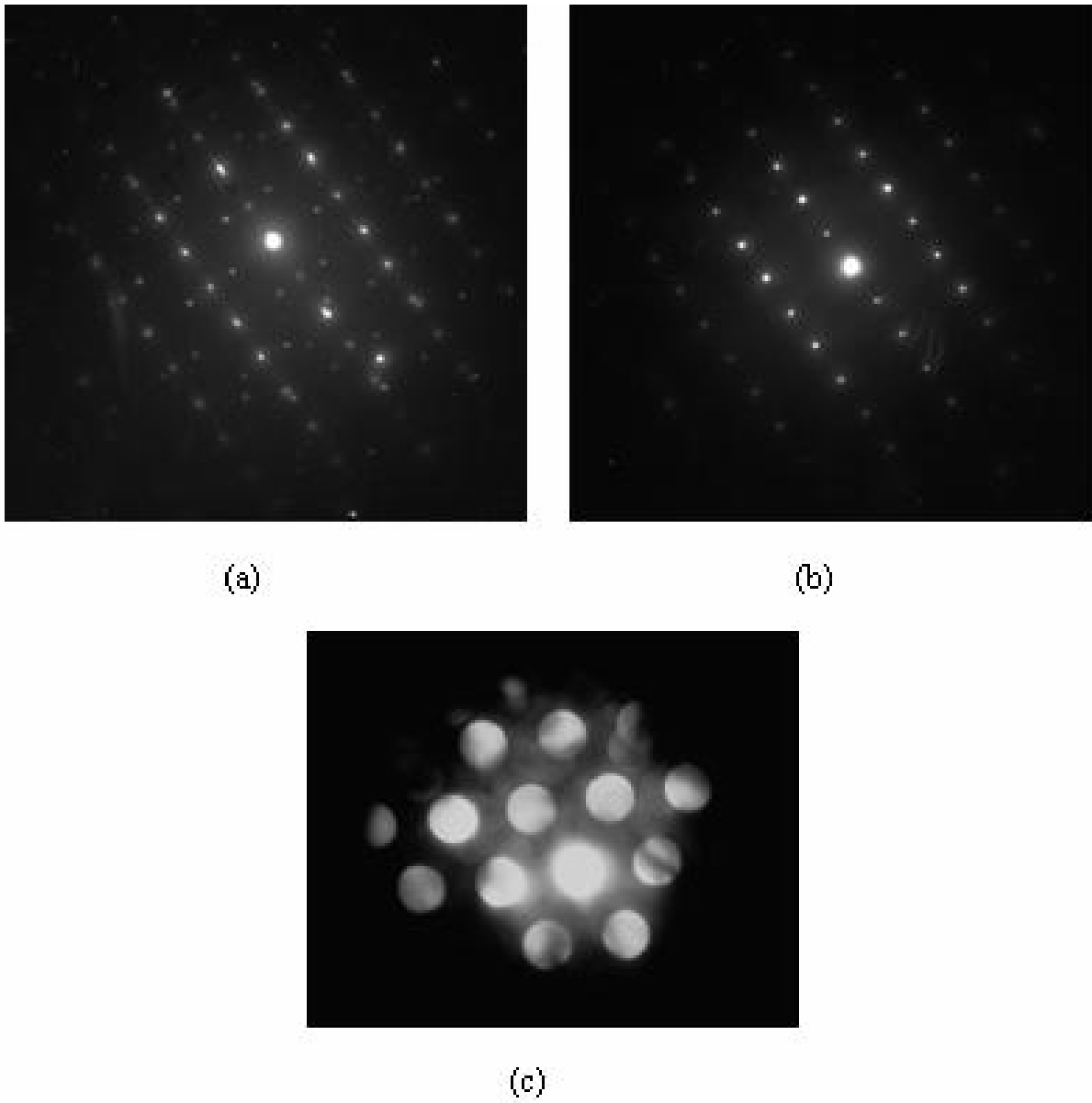


Fig.5.34 (a) SAD of both substrate and CuAl, (b) SAD of the substrate, and (c) microdiffraction pattern of CuAl .

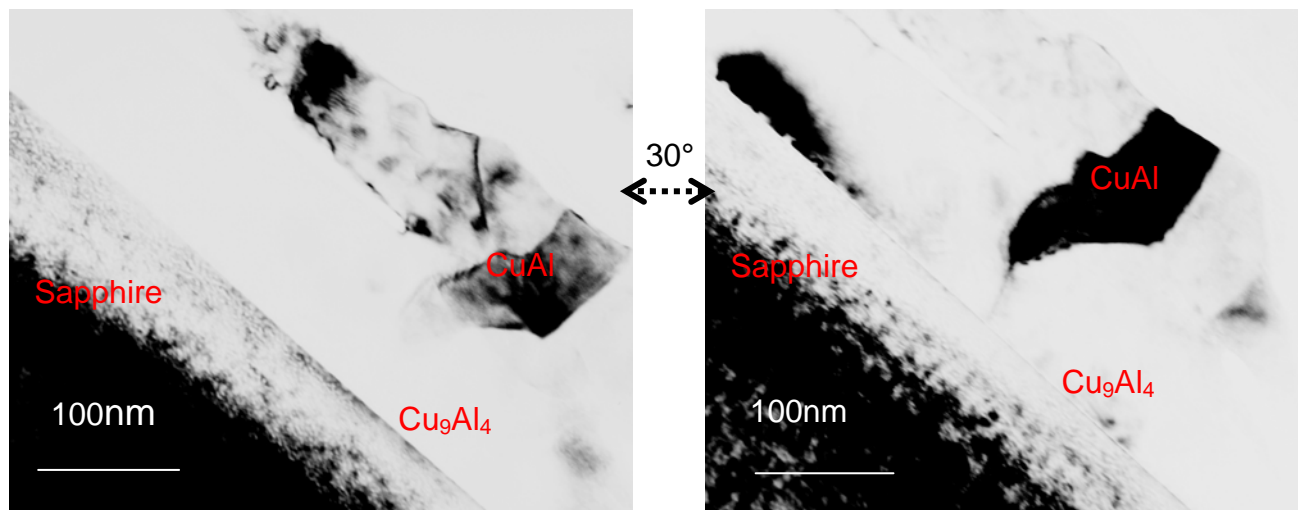


Fig.5.35 Bright field images of the CuAl and Cu₉Al₄ grains. The view directions are [10-10] and [2-1-10] of sapphire.

However, whether 600°C is the lowest transformation temperature is still a question. In other words, the temperature up to which the metastable HCP phase will exist is still an open question. So, additional annealing experiments at various temperatures have been carried out for the Cu-Al bilayer films with the same deposition conditions. After deposition, the films were cut into four pieces and sealed into quartz tubes under vacuum, and then they were annealed in a normal oven at 120, 160, 200 and 240°C, respectively. After this, XRD experiments were performed. They revealed that CuAl was the intermetallic phase formed firstly when the annealing temperature was at or higher than 160°C, as Fig.5.36~37 shows. These three XRD plots also reveal that the intensity of the CuAl peak increases with increasing annealing temperature. This fact indicates that the content of CuAl increases with temperature, and that the Cu-Al bilayer film will transform completely to CuAl at 240°C, as shown in Fig.5.37 demonstrated. When the annealing temperature is lower than 160°C, the XRD profile only shows the peaks from Cu, Al and the substrate (Fig. 5.36). That means the HCP intermetallic phase still can be stable when the temperature is as high as 120°C.

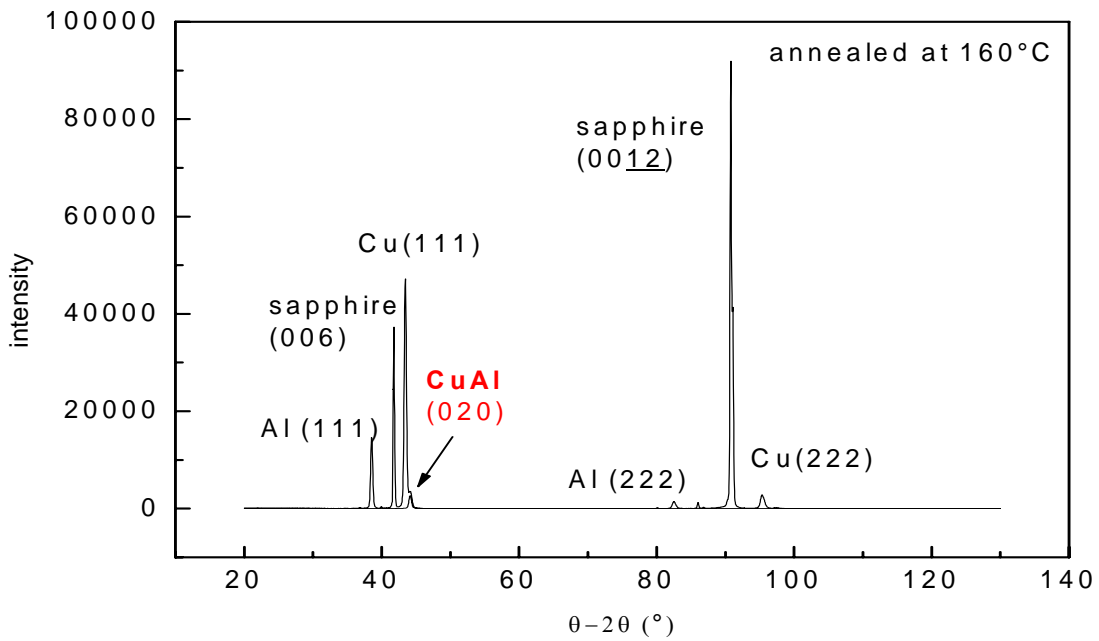
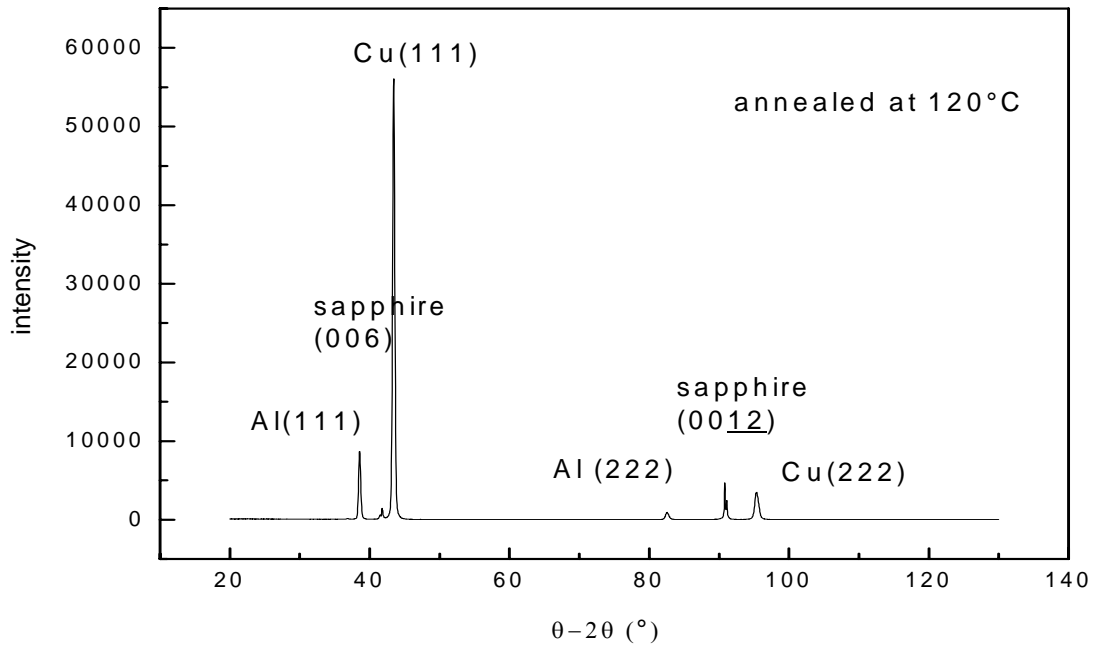


Fig.5.36 XRD of Cu-Al bilayer films annealed at 120°C (the upper) and 160°C (the lower).

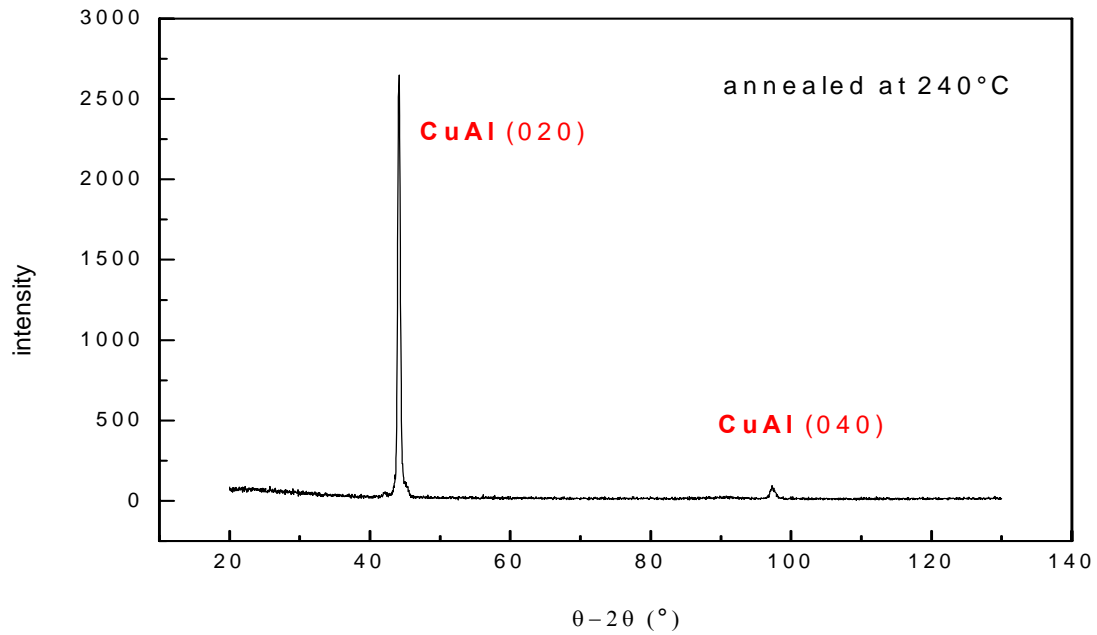
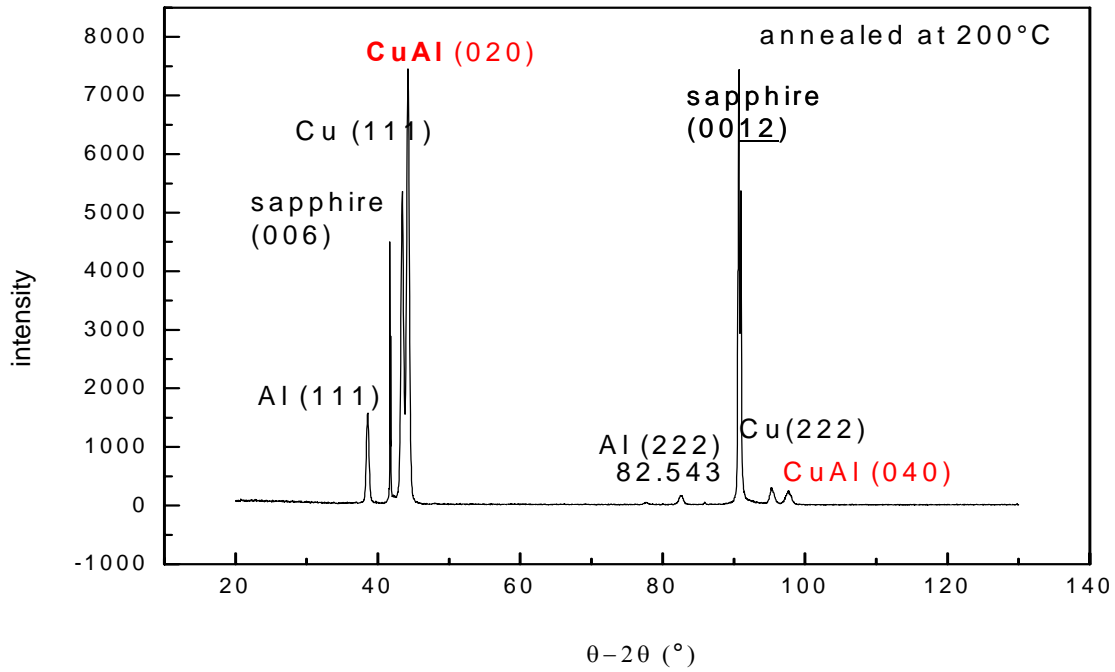


Fig.5.36 XRD of Cu-Al bilayer films annealed at 200°C (the upper) and 240°C (the lower).

Chapter 6

Discussion

In the first part of this chapter, the formation, morphology, crystal structure, chemical composition and thermo-stability of the interlayer between the Cu and Al film will be discussed. In addition, a formation mechanism of the interlayer will be described in the second part of the chapter. At the end of each part, results from the literature will be discussed and compared to the present results.

6.1 The formation and characteristics of the interlayer

In the following, the formation of the interlayer will be analyzed, and then the features of the interlayer, such as atomic structure, chemical composition, and thermodynamic stability will be discussed.

6.1.1 Formation of the interlayer between Cu and Al layers

An intermetallic interlayer with 8 nm thickness was observed between Cu and Al layers in HRTEM investigations, while no corresponding peaks were detected in XRD. The different results obtained by XRD and TEM experiments, for the same MBE film sample, indicate that the whole fraction of the interlayer is either so low that it is below the XRD detection limit or that the interlayer has just been formed during TEM sample preparation but not during film deposition. These points will be discussed in the following.

The detection limits for thin interlayers during XRD experiments strongly depend on the atomic number, beam intensity, in-plane texture (for films) and other factors. For the equipment employed in the present experiments, the detection limit is around 10 nm. For the investigated Cu-Al system, it is likely that the 8 nm thick layer results in an intensity which is too low to be detected. In addition, a small volume fraction usually leads to a broadening of the X-ray peaks which then might not be distinguishable from the background noise.

Since the interlayer connects Al and Cu and a 10% lattice mismatch between these two pure metal layers exists, the lattice of the interlayer will be expanded from the near-Cu side to the near-Al side (as revealed by HRTEM, Fig. 5.18). This leads to a wide range of d values, and thus θ values. It also enhances the possibility for a broad peak, and thus the information from the interlayer might not be detectable by XRD.

In the present study, the films were deposited at RT and no further annealing was performed after film processing. All of the experiments, except the heating experiments, were also performed at RT. Only during TEM sample preparation the specimen could be heated. However, as described in chapter 4, specific specimen preparation techniques were applied to reduce or prevent sample heating. Some of the TEM samples were embedded into polycrystalline Al_2O_3 tubes with glue without any heating, while others were fixed by Ti holders without any glue and also without heating. During the ion-milling procedure a liquid N_2 cooling stage was applied to reduce heating. In addition, the energy of the incident ion beam was 4.5 keV, and the ion-milling was performed from one direction only with an unfocused beam. Using these parameters, the heat generation during the ion milling procedure is minimized. In conclusion, it is believed that the TEM samples were prepared at or even lower than RT, and thus the bilayer films with an interlayer were not changed during TEM sample preparation.

XRR measurements were performed after film deposition at RT without further sample treatment. They reveal an interlayer thickness of around 8 nm which is similar to the value determined by HRTEM. Thus, they confirm that the interlayer forms during film deposition at RT.

In summary, after evaluating the applied methods, it is believed that the interlayer located between Cu and Al layers forms at RT during film deposition, and is not produced by TEM sample preparation.

6.1.2 The morphology, atomic structure and chemical concentration of the interlayer

In section 6.1.1, it was concluded that an interlayer forms between Cu and Al layers at RT. In this part, the morphology, the atomic structure and the chemical concentration of the interlayer will be discussed.

Morphology

In the present work, CTEM was employed to investigate the morphology of the interlayer. It was found that the average thickness is around 10 nm and that the two interfaces (Al/interlayer and the interlayer/Cu) are not flat. This roughness might stem from the roughness of the Al layer which was found experimentally by investigating the surface of an Al film with 100 nm thickness (see chapter 5).

XRR was also used to determine the thickness and/or roughness of the interlayer. The fitting for the XRR experimental data revealed that the roughness of the interlayer/Al interface (1.52 nm) is higher than that of the interlayer/Cu interface (0.74 nm) (see Fig.5.16). The thickness of the interlayer was estimated to be around 7.6 ± 0.2 nm including the interface roughnesses. Thus, the XRR measurements support the TEM findings.

Atomic structure

The atomic structure and chemical concentration of the interlayer were determined in the present work by various TEM methods such as quantitative HRTEM, EDS and EELS. These results will be discussed in the following part.

The information about the structure of the interlayer can be summarized as follows: the interlayer has a HCP stacking order (Fig. 5.18); the lattice parameters determined by quantitative HRTEM assuming a HCP structure are different from any values reported in literature; the XCFs of the HCP model are as high as 93.4% and 93.1% in $\langle 110 \rangle_{\text{FCC}}$ and $\langle 112 \rangle_{\text{FCC}}$ viewing directions (Fig. 5.22); the results from LADIA (Fig. 5.24) indicate that the HCP structure is expanding from the near-Cu side to the near-Al side, and the interlayer is an intermetallic layer with distorted HCP structure.

To exclude the possibility that the interlayer can be described by other high symmetrical structure models, additional image simulations were performed. The corresponding results will be compared to that of the HCP model.

The simulations were carried out using orthorhombic, tetragonal, and cubic models. As an example, the result using the orthorhombic model is displayed in Fig. 6.1. The quantitative agreement between the simulated and the experimental image for this model (XCF is 72.3%) is much lower than for the HCP model (XCF is higher than 93 %). Therefore, the orthorhombic model can be excluded.

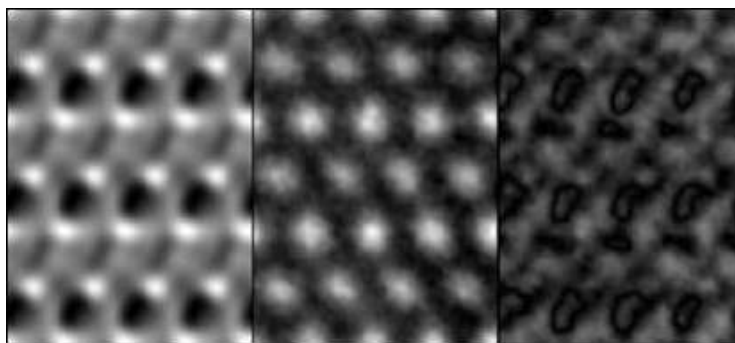


Fig.6.1 Simulated HRTEM image (left) calculated by using an orthorhombic atomic model in comparison to the experimental image of the interlayer (middle) and difference image (right). The viewing direction is $[110]$ of the based films. The XCF is 72.3%.

In principle, the computer program does not allow a comparison if the number of atoms in the model in the viewing direction is different from the number of features occurring in the experimental image. For the tetragonal model, it was not possible to find an agreement between the simulated and the experimental image in $[112]_{\text{FCC}}$ direction since there was no qualitative agreement between the experimental and any simulated images. Therefore, the tetragonal model cannot be used to describe the interlayer structure.

As to the cubic structure model, it might be suitable to get good agreements with both experimental images, however, the tilt angle between the two zone axes of the simulated images will

not correspond to the experimental determined angle of 30° . Thus, the cubic structure model can be excluded.

In principle, a monoclinic structure can also be used to describe the interlayer structure. However, the HCP model has a higher space group number, i.e. the HCP model has higher symmetry, and thus the monoclinic model was not used.

Chemical concentration

According to the results from EDS (Fig. 5.27) and EELS (Fig. 5.28) experiments, the chemical concentration versus position curve (Fig. 5.27), which ranges from the Cu layer to the Al layer across the interlayer, is similar to a pure diffusion profile. The distribution of the chemical composition at the interlayer, which is from 27 at % Al to 58 at % Al with 5 ~ 10 % systematical error, is a part of the 'diffusion' curve.

However, when EDS is employed for the detection of the chemical composition of layered or inhomogeneous specimen, the influences from beam broadening, on the concentration profile of the interlayer has to be taken into account. The beam broadening, which is the beam spreading during the penetration in the specimen, depends both on the penetrated thickness and on the penetrated material. The corresponding function is given by Goodhew *et al.* and Doig *et al.* ^{[Goodhew][Doig]}.

For this calculations the thickness t of the specimen and the beam profile are important. For the beam profile, a Gaussians function $g(x)$ was assumed. The full width of half maximum (FWHM) of the incidence beam will change during penetration of the material. As a first approximation, the FWHM of this Gaussian function $g(x)$ was taken as the average value of the incidence beam and the exited beam, as the schematic drawing in Fig. 6.2 illustrates. The convolution of this beam function $g(x)$ with the chemical concentration profile of the specimen will result in a profile, which is revealed by the EDS experiments. In the opposite way, if the broadening beam function $g(x)$ can be removed from the detected profile by deconvolution, the 'real' chemical concentration can be obtained. In the present work, the deconvolution technique was not employed due to the low number of measured points within the interlayer. Instead, in order to investigate the influence from beam broadening on the chemical concentration profile measured by EDS, simplified calculations were performed by

convoluting (a) electron beam functions $g(x)$ possessing different FWHM with (b) different concentration functions $f(x)$. This will be described in the next two parts.

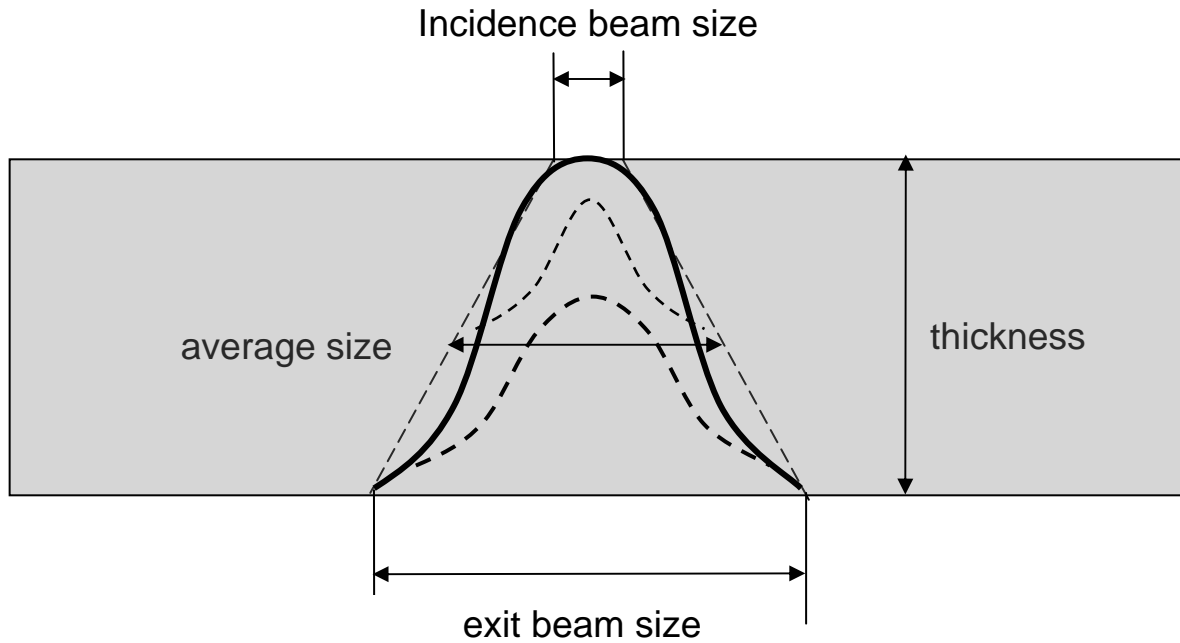


Fig. 6.2 Schematic drawing of beam broadening.

(a) Electron beam functions $g(x)$ with different FWHM

After the beam has penetrating the specimen, it will spread into ^[Goodhew]:

$$B = 0.198 \cdot (Z/E) \cdot (\rho/A)^{1/2} \cdot t^{3/2} \quad (6. 1),$$

with Z = atomic number, A = atomic weight, E is the electron energy in keV, ρ is the density (g/cm^3) and t is the specimen thickness (nm). Fig. 6.3 displays the beam broadening (for a point source) versus thickness curves in Cu and Al foils, which are involved in the present experiments. Since the interlayer consists of both Cu and Al, it is assumed that the range of the beam broadening at the interlayer is between those of Cu and Al.

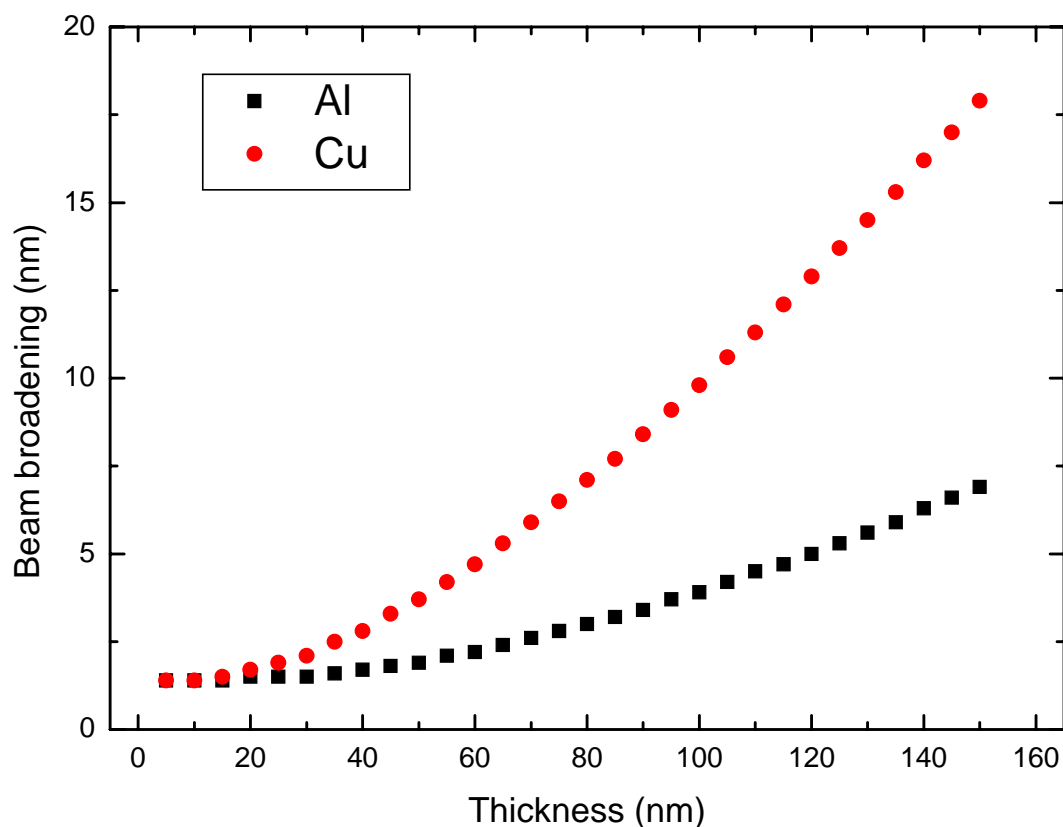


Fig. 6.3 Relationship between thickness and beam broadening in pure Cu and pure Al.

The thickness of the specimen is around 100 ~150 nm (this value was determined by EELS measurements which revealed a thickness of ~ 1.6 times the inelastic mean free path λ (with $\lambda_{\text{Cu}} = 63$ nm, and $\lambda_{\text{Al}} = 100$ nm)). According to Eq. (6.1), the range of the exit beam sizes in Al and in Cu can be obtained. Combining the incident beam size (2 nm in FWHM), average sizes of 2.7 to 8 nm are obtained (in FWHM). Therefore, for the convolution, six different beam sizes were considered, i.e. 0.5 nm, 1.25 nm, 1.5 nm, 2 nm, 2.5 nm and 5 nm in radius (corresponding to σ of the Gaussian functions), as shown in Fig. 6.4. Here, the value of 0.5 nm is chosen as a reference, since it is the smallest incident beam size in radius in the STEM VG 501 UX.

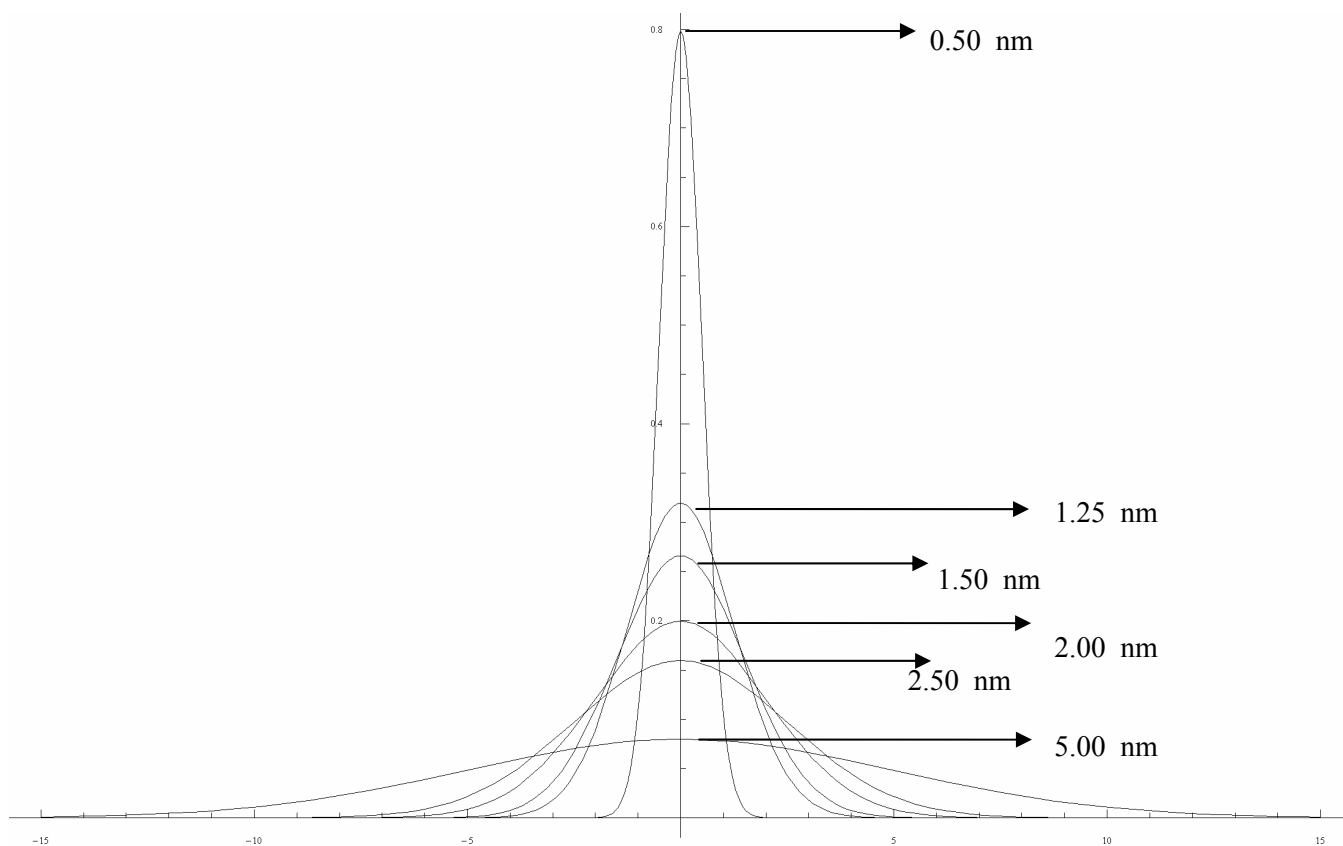


Fig. 6.4 Gaussian functions with various σ values which were used to describe the incident and broadened electron beams.

(b) Different concentration functions $f(x)$

Three models of chemical composition distribution were constructed for the 8 nm wide interlayer. The first model assumes that the interlayer is a pure diffusion layer. The chemical concentration gradient for this model is approximated by a linear decreasing function (see Fig. 6.5) from the pure Al to the pure Cu side. In the second model, the Al concentration is 45 at % Al at the Al/interlayer interface and then linear decreasing to 32 at% Al at the interlayer/Cu interface (Fig. 6.6). In the third model (see Fig. 6.7) a constant chemical concentration (e.g. the average value of the second model, 38 at % Al) of the interlayer is considered*.

* These chemical concentration ranges are designed according to the Hume-Rothery laws and will be discussed in detail in section 6.2.2.

As a first approximation, the model concentration functions $f(x)$ were convoluted with the electron beam function $g(x)$ according to:

$$(f * g)(x) = \int_{-\infty}^{+\infty} f(y) \cdot g(x - y) dy \quad (6.2).$$

As described above, the concentration function $f(x)$ was approximated by three models and for the electron beam function $g(x)$ a Gaussian function was used.

The possible 'measured' concentration profiles obtained by convoluting the Al distribution models with the Gaussian beam profiles (possessing defined σ values) are displayed in Fig. 6.5 to Fig. 6.7. The calculations revealed that the chemical concentration profiles are smeared out with increasing beam size. Fig. 6.5 shows that the steep diffusion curve is flattened with increasing beam size. Fig. 6.6 and Fig. 6.7 also reveal that the step and inclined step functions are fading out if a large beam is used. The characteristic of a step or inclined step function disappear for a beam radius larger than 2.0 nm. Nevertheless, compared to the experimental curves, the best agreement occurs for the calculated curves obtained by using broadened beams of 5 nm and the second and/or third model. They reveal a chemical composition range for the interlayer from 41 to 63 at% Al, which is only slightly steeper and wider than the experimental one (27~ 58 at % Al). In contrast, the pure diffusion model results in a much larger chemical range (25 ~ 74 at % Al) with the same beam size. This is not found experimentally. These results suggest that the second and/or third models can describe the experimentally observed chemical concentration features better, although diffusion also exists along the layered films.

As described above, the calculations revealed that the chemical concentration profiles are smeared out with increasing beam size. The calculated curves for a 2.5 nm or 5.0 nm beam size show a similar behaviour as the 'diffusion' model displayed in Fig. 6.5. Independent on the broadened beam size (which is larger than the smallest incident beam size of 0.5 nm), if the measured step length is larger than 2.0 nm in the 8 nm thick interlayer and thus only three or less points are measured in that region, the curvature of the concentration-position curves at the interlayer would not be revealed. This can be estimated from both Fig. 6.6 and 6.7, which correspond to the second and third model.

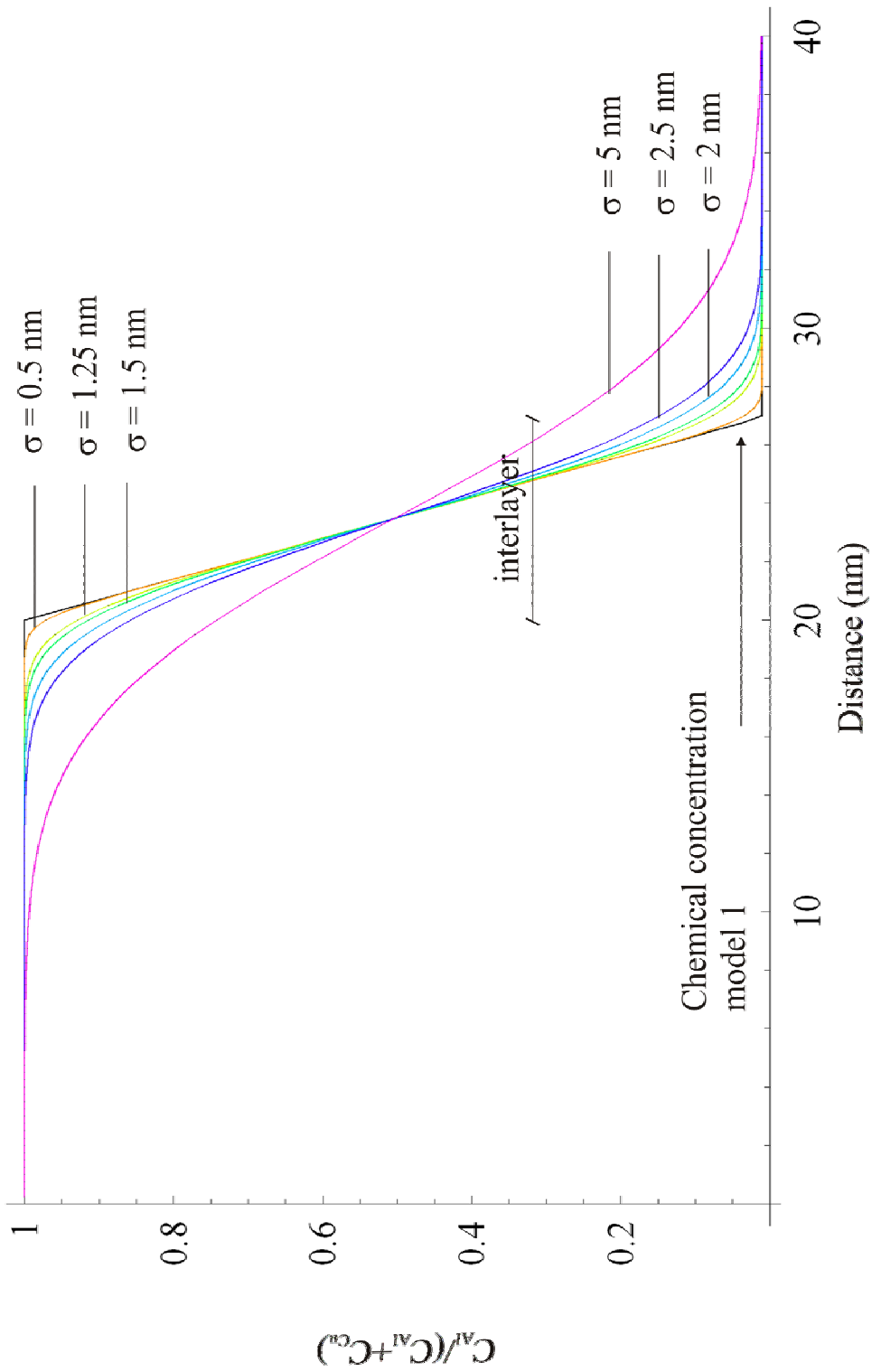


Fig.6.5 Calculated concentration profiles using different beam sizes and the corresponding linear decreasing concentration model.

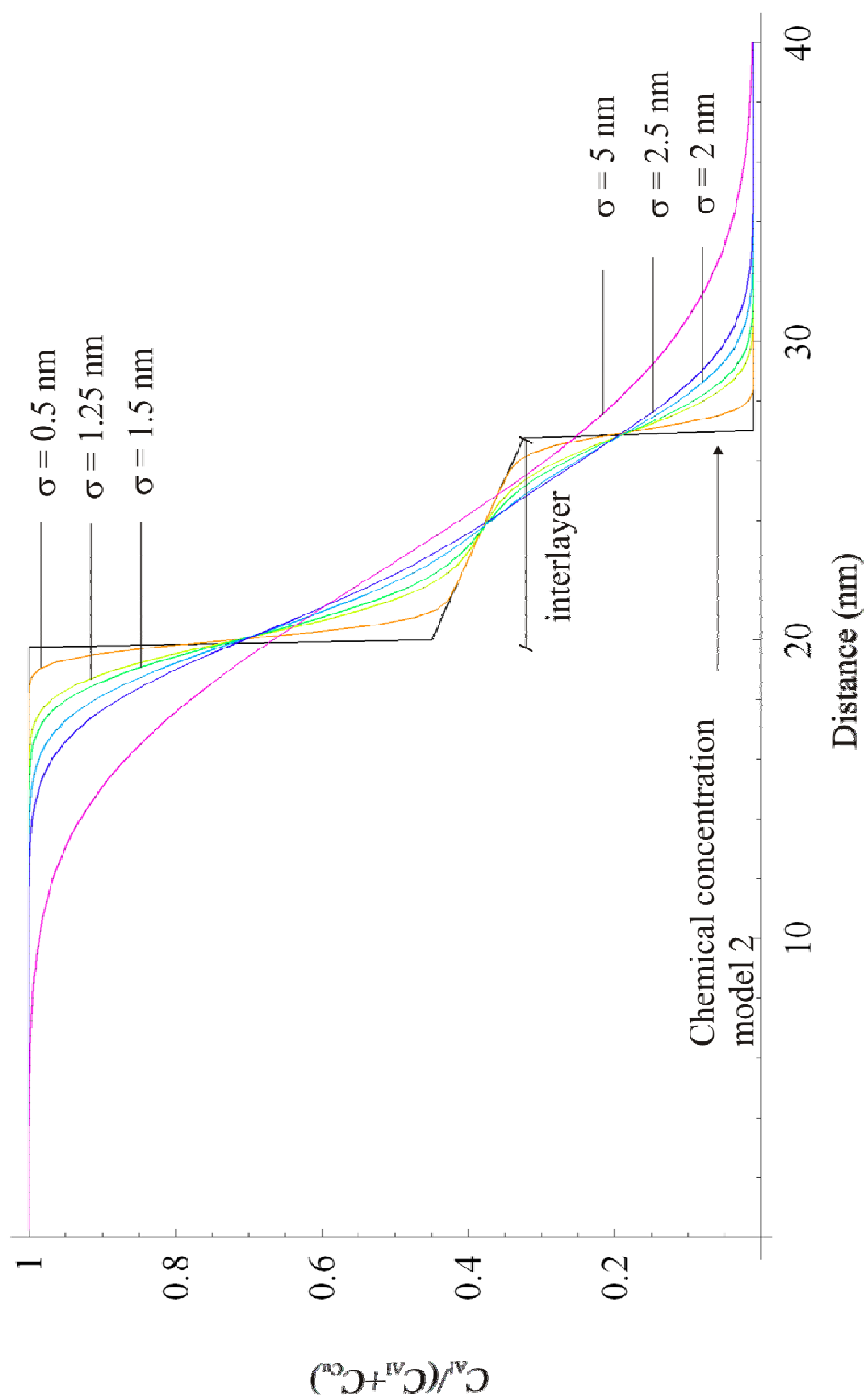


Fig. 6.6 Model calculation profile (black line) and corresponding calculated profiles using various beam sizes.

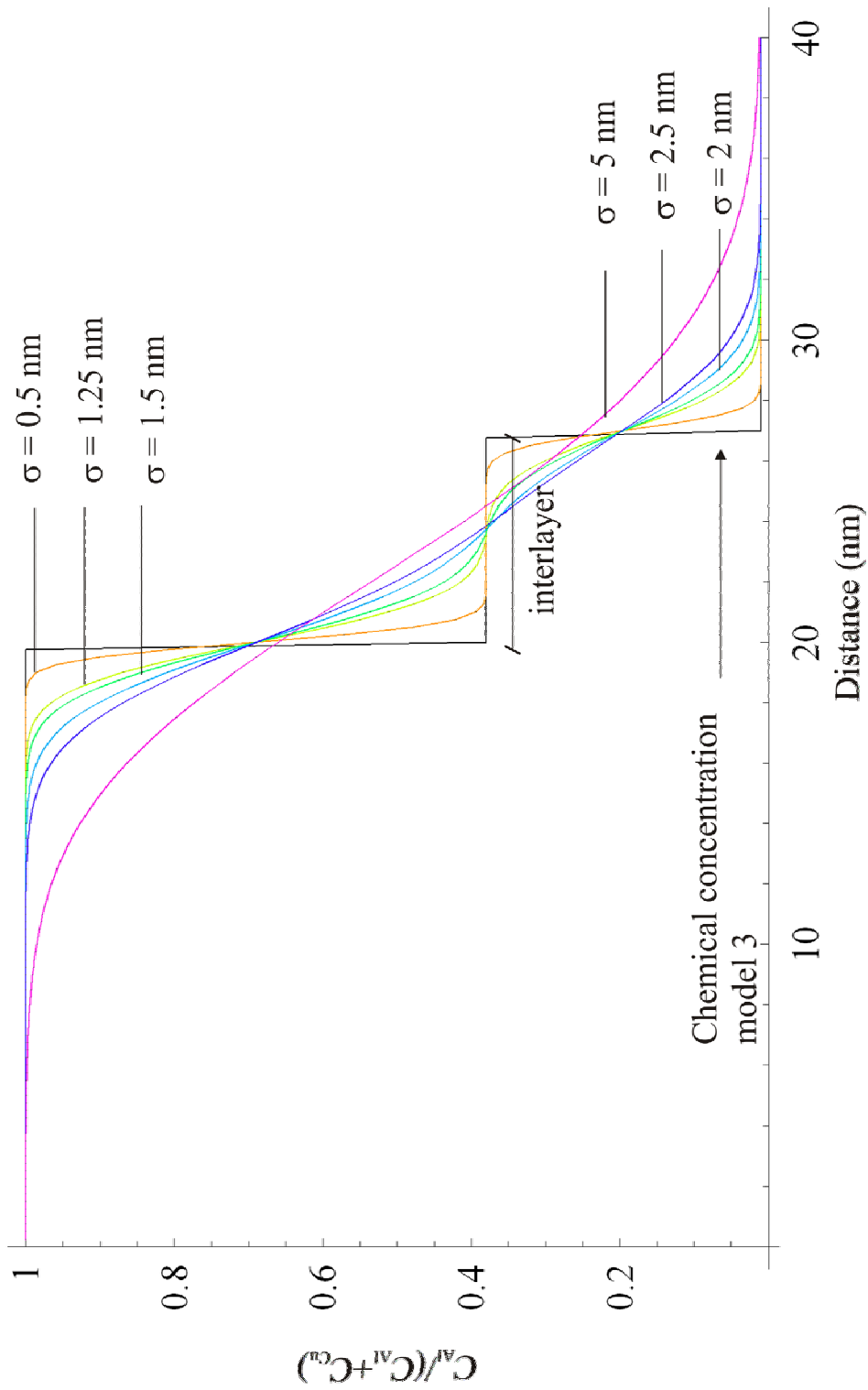


Fig. 6.7 Calculated concentration profiles using different beam sizes and a step-function for the 'real' concentration profile.

Combining Fig. 6.3 with the series of the chemical concentration curves influenced by the beam size, the maximum thickness and beam broadening can be estimated for which the 'real' concentration profile can be measured. If the specimen is thinner than 20 nm, the exit beam size is smaller than 2 nm for the Cu layer. For this case, it should be possible to detect the characteristics of the concentration-position curves by EDS measurements. If the TEM specimen is thicker than 20 nm, the penetrating beam will be spread more than 2 nm, and then the detailed characteristics in the chemical concentration can hardly be revealed in the experimental data.

In the present work, the thickness of the specimen is around 100 ~ 150 nm, for this thickness, the beam broadening is 9 ~ 18 nm in diameter for the pure Cu layer and 4 ~ 6 nm in the pure Al layer. At the same time, the step length in the linescan experiments was as large as 2.5 nm in the 8 nm wide interlayer. For the large broadened beam and a few numbers of detected points at the interlayer, the chemical concentration features can not be revealed in detail, and thus the EDS linescan measurements just give diffusion-like curves for the HCP phase locating between the Cu and Al layers.

In conclusion, the chemical composition profile of the interlayer was not determined in detail via EDS measurements due to beam broadening. However, the calculations suggest that the chemical concentration features at the interlayer agree with the models which are in accordance to Hume-Rothery laws (model 2 and 3). Although the experimental accuracy is limited in spatial resolution owing to beam broadening, the chemical concentration values of the interlayer are still reliable.

In order to determine whether the second or the third model is more suitable to describe the chemical concentration distribution at the interlayer, additional HRTEM image simulations were performed to evaluate the chemical composition of the interlayer as a function of the position. For these simulations, the lattice parameters of the model described in chapter 5 and the same imaging conditions (e.g. focus value, thickness, tilt angle) were used, but the chemical concentration was varied.

The simulation steps were as follows: at the positions for Cu atoms the occupancy was varied from 0 % (pure Al) x 100 % (pure Cu), and thus the relative Cu concentration changed

from 0 % to 50 % according to the atomic model. Then the Cu atoms were kept at their positions but the Al sites were gradually occupied by Cu. In this way, the relative Cu concentration was continuously increased to 100 %. After changing the chemical concentration, simulations were performed for the modified atomic models. Fig.6.8 shows the XCF as a function of the Cu concentration. As Fig. 6.8 illustrates, the original atomic model (50 % Cu and 50 % Al, Fig. 5.22) has the highest XCF in $[110]_{\text{FCC}}$ viewing direction, but in $[112]_{\text{FCC}}$ viewing direction, the best fitting model changes to the one with 40 % Cu and 60 % Al. However, the two experimental images taken in different viewing directions are acquired at different TEM cross-section samples stemming from the same MBE film sample. It is not possible to ensure that these two areas with a size of $(1.2 \times 0.8) \text{ nm}^2$ in the HRTEM images are from areas which have the same distance to the Cu/interlayer or to the Al/interlayer interface. It is more likely that the images were taken at regions which are differently located relative to the interfaces and which possess different chemical compositions. While the experimental images in $[110]$ direction is more likely acquired at the middle of the interlayer; the simulations for the image taken in $[112]$ direction indicate that it stems from an area close to the Al/HCP interface due to the high Al concentration. This explains why for the different viewing direction the highest XCF was obtained for different chemical compositions.

The simulation results suggest that in the interlayer, different areas have various chemical compositions. Thus the chemical concentration is not constant but changes within different regions. Therefore, the second model for the chemical concentration distribution of the interlayer should be the one closest to the real situation.

The above results can be summarized as follows: the roughness of the interlayer/Al interface exceeds that of the interlayer/Cu interface; the interlayer consists of an intermetallic layer which is $\sim 8 \text{ nm}$ thick and has a distorted HCP structure; the interlayer is neither a layer with constant chemical composition nor a pure diffusion layer, but it has a broad chemical composition, ranging from 27 to 58 at. % Al; the Al content increases from the Cu/interlayer to the Al/interlayer interface. This range of the chemical composition values will be further discussed in the section 6.2.1.

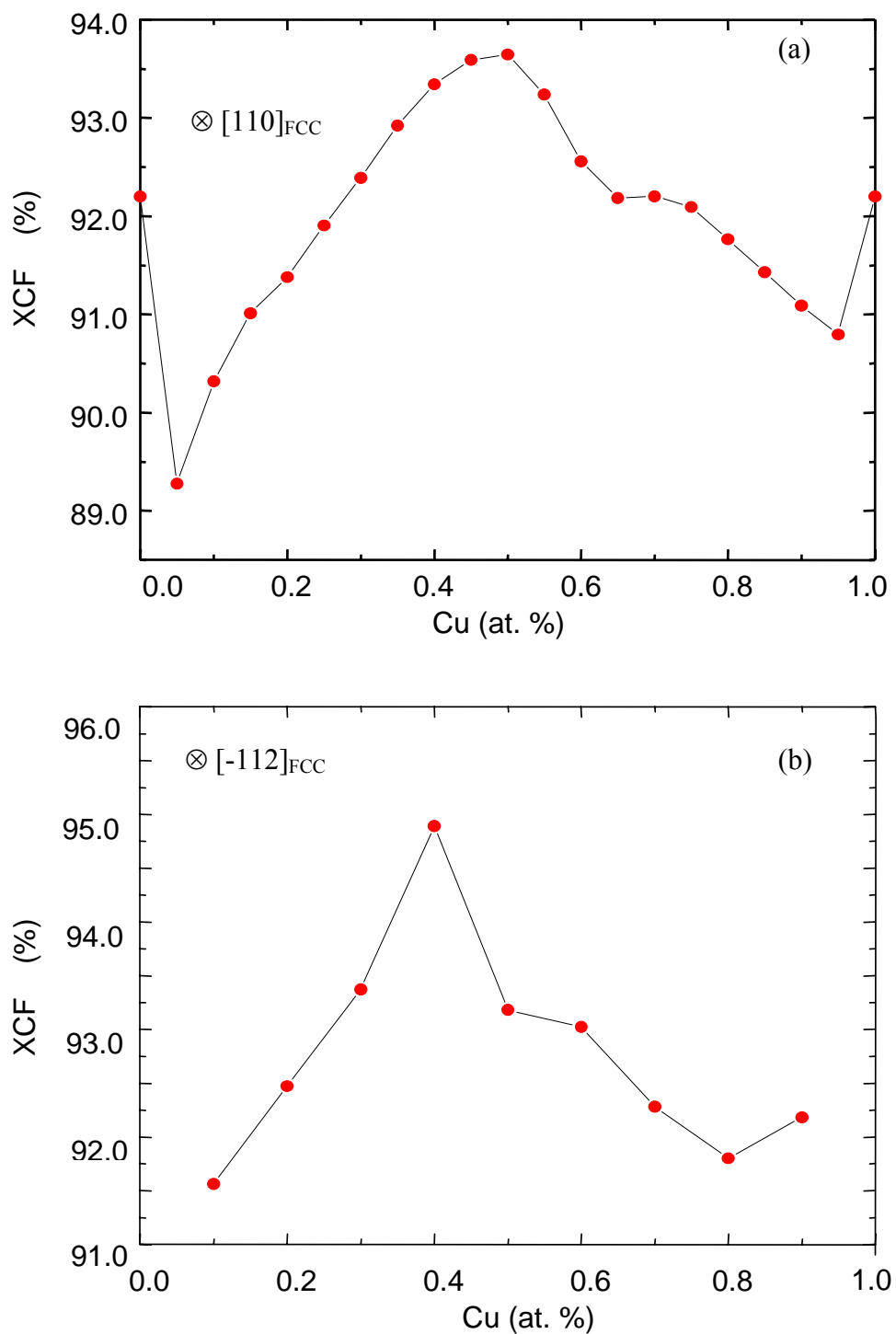


Fig. 6.8 Relationship between the chemical composition and the XCF (the agreement of simulation). (a) is for the $[110]_{\text{FCC}}$ viewing direction, the step size for changes in the chemical concentration is 5%, the open circle is for the model in which Cu and Al atoms exchange positions. (b) is for the $[-112]_{\text{FCC}}$ viewing direction with changes of 10 % in chemical concentration.

6.1.3 Thermal stability of the HCP phase

In-situ HRTEM heating experiments were performed at 600°C to investigate the stability of the HCP phase. After cooling the specimen to RT, it is found that all occurring phases are the thermodynamically stable alloy phases (Fig. 5.28 to 33). Their existence agrees with the phase diagram (Fig. 2.6). However, the HCP phase located at the interface between Cu and Al has disappeared. This indicates that the HCP phase is metastable.

The *in-situ* annealing experiments were carried out only at a high temperature of 600°C. In order to find the existence temperature region of the HCP phase, a series of *ex-situ* annealing experiments have been performed at lower temperatures (Fig. 5.34 to 37). XRD measurements were performed at these samples, and for annealing temperatures lower than 120°C the results are the same as for the as-deposited film (Fig. 5.37). However, it should be reminded that XRD is not able to detect the HCP phase due to the limited volume fraction. Therefore, these measurements only indirectly indicate that the metastable HCP Cu-Al alloy phase might be stable between RT and 120°C.

The XRD measurements performed at samples annealed *ex-situ* above 120°C showed the formation of the thermodynamically stable CuAl phase. However, it is unclear whether the metastable HCP can coexist with CuAl or not since the XRD was the only method employed. When the temperature is high enough that CuAl can form, the metastable HCP phase might disappear and transform into CuAl, or they might still occur at the interface.

In conclusion, when the temperature is higher than 600°C, the HCP phase will be decomposed. However, the precise existence temperature range of the HCP phase could not be determined experimentally since no additional TEM measurements were performed.

6.1.4 Comparison of the results to the literature on Cu-Al film systems

In the present study, an interlayer consisting of a HCP metastable intermetallic phase was found. ‘Similar’ results were reported by Chen *et al.* ^[Chen HY] and Vandenberg *et al.* ^[Vandenberg] as will be discussed below.

Chen and his colleagues ^[Chen HY] studied the Cu/Al interface by XRR and EXAFS. After annealing at 65 ~ 200°C, an interlayer existing of various phases was detected in their experiments,

which were described as a ‘multiphased’ layer. However, detailed information about the type of alloy phases formed, the average chemical composition of the ‘multiphased’ layer and the relative volume ratio between these phases were not given. They also did not report any new structure in the Cu-Al system. Though XRR is a useful technique to detect different electron densities, it can not detect crystal structures. In addition, XRR is not very sensitive to distinguish elements having similar electron densities.

In Vandenberg *et al.* [Vandenberg] experiments, a metastable β' -CuAl_x phase was found in a 700nm Cu/Al thin film which was evaporated on an oxidized silicon substrate. It forms at 250°C and has different lattice parameters compared to the known intermetallic phases. β' -CuAl_x has a hexagonal structure, and is a kind of superlattice of cubic FCC-ordered β -Cu₃Al [Vandenberg]. Though the structure of the β' -CuAl_x phase was obtained by grazing incident XRD, the chemical composition of this phase was not determined.

Compared to the present results, the results from Chen *et al.* [Chen HY] did not reveal the chemical composition or exact structure information of the metastable phases. Though Vandenberg *et al.* [Vandenberg] has obtained the atomic structure of the superlattice, the chemical composition for β' -CuAl_x is uncertain. Nevertheless, both the structure and formation temperature of the reported metastable phases are different from those observed in the present work.

Others studies [Simi], [Broeder], [Funamizu], [Hentzell], [Jang], [Fadnis], [Markwitz], [Gershinskii], [Campisano], [Hamm], [Rayne] performed at Cu-Al film systems only concentrated on the behavior (specifically phase formation and diffusion) of the known intermetallic phases at high temperatures. In none of these studies, a metastable HCP phase, as found in the present work, was reported. The reasons for this might be:

(i) Most of the samples were prepared or annealed at temperatures higher than 120°C. Since the HCP phase seems to be stable only at temperatures lower than 120°C (see chapter 6.13), it might be impossible to observe the HCP phase in these samples.

(ii) Some special TEM samples preparation techniques, which can protect the HCP metastable phase from being heated to higher temperatures, were not used. However, normal TEM sample preparations which use a heating process to harden the glue in the embedding procedure will push the metastable HCP phase to transform into other equilibrium alloy phases (CuAl₂, CuAl, Cu₃Al₂, Cu₃₃Al₁₇, Cu₉Al₄, and Cu₄Al).

(iii) The metal-metal interface is rough. In CTEM it is not easy to observe a flat interlayer and distinguish the banded interlayer from rough metal grains. However a large number of studies employed only CTEM techniques [Vandenberg]. Diffraction mode in CTEM is a powerful tool to investigate the structure of materials, but it is not so effective when the volume of the investigated area is too small. HRTEM at an atomic level can overcome this problem and the local structure can be investigated in detail. Until now this technique was rarely used in the Cu-Al system since several kinds of alloy phases exist simultaneously and the rough metal-metal interface makes the analysis more difficult. A few studies used HRTEM, but the investigations were performed at plane-view samples, and not for cross-section samples which can reveal the interface structure. Quantitative HRTEM was not applied to this system so far, though helpful to resolve the unknown atomic structure. In the present study, besides CTEM, HRTEM and quantitative HRTEM are employed, which revealed some interesting and reliable information about the structure and composition of the interlayer.

In summary, modified TEM sample preparation methods and the combination of various TEM techniques are necessary to protect and detect the metastable HCP phase. Without them, it is difficult to observe this phase. This and the fact that other preparation and annealing temperatures were used in previous research studies might explain why the HCP phase was not observed before.

6.2 The formation mechanism of the interlayer with HCP structure

After discussing the formation and characteristics of the HCP intermetallic phase between Cu and Al, the next part will concentrate on the formation mechanism.

6.2.1 The connection between chemical composition and structure of the HCP phase

The interlayer reported in the present work, has so far not been found in the Cu-Al system. The open question is whether the HCP structure and the broad chemical content of the intermetallic phase are related to each other. In bulk alloy material, a similar phenomenon has been explained by Hume-

Rothery laws for electron compounds ^[Cahn]. The same theory will be applied in the following to the interlayer found at the Cu/Al interface.

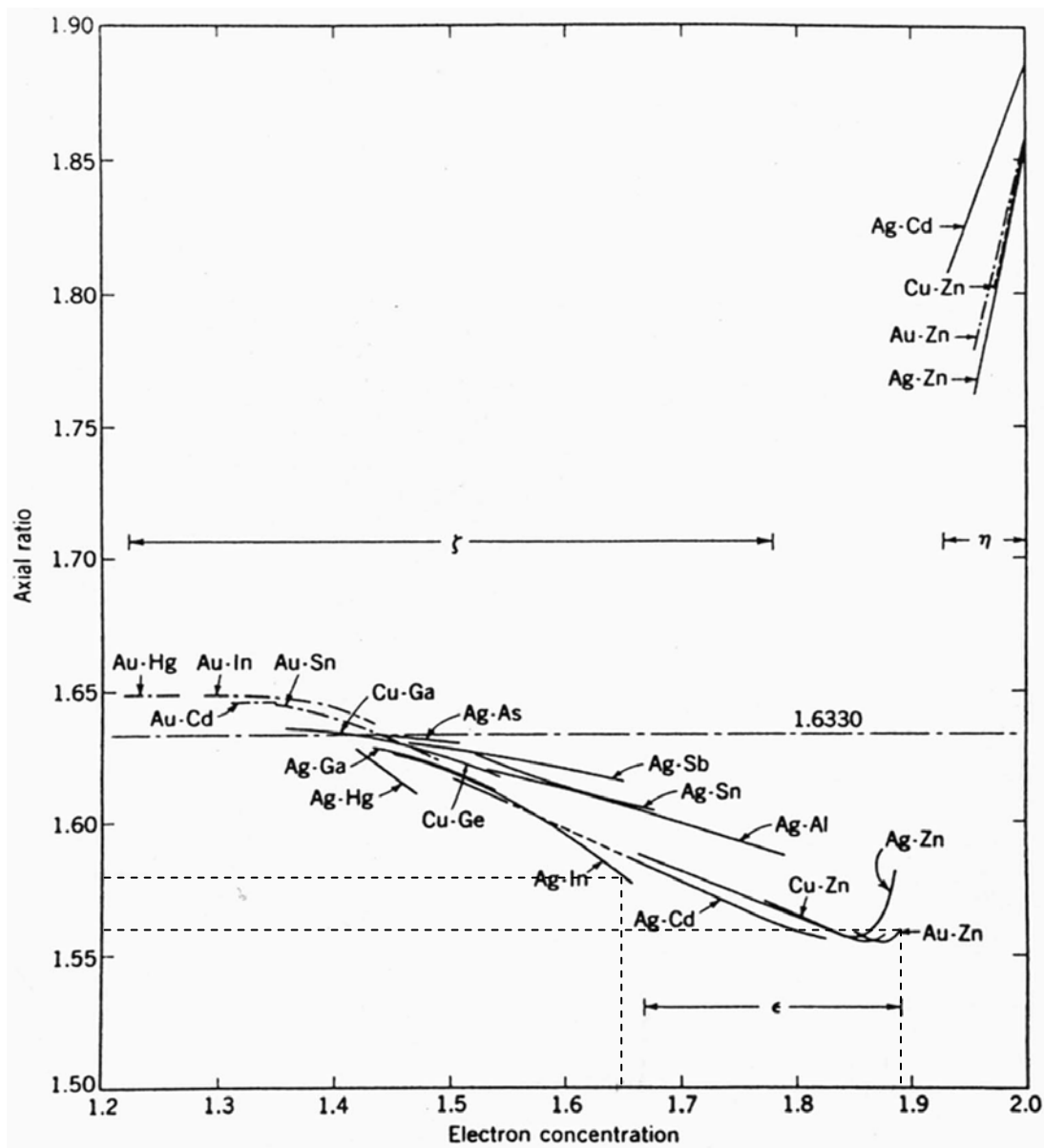


Fig. 6.9. The relationship between the electron concentration and axial ratio in various binary alloy systems with HCP structure ^[Cahn]. The dash lines indicate the range of the c/a ratio from HRTEM experiments and corresponding m range in the Cu-Al system.

According to the Hume-Rothery laws the valence electron density m , is an important parameter connecting the chemical composition and structure via equation (2.5), $m = e_A * x + e_B * (1-x)$ (see chapter 2). The literature provides a series of curves which reveal the relationship between m and c/a (axial ratio, i.e. structure) for various alloy systems. Fig. 6.9 illustrates the m versus c/a relationship in binary alloys with HCP structure ^[Cahn]. Combining the experimental c/a values obtained from HRTEM with these curves, m values can be obtained. Then the chemical composition can be deduced by using equation 2.5 (see also chapter 2).

In the present work, when the noble metal Cu, which has one valence electron per atom and a FCC structure, is ‘alloyed’ with Al, the m will increase from 1 to 3 eventually. The ratio of the relative chemical content decreases from 100 % Cu accordingly to 0 %. When m reaches a critical value, the structure will change from FCC to other crystalline structure types (see chapter 2). In the Cu/Al bilayer film system, the m value of the interface area is changing during deposition due to interdiffusion of Cu and Al. And thus, when the ‘alloy’ process continues, the HCP structure might be more favorable than the FCC structure.

Though Cu-Al alloys have not been included in the curves in Fig.6.9, some information can be obtained following the general trends of the other curves. According to the results from HRTEM, the axial ratio c/a is 1.57-1.58. In Fig. 6.9, the corresponding electron concentration values m are around 1.64 to 1.89. These electron concentration values are inserted into Eq. 2.5, where x is the content of Al with 3 valence electrons per atom, and $(1-x)$ is the content of Cu with 1 valence electron. It leads to a relative content of Al varying between 32 at% to 45 at%, which is in the range of the experimental EDS results (27 ~ 58 at %). This predicted values were used for evaluating the effect of beam broadening (chapter 6.1); the chemical concentration value of the interlayer was set between 32 ~ 45 at % Al in the second model and the average value of this range (38 at% Al) was used in the third model. Combining the results from the beam broadening effects and the Hume-Rothery theory, it is found that the measured chemical concentration range of the interlayer is larger than that of the ‘calculated’ values.

One reason for the difference between the calculated (32 ~ 45 at %) and measured (27 ~ 58 at %) chemical concentration range might be that the HRTEM simulations were done only for limited areas, so the simulated lattice parameters are precise for certain areas but not for the whole interlayer. This might explain why the calculated values for the chemical concentrations have a narrower range

compared to the measured EDS values, which were obtained from much larger areas. Furthermore, the EDS analysis has a systematic error of 5 ~ 10%. Another possible reason for the difference is that the real m values for the Cu-Al system might be different from those deduced from the curves in Fig. 6.9.

6.2.2 From FCC to HCP

As shown in section 6.2.1 and chapter 2, the HCP structure and the chemical composition of the interlayer are consistent with the Hume-Rothery rules. This is most likely the driving force for the interlayer formation. In this section, it will be discussed how the HCP phase can form from the FCC matrix.

Though HCP is more favorable than FCC when the valence electron density is around 1.64~1.89^[Li_{ZC}], the transformation of FCC to HCP needs the Shockley partial dislocation mechanism combined with interdiffusion as reported by Dahmen^[Dahmen] and Howe *et al.*^[Howe]. In a FCC structure, one perfect dislocation with $a/2 \langle 101 \rangle$ Burgers vector has a higher line energy compared to the sum of two Shockley partial dislocations with $a/6 \langle 211 \rangle$ Burgers vectors (see Eq. 2.4 to 2.6 in Chapter 2.3.1). The movement of a Shockley partial dislocation leads to a shear of a (111) plane, which induces a change of the stacking sequence from ABCABC to ABCABA. When the formed Shockley partial dislocation has passed through the whole closed packed (111)_{FCC} plane (all atoms in the same (111)_{FCC} plane have shifted along an $a/6 \langle 211 \rangle$ vector), a layer with HCP structure is formed. Similarly, arrays of (111) planes of the FCC structure can glide along $\langle 211 \rangle$ directions by a vector of $a/6 \langle 211 \rangle$ and thus increasing the thickness of the HCP layer. The schematic of the FCC/HCP transformation in $\langle 110 \rangle$ projection is shown in Fig. 6.10.

The $a/6 \langle 211 \rangle$ Shockley partial dislocation leads to a shear of $a/6 \langle 211 \rangle$, which is less than the smallest atomic distance in the FCC lattice, $1/2 \langle 110 \rangle$. In the [110] viewing direction, the [1-12] lattice vector extends over (111) planes, i.e. the $a/6 [1-12]$ lattice vector extends over $2/3$ projected atomic distances in the (111) plane.

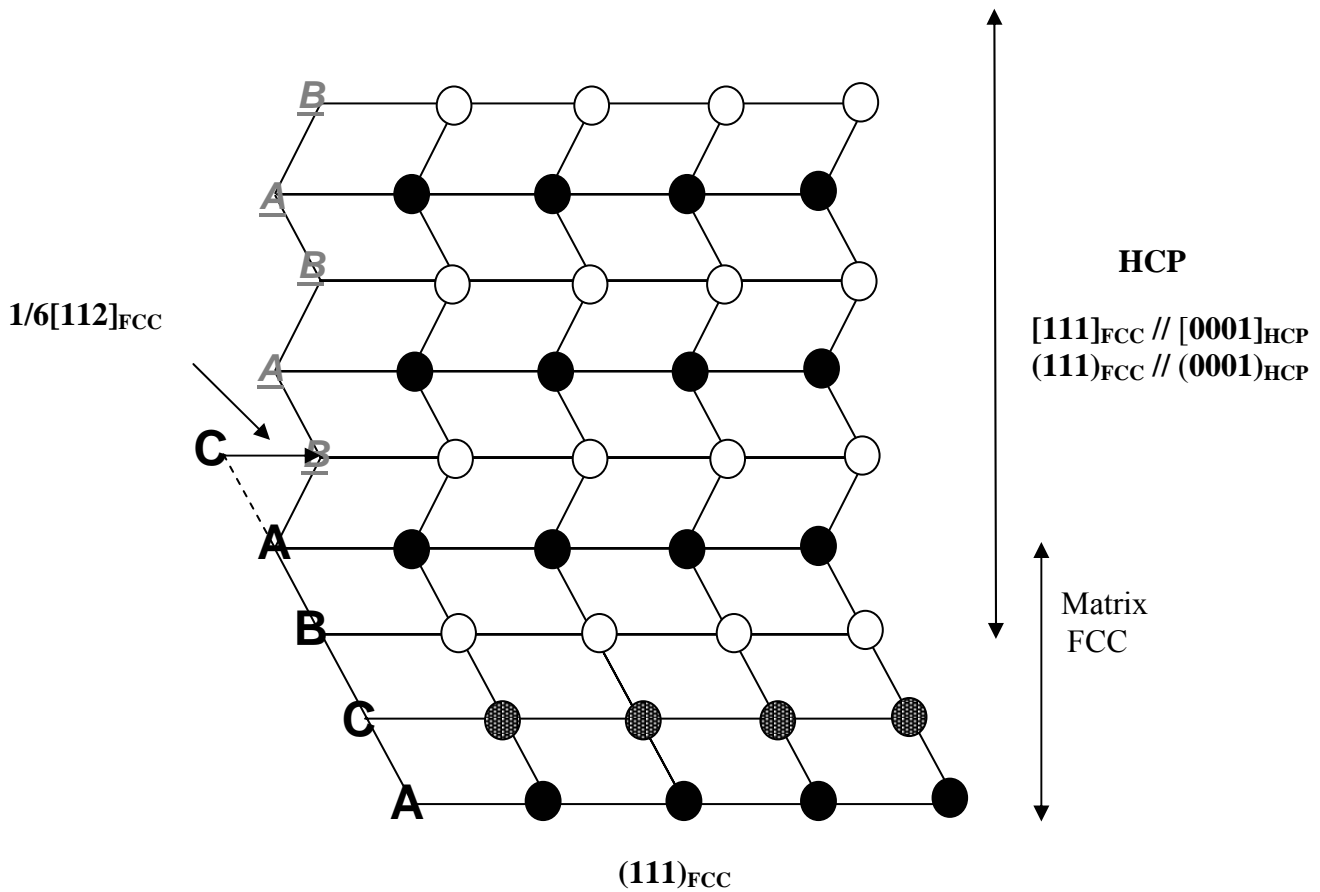


Fig. 6.10 FCC to HCP transformation model induced by Shockley partial dislocation with $a/6 \langle 112 \rangle$ Burgers vector ^[after Dahmen]. The circles filled with different pattern/brightness indicate different atom positions. The end of the arrow is the position for the FCC model and the head is the position for the HCP model. The arrow is an $a/6 \langle 112 \rangle$ Burgers vector. The four layers marked with under-line letters have slipped.

In the present study, the change in stacking sequence has been revealed by HRTEM images (e.g. Fig. 5.18). Both Cu and Al layers have FCC structure, with ABCABC sequence along the $[111]$ direction, while the stacking sequence has changed to ABAB in the interlayer. It is obvious that a FCC / HCP transformation has occurred. Fig. 6.11 shows the Cu/HCP interface, which is indicated by

a dark line. The HCP structure is above the line and the FCC structure is below this line. A closer look at the (111) atom plane, marked by the black line, shows that the positions of the atoms gradually change from C (Fig. 6.12). Thus there is an additional shear in this plane. In the left part of Fig. 6.11, atoms take the C_1 position which is repeating the position of C_0 three atom layers above, thus continuing the FCC structure. In contrast, at the right part of Fig. 6.11, the C_0 position is not repeated after three planes. The position of the atom (the head of the arrow) has shifted by $2/3$ projected atomic distances along the $[112]$ direction. The shift comes from different lattice parameters of Cu and the HCP interlayer. This shift could be due to a Shockley partial dislocation with an $a/6 \langle 1-12 \rangle$ vector, which induces an FCC_{Cu}/HCP transformation.

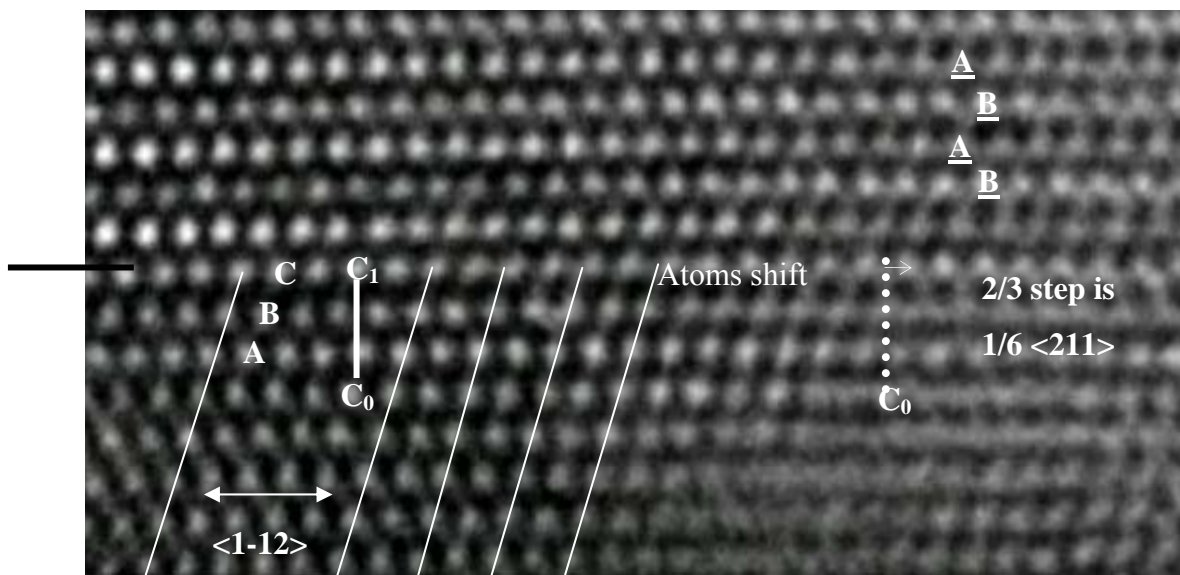
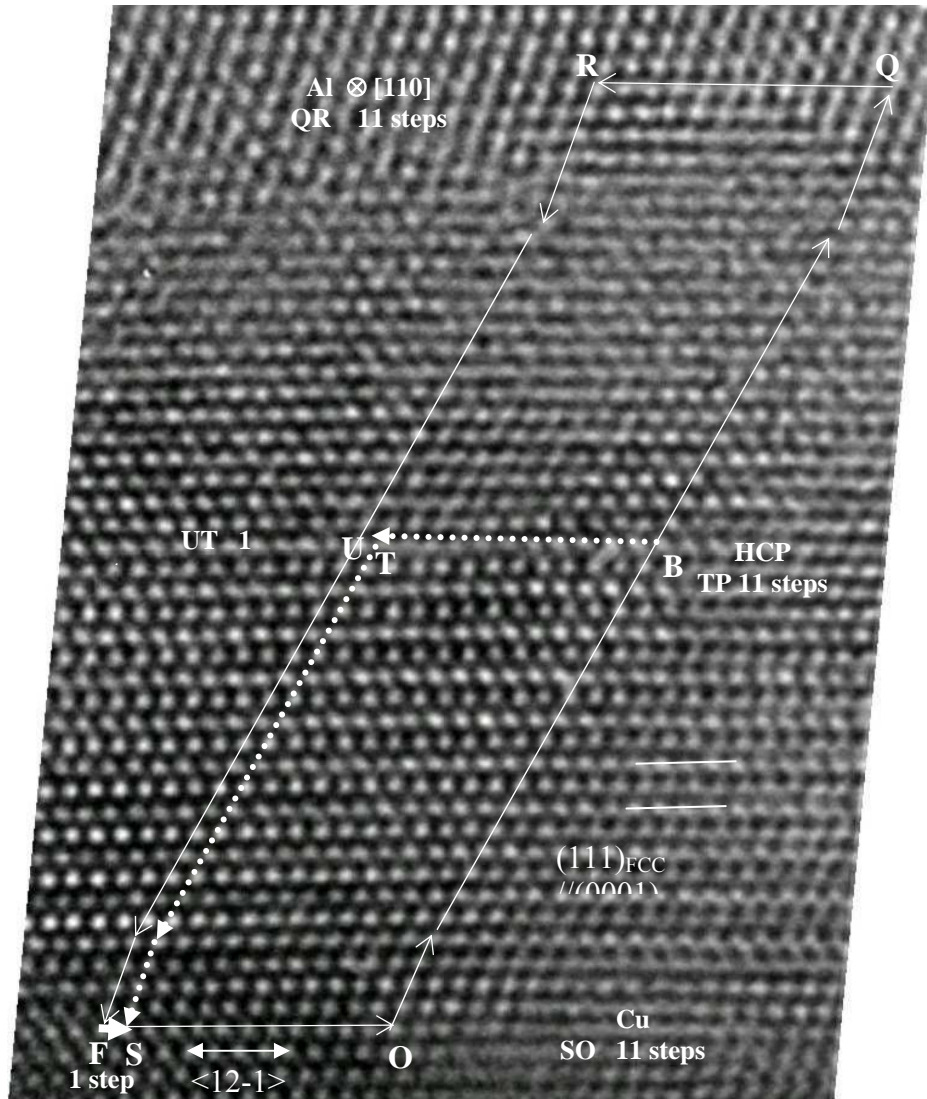


Fig. 6.11 HRTEM image of a HCP/FCC interface which is marked by the dark line. Above this line the HCP structure is formed. From the left side to the right side, the FCC structure is deformed and the C layer of FCC is gradually transforming into the A layer of HCP. The end of the arrow represents the atom position for the FCC structure, and the head of the arrow is the atom position for HCP structure. The distance between them is $2/3$ atomic distance in $[1-12]$ direction in the (111) plane. The stacking ordering is noted in the figure.

The FCC_{Al}/HCP interface is formed in the same way as discussed above for the FCC_{Cu}/HCP interface. Since Al and Cu have a 10 % lattice mismatch, the deformed HCP layer can hardly form coherent interfaces to both Cu and Al. Dislocation in the FCC/HCP/FCC structure can be investigated by dislocation circuits, as drawn in Fig. 6.12 (a). The dislocation circuit, SOBQRUFS, which keeps 11 steps along the $[1-12]$ direction and starts from Cu to Al crossing the HCP layer, shows a dislocation with an $a/4 [1-12]$ Burgers vector corresponding to the distance between the end and start point (marked by FS in Fig. 6.12 (a)). If the dislocation circuit is drawn only in Cu and HCP regions, the finishing point is identical to the starting point (SOBTS). However, if another dislocation circuit (TBQRUT) is constructed which includes the HCP and Al, a dislocation with $a/4 [1-12]$ projected Burgers vector (distance UT) is still observed.



(a)

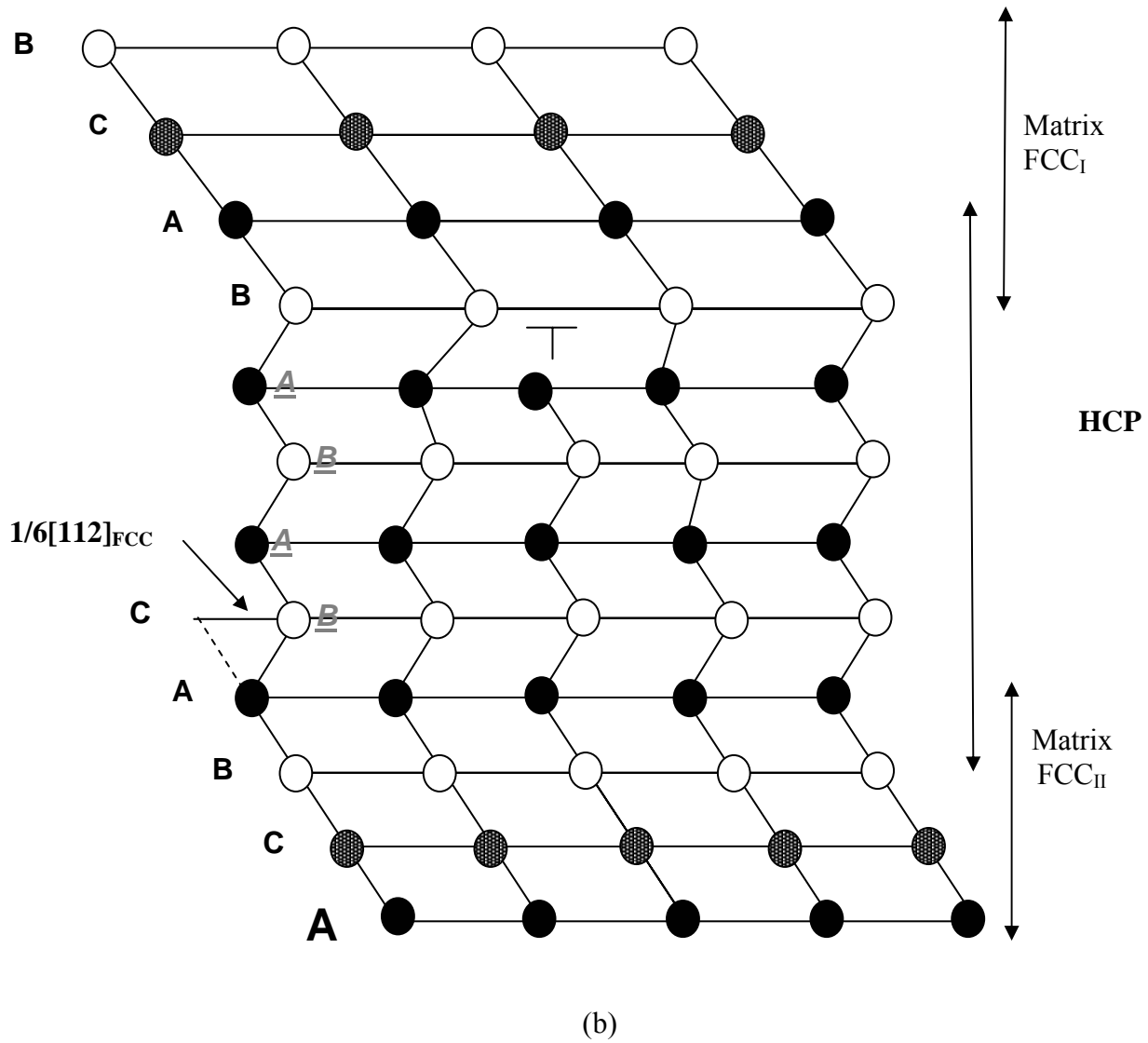


Fig. 6.12 (a) A dislocation circuit (SOBQRUFS), showing the formation of a dislocation with $1/3 [112]$ Burgers vector (distance FS) across Cu, HCP phase and Al. S is the start of the circuit and F indicates the finishing point of the circuit. The circuit with a dashed line (SOBTS) is only including Cu and the HCP structure. The step lengths have been marked in the image. (b) is a model for a FCC_I /HCP/ FCC_{II} structure, in which an edge dislocation exists as well as Shockley partial dislocation.

The formed Cu/HCP interface has similar lattice parameter as Cu. As mentioned above since Cu and Al have a 10 % lattice mismatch, if the two lattices are connected by one HCP phase, phase deformation and dislocations will form to reduce the strain. This is the reason that the dislocation has formed within the interlayer. The corresponding model (the thickness of the layer is much smaller than the real one) is displayed in Fig. 6.12 (b). It should be noted that in principle the $a/4$ [1-12] dislocation could also form at the Cu / HCP interface. However, in the present experiments the coherent interface structure occurred between Cu and the HCP phase.

In summary, when a FCC/HCP transformation occurs in a single matrix film, the mechanism can be described by the formation of Shockley partial dislocations (Fig. 6.10). When the transformation occurs in bilayer films with large lattice mismatch between the different matrixes, besides Shockley partial dislocations which introduce the FCC_I/HCP and HCP/FCC_{II} transformations, also edge dislocations form decreasing the strain from the lattice misfit (Fig. 6.12 (b)). The investigated sample belongs to the second type and both kinds of dislocation have been observed by HRTEM.

6.2.3 The mechanism of phase formation

Combining the findings from paragraph 6.2.1 and 6.2.2, the mechanism of the HCP phase formation can be describe as follows: interdiffusion occurs from pure Al to pure Cu, and gradually changes the chemical composition of the Cu-Al rough interface during the deposition of the Cu film. At the same time, the valence electron density of the atoms at the interface varies depending on the chemical changes (Eq. 2.5). Then the Fermi sphere of the alloyed atoms which is modified by the valence electron density, will contact the Brillion zone. Therefore, when the Fermi sphere expands to a certain level, the FCC structure at the interface could be transformed to the HCP structure which is energetically favorable, and stacking faults trigger the structure transformation to occur.

However, if the valence electron density does not reach the critical value, the structure will not transform, although the composition is still changed by interdiffusion. This happened in the area near the HCP interlayer, where the structure is FCC (or deformed FCC) but the composition is different from the pure metal. Both the experimental EDS results (Fig.5.27) and the deformed FCC

structure near the HCP interlayer (Fig. 6.11) display these characteristics of the interlayer. When the interdiffusion across the FCC / interlayer continues, the formation of the HCP structure will continue as well as the Shockley partial dislocation slip through the plane parallel to the interface.

After the short and general description of the HCP phase formation mechanism, it will be discussed why the FCC-HCP transformation occurs only during the film deposition and how the interfaces with the two different FCC matrix films look like.

As mentioned in Chapter 6.1.1, XRR measurements have indicated that the interlayer has formed during film deposition, and TEM results also revealed that both the sample preparation and electron radiation in TEM investigations do not affect on the growth of the interlayer. All of these facts indicate that the interlayer forms during deposition. During film growth, the ad-atoms have a higher mobility than later in the solid phase even if the substrates were at RT. In addition, the Al surface is rough, and the driving force for diffusion across the curved interface is high. Therefore, during deposition diffusion can be strong enough to induce a phase transformation at RT. The diffusion rate of Cu in Al at RT is $\sim 10^{-21} \text{ m}^2/\text{s}^*$, and thus is too small to account for the formation of the interlayer after deposition. This is also the reason why the intermetallic phase stops to grow after deposition at a thickness of 8 nm. During the one year when this work carried on, the thickness of the interlayer in the same film sample did not change, providing some evidence for this conclusion.

As mentioned above, the interdiffusion between Cu and Al is fast at a highly curved Al surface. Depending on the area, the Al surface is concave or convex. At the convex Al surface, the diffusion rate of the Cu atoms will be higher compared to the concave area and the opposite is true for the Al atoms. The roughness will be decreased and on the same time a diffusion zone containing Cu and Al atoms will form. At the beginning of the Cu deposition, Cu ad-atoms reach the Al layer. On the same time, Al will diffuse into the growing Cu layer. When a certain chemical composition range is reached in this diffusion zone, FCC-HCP transformation can start according to Hume-Rothery laws and by introducing Shockley partial dislocations, as well as the formation of the

* Because the diffusion rate of Cu in Al at RT is not available, the value was roughly estimated by following the tendency of the diffusion rates between 440 to 570 °C using Fick's second law of diffusion. However, the estimated diffusion rate at RT might be larger than the real one.

Al(Cu)-HCP interface. Since the simple mixed Cu-Al layer adjacent to the HCP is more disordered, the Al-HCP interface is not sharp.

During the deposition of Cu atoms, the HCP layer is growing while the concentration of Al is less and less. When the concentration of Al is out side of the special value range, the HCP formation will stop. Then the further deposited Cu-atoms and diffused Al will form an interface with the HCP phase. Since the observed HCP phase is Cu-rich (55 ~ 68 at %) and the terminating HCP cell should have the highest Cu concentration (~ 70 %), the lattice parameter will be not very different from pure Cu. And thus the Cu-HCP interface can be coherent. During the following growth of the Cu layer, residual strain can be released by dislocations into the pure Cu. This is also the reason why the Cu layers contain more dislocations.

6.2.4 Comparison to literature results on structure transformations in metal films

Many results using STM [Ling], [Meunier], [Radeke], [Jacobsen], [Lundgren], [Günther] have illustrated that reconstruction is a common phenomenon at metal-metal interfaces. Though the reconstructed interface is usually a few layers thick, it also gives a hint that this reconstruction could be the beginning stage of a structure transformation. However, the interlayer between Cu-Al in the present work is changed not only in structure but also in the chemical concentration compared to the bulk films. Lundgren *et al.* [Lundgren] found that an alloy CoPt can form at the Co/Pt interface where stacking faults also occurs when Co is only 2ML thick. This might be very similar to what happens on the rough Cu/Al interface, and may also explain the structure change at the Cu-interlayer or Al-interlayer interface. However, to explain the formation of the observed interlayer in present work, which possesses a broad chemical concentration, Hume-Rothery laws have to be employed in addition.

Amorphous layer can exist at metal-metal interfaces, and form a SS (solid solution)-amorphous structure [Clemens], [Egami], [Kwak], [Benedictus]. At certain composition and temperature ranges, ordered phases have lower Gibbs free energies, and the amorphous layer will transform to equilibrium alloy phase (s) at the interface [Schwarz]. It is possible that the HCP layer in this work is developed from an amorphous layer after deposition, since the XRR experiment, which was

performed directly after film deposition, can only detect the material and thickness but not the structure. However, there is no evidence that a continuous amorphous layer forms first and then transforms to the HCP phase.

Similar to the results in the present work, some ordered phases have been found at interfaces in metal film systems by Liu *et al.* [Li JH], [Li 2005], [Li ZC], [Yan], [Chen], [YG] and [Zhang ZJ] and Pan *et al.* [Zeng 2001] [Zeng 2002], [Pan]. They choose various binary metal systems, such as Ni-Ru (FCC-HCP), Nb-Cu (BCC-FCC), Mo-Co (BCC-HCP), most of them are immiscible in equilibrium. The multilayer films were treated by 200 keV ion-beam mixing or by 10 keV IBAD technique. It was found that some metastable phases formed at the interfaces, which have different lattice parameters with the base material. Calculations revealed that the Gibbs-free energy of the new phases at the interfaces was changing with chemical composition and structure.

The Cu-Al system was not studied in the framework of IB and IBAD, and there are many thermo-stable intermetallic phases in the Cu-Al system. Another important difference is that the symmetry of the metastable phase is the same as one of the base metal films in the studies performed by Liu *et al.* [Li JH], [Li 2005], [Li ZC], [Yan], [Chen], [YG] and [Zhang ZJ] and Pan *et al.* [Zeng, 2001 and 2002, Pan], while the present experiments revealed a metastable phase with different symmetry to the base films. According to the studies of Liu *et al.* [Li JH], [Li 2005], [Li ZC], [Yan], [Chen], [YG] and [Zhang ZJ] and Pan *et al.* [Zeng 2001] [Zeng 2002], [Pan], the excess interfacial free energy and the irradiation energy were the driving force for the formation of metastable phases. In the present work, one of the possible driving force might be the ion-milling during TEM specimen preparation (4.5 keV and unfocused). This value is similar to the ~10 keV ion beam used in their experiments. But the 10 keV ion beam is employed during the film deposition process; while the 4.5 keV beam for ion-milling is used after deposition and applied in a cooling stage. The effects in these two processes are different. As discussed in the last section, the additional energy of the ad-atoms during deposition is more reasonable to be the driving force for the phase formation. They enhance the diffusion rate during deposition and induce the phase transformation by changing composition.

Chapter 7

Conclusions

In this chapter, the main experimental results and the corresponding analysis for the interfaces in the layered Cu/Al films will be summarized.

Depending on the film deposition conditions, layered Cu/Al films process different characteristics. Multilayered (2, 4 and 8 layers) Cu/Al films deposited on Si (0001) by sputtering are polycrystalline. Bilayer Cu/Al films, which grew on sapphire (0001) substrates by sputtering, are $(111)_{\text{FCC}}$ textured with the orientation relationship of $\pm \langle 110 \rangle (111)_{\text{Cu}} // \pm \langle 110 \rangle (111)_{\text{Al}} // \langle 2-1-10 \rangle (0001)_{\text{sapphire}}$, and reveal an interlayer at the interface consisting of thermodynamic stable intermetallic phases. The Cu/Al bilayer film deposited on sapphire (0001) by MBE at RT is epitaxial. These films were investigated in detail in the present work, and the characteristics of the occurring Cu/Al interface will be summarized in 4 parts in the following:

1. Structure

The orientation relationship between the bilayer films and the substrate is:

$$\langle 110 \rangle (111)_{\text{Cu}} // \langle 110 \rangle (111)_{\text{Al}} // \langle 10-10 \rangle (0001)_{\text{sapphire}}.$$

An interlayer with the thickness of 8 nm forms between the pure Cu and the pure Al films. HRTEM revealed that along $[111]_{\text{FCC}}$ direction, the atomic structure of the interlayer has an *ABAB* stacking sequence, which is identical to that of a HCP structure in $[0001]$ direction. A HCP atomic model,

with the lattice parameters $a = b = 0.256$ nm, $c = 0.419$ nm, $\gamma = 120^\circ$, and the space group $P\bar{6}m2$, was constructed and used for image simulations. Quantitative HRTEM revealed agreements between simulated images and experimental images of 93.1 % and 93.4 %, in $\langle 110 \rangle_{\text{FCC}}$ and $\langle 112 \rangle_{\text{FCC}}$ directions, respectively. The orientation relationship between the FCC metal layers (Cu and Al) and the HCP interlayer is:

$$\langle 110 \rangle (111)_{\text{FCC}} // \langle 11\bar{2}0 \rangle (0001)_{\text{HCP}}.$$

Furthermore, lattice distortion analysis (LADIA) illustrated that the HCP lattice is expanding from the near-Cu-side to the near-Al-side.

2. Chemical composition

EDS linescans experiments, which were performed from the pure Al to the pure Cu layer across the interlayer, indicated that the chemical concentration is gradually changing from the near-Al-side to the near-Cu-side. After quantitative EDS analysis using a k -factor from a prepared standard CuAl_2 alloy, it is found that the chemical composition of the interlayer is 27 ~ 58 at% Al, and that the Al concentration is gradually increasing from the near-Cu-side to the near-Al-side. Using Hume-Rothery laws for electron phases and beam broadening effects due to experimental conditions, the wide chemical concentration range for the HCP phase can be explained.

3. Formation mechanism

Employing Hume-Rothery laws and Shockley partial dislocation, the formation of the intermetallic phase with HCP structure and broad composition range can be explained. According to Hume-Rothery laws the HCP structure can be energetically favored compared to the FCC, when the chemical composition reaches a certain region during deposition. At the same time, stacking defects will induce the FCC-HCP structure transformation by extending the Shockley partial dislocation in $\langle 112 \rangle$ direction. Since the HCP phase can be stable within a wide chemical region, the concentration of it can be broad.

4. Thermodynamic stability

In-situ heating experiments were performed in TEM at $\sim 600^{\circ}\text{C}$. After the specimen was cooled down to RT, HRTEM revealed that the HCP phase has disappeared and other equilibrium intermetallic phases form. This suggested that the HCP intermetallic phase is metastable. XRD measurements, which were carried out after *ex-situ* heating of the films, showed that the HCP metastable phase is unstable for the temperatures above 120°C .

List of Figures

Chapter 2

Fig.2.1	Mismatch and strain types in film systems	5
Fig.2.2	Schematic drawing of a cluster on a substrate and the forces acting on the cluster.....	8
Fig.2.3	Three kinds of interface structures.....	9
Fig.2.4	Stacking order of atomic layers in $\langle 111 \rangle$ direction in FCC lattices.....	11
Fig.2.5	Burgers vectors of perfect dislocations and Shockley partial dislocations	12
Fig.2.6	Cu-Al binary phase diagram.....	18
Fig.2.7	GPI in the viewing direction of $[001]_{\text{Al}}$	20
Fig.2.8	Schematic drawings of the structures of Θ'' (GP II), Θ' and Θ (CuAl_2).....	21

Chapter 3

Fig.3.1	The calculated free-energy diagram of the Ni–W system.....	28
---------	--	----

Chapter 4

Fig.4.1	Schematic drawing for θ - 2θ scan experiments and pole figure measurements.....	35
Fig.4.2	Sketch of the reflection and refraction in a layered structure.....	36
Fig.4.3	Force distance curve and the sketch of an AFM.....	38
Fig.4.4	Ray diagram of imaging and diffraction modes in TEM after Reimer ^[Reimer]	40
Fig.4.5	Schematic drawing for the image formation in HRTEM ^[after Kienzle]	42
Fig.4.6	Schematic illustration of the electron wave propagation ^[after Tchernychova] and the diagram for quantitative HRTEM.....	47

Fig.4.7	Schematic drawing of the analytical TEM VG HB501 UX.....	49
Fig.4.8	The signals detected by EDS and EELS.....	50
Fig.4.9	An EELS spectrum and the corresponding energy levels.....	51
Fig.4.10	Cross- sectional TEM specimen preparation with different embedding ways.....	55
Fig.4.11	Light microscopy images of the cast CuAl ₂ material.....	58
Fig.4.12	XRD profile from the cast sample of CuAl ₂	59

Chapter 5

Fig. 5.1	XRD θ - 2θ scan of 2, 4 and 8 layered Cu/Al films on Si (001).....	62
Fig. 5.2	XRD Pole figures for (111) _{FCC} plane of the Cu/Al bilayer film on Si (001).....	64
Fig. 5.3	FIB images of Cu/Al multilayer films on Si (001).....	65
Fig. 5.4	BF TEM images for 2, 4, and 8 layered Cu/Al films on Si (001).....	66
Fig. 5.5	XRD of a bilayer Cu/Al film grown on sapphire (0001) by magnetron sputtering.....	69
Fig. 5.6	XRD pole figures for (111) _{FCC} plane of the Cu/Al bilayer film on sapphire (0001).....	70
Fig. 5.7	FIB image of bilayer Cu/Al bilayer film prepared by sputtering on sapphire (0001).....	71
Fig. 5.8	BF images and SAD of the Cu/Al films deposited on sapphire (0001) by sputtering.....	73
Fig. 5.9	HRTEM image of the interlayer between Cu and Al (region 1) in sputtered bilayer films on sapphire (0001)	74
Fig. 5.10	HRTEM image of the interlayer between Cu and Al (region 2) in sputtered bilayer films on sapphire (0001).....	76
Fig. 5.11	BF STEM image of the interlayer between Cu and Al in sputtered bilayer films on sapphire (0001).....	76
Fig. 5.12	BF, HAADF and DF STEM images of the interlayer at the Cu/Al interface in sputtered bilayer films on sapphire (0001).....	77
Fig. 5.13	EELS spectra from various regions in the Cu-Al bilayer film on sapphire (0001) by sputtering.....	78
Fig. 5.14	HRTEM images from the Al/Al ₂ O ₃ interface in sputtered bilayer film samples.....	80
Fig. 5.15	XRD profile of the bilayer Cu/Al film deposited by MBE.....	81
Fig. 5.16	XRR experimental curve and corresponding fitted curve of the bilayer Cu/Al	

	film deposited by MBE.....	82
Fig. 5.17	AFM images of a 100nm thick Al film grown on sapphire (0001) by MBE.....	84
Fig. 5.18	BF image and SAD from the bilayer films deposited on sapphire (0001)by MB.....	86
Fig. 5.19	HRTEM image of the interlayer in Cu/Al bilayer films deposited on sapphire (0001) by MBE.....	87
Fig. 5.20	A dislocation between the interlayer and the Cu film in bilayer films deposited on sapphire (0001) by MBE.....	88
Fig. 5.21	HRTEM image of the interlayer and Al film	89
Fig. 5.22	Simulated HRTEM image map	90
Fig. 5.23	Atomic model of the HCP structure and corresponding quantitative simulations.....	91
Fig. 5.24	HRTEM image for the distorted interlayer	93
Fig. 5.25	Lattice deformation map of the interlayer	94
Fig. 5.26	STEM BF image of the Cu/Al bilayer system with an interlayer occurring at the Cu/Al interface.....	96
Fig. 5.27	EDS linescan profile from Al to Cu across the interlayer.....	97
Fig. 5.28	EELS curves at the Al L _{2,3} edge and the Cu M _{2,3} edge and DF image at the corresponding area.....	98
Fig. 5.29	BF TEM image of the bilayer film after annealing at 600°C for 1 second.....	99
Fig. 5.30	HRTEM image of the Al layer and two CuAl ₂ grains.....	100
Fig. 5.31	HRTEM image of the Cu layer after annealing.....	100
Fig. 5.32	Two CuAl ₂ grains with different orientations.....	101
Fig. 5.33	Microdiffraction patterns of Cu ₉ Al ₄	102
Fig. 5.34	SAD and microdiffraction pattern of CuAl.....	103
Fig. 5.35	Bright field images of the CuAl and Cu ₉ Al ₄ grains.....	104
Fig. 5.36	XRD of Cu-Al bilayer films annealed at 120°C and 160°C	105
Fig. 5.37	XRD of Cu-Al bilayer films annealed at 200°C and 240°C	106

Chapter 6

Fig. 6.1	Simulated HRTEM image calculated by using an orthorhombic atomic model.....	110
Fig. 6.2	Schematic drawing of beam broadening in thin film specimen.....	112

Fig. 6.3	Relationship between thickness and beam broadening in Cu and Al layers.....	113
Fig. 6.4	Gaussian functions with various σ values.....	114
Fig. 6.5	Calculated concentration profiles using different beam sizes and the corresponding linear decreasing concentration model.....	116
Fig. 6.6	Calculated concentration profiles using different beam sizes and the corresponding concentration model with a slope-function	117
Fig. 6.7	Calculated concentration profiles using different beam sizes and the corresponding concentration model with a step-function	118
Fig. 6.8	The influence from the chemical composition on the XCF.....	121
Fig. 6.9	The relationship between the electron concentration and axial ratio in various binary alloy systems with HCP structure.....	125
Fig. 6.10	FCC to HCP transformation model.....	128
Fig. 6.11	HRTEM image of a HCP/FCC interface.....	129
Fig. 6.12	HRTEM image of dislocations in Cu/Al bilayer films and a model for a $FCC_I/HCP/FCC_{II}$ structure.....	130

List of Tables

Chapter 2

Table.2.1.	Crystal structure and lattice parameters of phases in the Cu-Al system.....	19
------------	---	----

Chapter 5

Table 5.1	OR of Cu/ Al/sapphire bilayer (400nm/400nm) films prepared by sputtering.....	71
Table 5.2	Possible phases for the structures at the interlayer.....	74
Table 5.3	Chemical composition and possible phases at the interlayer between Cu and Al films grown on sapphire at 200°C.....	79
Table 5.4	The values of thickness and roughness of layers in Cu/Al bilayer film.....	83

Bibliography

- [Askeland] D. R. Askeland, *The Science and Engineering of Materials*, Wadsworth Publishing Company, Third edition, (1994)
- [Auciello] O. Auciello and C. M. Foster, *Annu. Rev. Mater. Sci.* **28**, 501 (1998)
- [Blanpain] B. Blanpain, L. H. Allen, J.-M. Legresy, and J. W. Mayer, *Phys. Rev. B.* **39**, 13067 (1989)
- [Benedictus] R. Benedictus, A. Böttger, and E. J. Mittemeijer, *Phys. Rev. B.* **54**, 9109 (1996)
- [Barrett] C. R. Barrett, W. D. Nix, and A. S. Tetelman, *Principles of Engineering Materials*, Prentice Hall, (1973)
- [Bauer] E. Bauer, *Zeitschrift für Kristallographie* **110**, 372, (1958)
- [Broeder] F. J. A. Den Broeder, M. Klerk, J. M. Vandenberg, and R. A. Hamm, *Acta metall.* **31**, 285 (1983)
- [Campbell] R. A. Campbell, J. A. Rodriguez, and D. W. Goodman, *Phys. Rev. B* **46**, 7077(1992)

- [Campisano] S. U. Campisano, E. Costanzo, and F. Scaccianoce, *Thin Solid Films* **52**, 97 (1978)
- [Cahn] R. W. Cahn and P. Haasen, *Physical Metallurgy*, Elsevier, Third edition, (1983)
- [Carlberg] M. H. Calberg, E. P. Münger, and V. Chirita, *Phys. Rev. B.* **54**, 2217 (1996)
- [Case] F. C. Case, *J. Vacuum Sci. Technol.* **5**, 1762 (1987)
- [Chen HY] HY. Chen and S. M. Heald, *J. Appl. Phys.* **66**, 1793 (1989);
HY. Chen and S. M. Heald, *Phys. Rev. B.* **42**, 4913 (1990);
S. M. Heald, HY. Chen, and J. M. Tranquada, *Phys. Rev. B.* **38**, 1016 (1988)
- [Chen YG] Y. G. Chen and B. X. Liu, *Acta mater.* **47**, 1389 (1999)
- [Chen Z] Z. Chen and K. N. Tu, *J. Appl. Phys.* **54**, 6829 (1983)
- [Chin] Y.-L. Chin, B.-S. Chiou, and W.-F. Wu, *Jpn. J. Appl. Phys.* **39**, 6708, (2000)
- [Clemens] B. M. Clemens and G. L. Eesley, *Phys. Rev. Lett.* **61**, 2356 (1988)
- [Dehm] G. Dehm, F. Ernst, J. Mayer, G. Möbus, H. Müllejans, F. Philipp, C. Scheu, and M. Rühle, *Zeitschrift für Metallkunde* **87**, 898 (1996).
- [Dahmen] U. Dahmen, *Scripta Metallurgica.* **21**, 1029 (1987)
- [Doig] P. Doig, D. Lonsdale, P. E. J. Flewitt, *Phil. Mag. A*, **41**, 761 (1980)
- [Du] K. Du, Y. Rau, N. Y. Jin-Phillipp and F. Phillipp, *J. Mater. Sci. Technol.*, **18**, 135 (2002)

- [Egami] T. Egami and Y. Waseda, *J. Non-Cryst. Solids* **64**, 113 (1984)
- [Fadnis] A. N. Fadnis, M. L. Trudeau, A. Joly and D. V. Baxter, *Phys. Rev. B.* **48**, 12202 (1993)
- [Feng] D. Feng, *Physical Metallurgy*, (1987)
- [Fultz] B. Fultz, and J. M. Howe, *Transmission electron microscopy and Diffractometry in Materials*, Springer Verlag, Second edition (2002)
- [Funamizu] Y. Funamizu, and K. Watanabe, *Trans. Jpn. Inst. Met.***12**, 1382 (1971)
- [Geng] J. Geng and P. Oelhafen, *Sur. Sci.* **452**, 161 (2000)
- [Gong] H. R. Gong, L. T. Kong, W. S. Lai, and B. X. Liu, *Phys. Rev. B.* **66**, 104204 (2002)
- [Goodhew] P. J. Goodhew and F. J. Humphreys, *Electron microscopy and Analysis*, Taylor and Francis (2001)
- [Gösele] U. Gösele and K. N. Tu, *J. appl. Phys.* **53**, 3252 (1982)
- [Gershinskii] A. E. Gershinskii, B. I. Fomin, E. I. Cherepov and F. L. Edelman, *Thin Solid Films* **42**, 269 (1977)
- [Gubbiotti] G. Gubbiotti, G. Carlotti, A. Montecchiari, M. De Crescenzi, R. Zivieri, L. Giovannini, and F. Nizzoli *Phy. Rev. B.* **62**, 16109 (2000)

- [Günther] C. Günther, J. Vrijmoeth, R. Q. Hwang, and R. J. Behm, *Phys. Rev. Lett.* **74**, 754 (1995)
- [Hamm] R. A. Hamm and J. M. Vandenberg, *J. Appl. Phys.* **56**, 293 (1984)
- [Hentzell] H. T. G. Hentzell, R. D. Thompson and K. N. Tu, *J. Appl. Phys.* **54**, 6923 (1983)
- [Hirth] J. P. Hirth and R. C. Pond, *Acta Mater.* **12**, 4749 (1996)
- [Hirvonen] J. K. Hirvonen, *Mater. Sci. Rep.* **6**, 215 (1991);
J.K. Hirvonen, *Surf. Coat. Technol.* **65**, 84 (1994)
- [Howe] J. M. Howe and G. J. Mahon, *Ultramicroscopy* **30**, 132 (1989)
- [Hull] D. Hull and D. J. Bacon, *Introduction to Dislocations*, Pergamon Press, Fourth edition, (2001)
- [Hume] W. Hume-Rothery, *Elements of structural metallurgy* (The institute of metal, London, Monograph and Report Series. No. 26), (1961)
- [Jacobsen] J. Jacobsen, L. Pleth Nielsen, F. Besenbacher, I. Stensgaard, E. Lægsgaard, T. Rasmussen, K. W. Jacobsen, and J. K. Nørskov, *Phys. Rev. Lett.* **75**, 489 (1995)
- [Jiang] H. G. Jiang, J.Y. Dai, H. Y. Tong, B. Z. Ding, Q. H. Song and Z.Q. Hu, *J. Appl. Phys.* **74**, 6165 (1993)
- [Johnson] W. L. Johnson, *Prog. Mater. Sci.* **30**, 81 (1986)

- [Johansson] B. O. Johansson, J. E. Sundgren, U. Helmersson and M. K. Hobbs, *Appl. Phys. Lett.* **44**, 670 (1984)
- [Jones] H. Jones, *J. Phys. Radium* **23**, 637 (1962)
- [Kief] M. T. Kief and W. F. Egelhoff, *Phys. Rev. B* **47**, 10785 (1993)
- [Kienzle] O. Kienzle, Ph. D. Thesis, University Stuttgart, Stuttgart, Germany (1999)
- [Knapp] A. Knapp and D. M. Follstaedt, *Phys. Rev. Lett.* **55**, 1591 (1987)
- [Kwon] K. W. Kwon, H. J. Lee, and R. Sinclair, *Appl. Phys. Lett.* **75**, 935 (1999)
- [Kurata] H. Kurata, '*Electron Microscopy Seminar Text*', the University of Tokyo, Tokyo, Japan (2000)
- [Kwak] J. S. Kwak, E. J. Chi, J. D. Choi, S. W. Park, and H. K. Baik, *J. Appl. Phys.* **78**, 983 (1995)
- [Laissardiere] G. T. de Laissardiere, D. Nguyen-Manh and D. Mayou, in press, *Materials Science*, (2005)
- [Larsen] K. Kyllesbech Larsena, S. Skovmanga, N. Karpeb, J. Bøttigera and R. Bormannc, *Nucl. Instr. Meth. B* **80-81**, 390 (1993)
- [Li, 2004] J. H. Li, L. T. Kong and B. X. Liu, *J. Materials Research*, **19**, 3547 (2004)
- [Li, 2005] J. H. Li, H. B. Guo, L. T. Kong and B. X. Liu, *Phys. Rev. B* **71**, 14107 (2005)
- [Li, XY] X. Y. Li, Z. F. Li and B. X. Liu, *J. Alloys and Compounds*. **334**, 167 (2002)

- [Li, ZC] Z. C. Li, D. P. Yu and B. X. Liu, *Phys. Rev. B.* **65**, 245403 (2002)
- [Li, ZC 2000] Z. C. Li, J.B. Liu, Z. F. Li and B. X. Liu, *J. Phys.: Condens Matter* **12**, 9231 (2000)
- [Lilienfeld] D. A. Lilienfeld, M. Nastasi, H. H. Johnson, and J. W. Mayer, *Phys. Rev. Lett.* **55**, 1587 (1985)
- [Lin] C. Lin, G. W. Yang, and B. X. Liu, *Phys. Rev. B.* **61**, 15649 (2000)
- [Ling] W. L. Ling, J. de la Figuera, N. C. Bartelt, R. Q. Hwang, A. K. Schmid, G. E. Thayer, and J. C. Hamilton, *Phys. Rev. Lett.* **92**, 116102 (2004)
- [Liu] B. X. Liu, Z. J. Zhang, Q. Jin and F. Pan, *Mater. Res. Soc. Symp. Proc.* **369**, 71 (1996)
- [Lundgren] E. Lundgren, G. Leonardelli, M. Schmid, and P. Varga, *Surf. Sci.* **498**, 257 (2002)
- [Mahon] G.J. Mahon, J.M. Howe and S. Mahajan, *Phil. Mag. Letters* **59**, 273 (1989)
- [Markwitz] A. Markwitz, W. Mattz, M. Waldschmidt and G. Demortier, *Surf. Interface Anal.* **26**, 160 (1998); A. Markwitz, W. Mattz and M. Waldschmidt, *Surf. Interface Anal.* **33**, 1 (2002)
- [Marinov] M. Marinov, *Thin solid films* **46**, 267 (1977)
- [Meng] W. J. Meng, C. W. Nieh, E. Ma, B. Fultz, and W. L. Johnson, *Mater. Sci. Eng.* **97**, 87 (1988)

- [Merkle] K. L. Merkle, M. I. Buckett, and Y. Gao, *Acta metal. Mater.* **40**, S249 (1992)
- [Meunier] I. Meunier, G. Tréglia, J.-M. Gay, B. Aufray, and B. Legrand, *Phys. Rev. B.* **59**, 10910 (1999)
- [Möbus] G. Möbus and M. Rühle, *Ultramicroscopy* **56**, 54 (1994).
- [Muddle] B.C. Muddle, J.F. Nie and G.R. Hugo, *Metall. and Materials Trans. A* **25**, 1841 (1994)
- [Nakagawa] T. Nakagawa, S. Mitsushima, H. Okuyama, M. Nishijima, and T. Aruga, *Phy. Rev. B.* **66**, 085402 (2002)
- [Ohring] M. Ohring, *Material Science of Thin Films*, San Diego, Academic Press, (2002)
- [Palmberg] P. W. Palmberg and T. N. Rhodin, *J. Chem. Phys.* **49**, 134 (1968)
- [Pan, 1995] F. Pan, Y. G. Chen, and B. X. Liu, *Appl. Phys. Lett.* **67**, 780 (1995)
- [Pan, 1996] F. Pan, Z. F. Ling, K. Y. Gao and B. X. Liu, *Mater. Res. Soc. Symp. Proc.* **398**, 337 (1996)
- [Polak] R. B. Schwarz and W. L. Johnson, *Phys. Rev. Lett.* **51**, 415 (1983)
- [Pond] R.C. Pond, Y.W. Chai and S. Celotto, *Materials Science and Engineering A* **378**, 47 (2004)
- [Radeke] M. R. Radeke and E. A. Carter, *Phys. Rev. B.* **51**, 4388 (1995)
- [Pötschke] G. O. Pötschke and R. J. Behm, *Phys. Rev. B.* **44**, 1442 (1991)

- [Parratt] L. G. Parratt, *Phys. Rev.* **95**, 359 (1954)
- [Polak] M. Polak, C. S. Fadley, and L. Rubinovich, *Phys. Rev. B* **65**, 205404 (2002)
- [Rajan] K. Rajan and E. R. A. Walluch, *J. Crystal Growth* **49**, 297 (1980)
- [Ramana] C. V. Ramana, P. Masse, R. J. Smith, and Bum-Sik Choi, *Phys. Rev. Lett.* **90**, 066101 (2003)
- [Rayne] J. A. Rayne, M. P. Shearer, and C. L. Bauer, *Thin solid film*, **65**, 381 (1980)
- [Reimer] L. Reimer, *Transmission Electron Microscopy*, Springer Verlag, (1984)
- [Roy] R. A. Roy, D. S. Yee and J. J. Cuomo, *Mater. Res. Soc. Symp. Proc.* **128**, 23 (1989)
- [Sachtler] J. W. Sachtler, M. A. van Hove, J. P. Biberian, and G. A. Somorjai, *Surf. Sci. Lett.* **110**, 19 (1981)
- [Schreiber] F. Schreiber, *Prog. Surf. Sci.* **65**, 151 (2000)
- [Schwarz] R. B. Schwarz and W. L. Johnson, *Phys. Rev. Lett.* **51**, 415 (1983)
- [Shearer] M. P. Shearer, S. K. Sen and C. L. Bauer, *Phys. Stat. Sol. (a)* **69**, 139 (1982);
M. P. Shearer, C. L. Bauer and A. G. Jordan *Thin Solid Films*, **61**, 273 (1979)
- [Simic] V. Simic and Z. Marinkovic, *J. The Less-Common Metals*, **72**, 133 (1980)
- [Smidt] F.A. Smidt, *Int. Mater. Rev.* **35**, 61 (1990)

- [Sonnenberg] N. Sonnenberg, A.S. Longo, M.J. Cima, B.P. Chang, K.G.Ressler, P.C. McIntyre, Y.P. Liu, *J. Appl. Phys.* **74**, 1027 (1993)
- [Su] C. M. Su, H.G.Bohn, K.-H. Robrock and W. Schilling, *J. Appl. Phys.***70**, 2086 (1991)
- [Stadelmann] P. A. Stadelmann, *Ultramicroscopy*, **21**, 131 (1987)
- [Tchernychova] E. Tchernychova, Ph. D. Thesis, University Stuttgart, Stuttgart, Germany (2004)
- [Tersoff] J. Tersoff and L. M. Falicov, *Phy. Rev. B.* **25**, 2959 (1982)
- [Tolan] M. Tolan, *X-Ray Scattering from Soft-Matter Thin Films*, Springer Verlag, (1999).
- [Tsakalakos] T. Tsakalakos and A. F. Jankowski. *Rev. Mater. Sci.* **16**, 293 (1986)
- [Tsay] J. S. Tsay and C. S. Shern, *Surf. Sci.* **396**, 313 (1998)
- [Tu] K. N. Tu, *Annu. Rev. Mater. Sci.* **15**, 147 (1985)
- [Tu, 1982] K. N. Tu, G. Ottaviani, U. Gösele, and H. Föll. *J. Appl. Phys.* **54**, 758 (1982)
- [Tu, 1977] K. N. Tu, *J. Appl. Phys.* **48**, 3400 (1977)
- [Vandenberg] J. M. Vandenberg and R. A. Hamm, *Thin Solid Films*, **97**, 313 (1982)
- [Vredenburg] A. M. Vredenburg, J. F. M. Westendorp, F. W. Saris, N. M. van der Pers, and Th. H. de Keijser, *J. Mater. Res.* **1**, 774 (1986)

- [Vinci] Richard P. Vinci and Joost J. Vlassak, *Annu. Rev. Mater. Sci.* **26**, 431 (1996)
- [Yan] H. F. Yan, Z. C. Li, and B.X. Liu, *J. Phys. D* **36**, 615 (2003)
- [Yang] G.W. Yang, C. Lin, B.X. Liu, *Appl. Phys. A* **69**, 403 (1999)
- [Williams] D. B. Williams and C. B. Carter, *Transmission Electron Microscopy*, Springer Verlag (1996)
- [Zeng, 2001] F. Zeng, B. Zhao and F. Pan, *Nuclear Instruments and Methods in Physics Research B.* **183**, 311 (2001)
- [Zeng, 2002] F. Zeng, M. Ding, B. Zhao and F. Pan, *Materials Letters*, **53**, 40 (2002)
- [Zhang Q] Q. Zhang, W.S. Lai and B.X. Liu, *Phys. Rev. B.* **61**, 9245 (2000)
- [Zhang ZJ] Z. J. Zhang and B. X. Liu, *J. Appl. Phys.* **76**, 3351 (1994)
- [Zhang ZJ, 1995] Z. J. Zhang and B. X. Liu, *J. Phys.: Condens Matter* **7**, L293 (1995)
- [Zhao] B. Zhao, D.M. Li, F. Zeng and F. Pan, *Appl. Surface Science.*, **207**, 334 (2003)
- [Zhao, 2004] B. Zhao, K. w. Geng, F. Zeng, et al *AJ. Mat. Sci. & Tech.* **20**, 577 (2004)

Acknowledgements

I would like to thank

- Prof. Dr. Dr. h.c. M. Rühle who gave me the opportunity to perform this study in his group, and his constant support, encouragement and guidance.
- Prof. Dr. E. Arzt for taking over the *Mitbericht*
- Dr. C. Scheu for her continuous guidance and help, support and many fruitful discussions during the past three years, especially for her unbelievable patience and effort in correcting this thesis.
- Dr. T. Wagner for the help in layered film growth, scientific discussions and many supports.
- Dr. G. Richter for his help with the quantitative HRTEM image analysis, continuous encouragements and discussions.
- Prof. Dr. Dehm and T. K. Schmidt for their rewarding discussion and nice cooperation in bilayer film systems deposited by sputtering
- Dr. S. Strum for his help in the EDS experiments performed in the VG STEM and discussions.
- Dr. W. Sigle and Dr. A. Leineweber for many fruitful discussions.

- Dr. Y. Jin-Philipp for the help in LADIA and Dr. H. Lamparter for the XRD experiments
- Mr. A. Weible and Dr. B. Lee for their assistance in annealing experiments
- Dr. L. Zhang, Ms. A. Vlad and Dr. A. Stierle for the XRR experiments and corresponding discussion.
- F. Wetscher for his help with the convolution analysis.
- U. Salzberger, U. Bäder, M. Kelsch and A. Strecker for their continuous support in TEM specimen preparation technique.
- Mr. P. Kopold and Mr. R. Höschen for the introduction to microscopy and technical supports in CTEM and HRTEM.
- All the members in Prof. Rühle group from 2003 to 2005, for warm working atmosphere, private discussions, and supports with all kind of problems.
- My parents and sister in China, all my friends in Germany and China, especially YiLin, for their strong supports and understanding.

This work was performed at the Max-Planck-Institut für Metallforschung, Stuttgart in the department of Prof. Rühle from January 2003 to December 2005. Financial support of the German Science Foundation through the Graduirtenkolleg 'Innere Grenzflächen in kristallinen Materialien' (GRK 285/3) is gratefully acknowledged.

Curriculum Vitae

Name: Limei Cha
Date of Birth: 24, March 1977
Place of Birth: Yunnan, China
Nationality: China
Marital Status: single

2003 - 2005: Ph.D. Student in the group of Prof. Dr. Dr. h.c. Manfred Rühle
at the Max-Planck-Institut für Metallforschung Stuttgart

1999 - 2002: Department of Engineering of Material and Metallurgy,
Kunming University of Science and Technology, China

Master Degree in Material Science (2002)

The title of thesis :

'The preparation and properties of bilayer manganite films'

1995 - 1999: Department of Material Science and Engineering
Tianjin University, China

Bachelor Degree in Material Science (1999)

The title of thesis:

'The methods to lower the resistivity of PTC ceramic material'